NORTHWESTERN UNIVERSITY

The Role of the Vimentin Cytoskeleton in Lung Cancer, Platelet Mechanics, and Acute Lung Injury

A DISSERTATION

SUBMITTED TO THE GRADUATE SCHOOL
IN PARTIAL FULFILLMENT OF THE REQUIREMENTS

for the degree

DOCTOR OF PHILOSOPHY

Biomedical Engineering

By

Alexandra Berr

EVANSTON, ILLINOIS

September 2022

Abstract

Vimentin intermediate filaments (VIFs) provide mechanical integrity to cells and serve as markers of tissue origin and cell differentiation. Several non-mechanical roles for vimentin have recently been reported, including regulation of key pathways that control cell growth, cell signaling, and cell motility. Here, I present the role of vimentin in three different contexts. (1) Vimentin is highly expressed in metastatic cancers, and its expression correlates with poor patient prognoses. However, no causal *in vivo* studies linking vimentin and NSCLC progression existed until now. *LSL-Kras*^{G12D}, *Tp53*$^{fl/fl}$ mice (*KPV*$^{+/+}$) were crossed with vimentin-knockout mice (*KPV*$^{-/-}$); *KPV*$^{-/-}$ mice have attenuated tumor growth and improved survival compared to *KPV*$^{+/+}$ mice. *KPV*$^{+/+}$ mice were treated with withaferin A (WFA), an agent that disrupts VIF formation. This treatment suppresses tumor growth and reduces tumor burden in the lung. Using an allograft tumor model, luciferase-expressing *KPV*$^{+/+}$, *KPV*$^{-/-}$, and *KPV*^{Y117L} cells were implanted into the flanks of nude mice to track cancer metastasis to the lung. *KPV*^{Y117L} cells form oligomers called unit-length filaments but cannot assemble into mature VIFs. *KPV*$^{-/-}$ and *KPV*^{Y117L} cells fail to metastasize, suggesting that cell-autonomous metastasis requires mature VIFs. Integrative metabolomic and transcriptomic analyses reveal that *KPV*$^{-/-}$ cells upregulate genes associated with ferroptosis, an iron-dependent form of regulated cell death. *KPV*$^{-/-}$ cells display reduced levels of the lipid repair enzyme glutathione peroxidase 4 (GPX4), leading to the accumulation of toxic lipid peroxides and increased ferroptosis in *KPV*$^{-/-}$ cells. I show that vimentin protects the cell from ferroptosis-mediated cell death, which contributes to tumor growth and metastasis in NSCLC. (2) Blood clots form after injury when platelets bind fibrin fibers and form thrombi. The mechanical properties of the clot are critical for proper wound healing and restoration of laminar blood flow. I found that platelet-rich plasma isolated from *Vim*$^{-/-}$ mice formed less contractile and viscoelastic thrombi than *Vim*$^{+/+}$ platelet-rich plasma. *In vivo*, *Vim*$^{-/-}$ mice exhibit longer clotting times than *Vim*$^{+/+}$ mice. I show that vimentin is

required for efficient and mechanically robust blood clot formation through this work. (3) Acute lung injury is mediated by IL-1β signaling, which requires maturation via the NLRP3 inflammasome. Our group found that vimentin scaffolds the NLRP3 inflammasome and is required for IL-1β release. To target vimentin-mediated inflammasome signaling, we designed PEG-b-PPS micelles that contain Five1, a recently identified small molecule that causes VIF disassembly. Here, I provide proof-of-principle evidence that these nanoparticles decrease IL-1β release *in vitro*. Together, I show that vimentin is critical in NSCLC signaling by suppressing ferroptosis and promoting metastasis. Vimentin confers unique mechanical properties to blood clots which is required for efficient hemostasis. Finally, vimentin can be targeted in a cell-specific manner through nanoparticle delivery to disrupt pro-inflammatory signaling scaffolds and suppress inflammation. These studies ultimately advance understanding of intermediate filaments' mechanical and non-mechanical roles in cancer biology, hemostasis, and acute lung injury.

Acknowledgments

I am so grateful to have been surrounded by so many incredible people over the course of my PhD. My advisor, Karen Ridge, has been an incredible source of support— when a problem arose during my project, she knew exactly when to step in and help me and when to let me figure it out on my own. Karen cares deeply about the success of her mentees—both in their professional and personal lives. To that end, I will forever be grateful for the support Karen gave me so that I could spend time with my mom in the last few months of her life. Thank you, Karen, for the invaluable mentorship and support over the past 6 years.

I owe a debt of gratitude to the rest of the Ridge lab as well. Yuan Cheng has been a huge source of support—she trained me on countless techniques and helped me with a million experience. I will fondly remember our time in the IVIS room. Jen Davis has also contributed greatly to this work—she put countless hours into image analysis and editing, which was invaluable to this project. To Maggie Turner and Mark Ciesielski, my first friends in the lab, thank you for the good times in the mouse room and at happy hours after the days in the mouse room. I am grateful for mentorship also from Clarissa Koch and Jennifer Hu, postdocs who were always happy to answer any silly questions I had. I appreciate all the time I got to spend with my fellow grad students, Kishore, McKenzie, and Tatiana, and everyone else in the Ridge lab: Chi, Andrew, Ruihua, Bria, Walter, Megan, Francisco, Grant, Dale, as well as all my pals in the Pulmonary Division. I would never have started my PhD without my incredible mentors at UVa—Kim Kelly, who gave me the opportunity to start working in a lab in high school, and Jenny Munson, under whose mentorship I became a confident and independent scientist. I would also like to thank Jessica Yuan, Kathryn Kingsmore, Chase Cornelison, and Ali Harris for showing me what grad school looked like and helping me get on the path to a PhD.

I have been very lucky to receive mentorship from sources outside my lab as well. To my committee, Evan Scott, Shu Liu, and Sasha Misharin, thank you for the insightful feedback from both engineering and medical perspectives over the years. I am grateful, too, for collaboration within my department (working with Molly Frey from the Scott lab), my division (bombarding the Chandel lab with questions about metabolism), and other institutions (working with Paul Janmey and Oleg Kim from UPenn to consider the biophysical implications of vimentin). These relationships have made me a better scientist and I am forever grateful for the support.

I could not have gotten to this point without the support of my family. My dad-- who encouraged my interest in STEM by constantly doing times tables with me while we listened to The Beatles on the drive to school-- showed me that a career as a scientist was possible. My sisters, Zoe and Lydia, have been so supportive; I have cherished their visits to Chicago and I'm so proud of them for finishing school and turning into adults while I've been in grad school. My mom, who instilled in me a sense of humor and a desire to help people, was my greatest source of support. Although she passed away in my third year of grad school, I truly would not have been able to do this program without her. She was an incredible person and supported me unconditionally.

Lastly, I could not have finished this PhD without my amazing friends. To my best friend, Anna—thank you for talking to me everyday and supporting me through high highs and low lows. I can't wait until we're both doctors. Thanks also to Yuni, who's been an excellent commiserator throughout our six years in the BME program. I'd like to thank my friends from home, college, and everywhere in between, who have pushed me to be the best version of myself: Emily, Peyton, Hannah, Julia, Casey, Willa, Adam, Megan, Marissa, Leigh, and lots more. Finally, thank you to my comedy pals, who showed me that there's more than a 9-5: Andrew, Jonathan, Luke, Jeff, Jackie, Tad, Diya. I love all of you and I could not have done this without you!

List of Figures and Tables

Table of Contents

Chapter 1. Introduction

The eukaryotic cytoskeleton is composed of a complex network of filaments that can be broadly divided into three categories: microfilaments, microtubules, and intermediate filaments (IFs). Microfilaments (actin) are the thinnest cytoskeletal filaments. They interact with molecular motors like myosin to exert forces that allow cells to move. The largest cytoskeleton filaments are microtubules (α- and β-tubulin); these filaments coordinate organelle trafficking and participate in mitosis. The third type of filaments, IFs, are named because their 10 nm average diameter places them between microfilaments and microtubules in size. Unlike these other well-defined cytoskeletal proteins, IFs were not distinguished from other cytoskeletal filaments until 1968 when electron microscopy allowed for investigators to identify IFs as structures distinct from actin and microtubules (1, 2).

Despite their relatively late discovery, IFs are encoded by the greatest number of genes among the three cytoskeletal networks. These IF genes code for a wide set of proteins that are organized into six distinct class (3). Types I and II are acidic and basic keratins, respectively. Keratin exists in many different forms and is constitutively expressed in epithelial cells, hair, and nails. Type III IFs are expressed in a range of tissues. Desmin is found in sarcomeres; glial fibrillary acidic protein (GFAP) is expressed in glial cells; vimentin is found in mesenchymal cells, white blood cells, and endothelial cells. Type IV IFs include neurofilaments, which are found in neuronal axons. Type V IFs are distinct in that they are composed of lamins, which are found in the nucleus, not the cytoplasm. Finally, Type VI IFs contain nestin, a protein expressed during neural development. Together, IFs represent a diverse set of proteins that are expressed in an array of different tissues.

The type III IF vimentin is one of the most widely studied IFs due to its high expression across a variety of tissues and was therefore one of the first IFs to be isolated from cell-free preparations (4). These filaments can be disassembled *in vitro* and repolymerized in salt solution (5).

Vimentin isolated from a range of animal models has been cloned and its sequence is highly conserved (6, 7).

The structure of vimentin dictates its function. Vimentin, like all other IFs, is transcribed as a monomer with an α-helical rod domain and non-helical head and tail domains. Two monomers form a coiled-coil dimer; these dimers then form tetramers, eight of which assemble into unit-length filaments (ULFs). Tetramers are the smallest stable soluble form of vimentin, and they participate in ATP-dependent subunit exchange with ULFs (8). ULFs anneal longitudinally to form full-length filament. Full-length filament disassembly is mediated by phosphorylation, and its assembly state determines its function (9, 10). For example, vimentin phosphorylation at Ser-38 causes filament disassembly, which then affects the cell's polarity and directionality of lamellipodia (10). Additionally, vimentin architecture affords it unique mechanical properties compared to actin and microtubules. Compared to the other two main cytoskeletal proteins, vimentin filaments are extremely flexible and can withstand high forces without breaking. These mechanical properties confer cells protection from compressive forces by increasing cell elasticity (11). Therefore, the assembly state of vimentin affords it a unique role as both a signaling and structural protein.

The work presented in this thesis relies heavily on the creation of the global vimentin knockout mouse (*Vim*$^{-/-}$). When this mouse was created nearly 3 decades ago, it was reported to display a relatively mild phenotype (12). However, in the nearly three decades since its development, studies have revealed a phenotype distinct from the WT mouse.

Of note, *Vim*$^{-/-}$ mice are much smaller than WT littermates when fed a standard diet (13). Specifically, *Vim*$^{-/-}$ mice accumulate less body fat than WT mice. Vimentin forms a cage around lipid droplets via an interaction with perilipin (14, 15). Relatedly, *Vim*$^{-/-}$ mice develop smaller lipid droplets and adipocytes than WT mice (16). Vimentin is therefore implicated in lipolysis, the process by which energy stored in fat is released. Vimentin physically interacts with hormone-sensitive lipase

(HSL), an enzyme that facilitates transfer of cholesterol to mitochondria (16). As a result, *Vim*$^{-/-}$ mice have reduced cholesterol influx into the mitochondria (17). Vimentin also interacts directly with the β3-adrenergic receptor, which increases ERK activation and lipolysis. Vimentin knockdown abrogates ERK signaling and reduces lipolysis in a mouse model (18). Interestingly, the first vimentin mutation reported in patients is associated with lipodystrophy (19, 20). Other studies identified that *Vim*$^{-/-}$ mice accumulate less fat than WT mice; relatedly, *Vim*$^{-/-}$ mice display some resistance to athererosclerosis (13, 21). Together, these reports suggest a critical role for vimentin in fat regulation and lipid droplet homeostasis.

Vimentin has a profound impact on kidney function. WT mice subjected to a partial nephrectomy survive up to 72 hours, while *Vim*$^{-/-}$ mice all die within the same timeframe (22). WT mice are able undergo renal vasodilation which allow them to maintain renal function and survival, while *Vim*$^{-/-}$ mice fail to recover and ultimately die from kidney failure. Sodium-glucose transporters, found in the proximal tubules of nephrons, are required for glucose resorption in the blood stream. Vimentin is required for proper localization of sodium-glucose transporters to the brush border membrane, which is necessary for maintaining proper function of the transporters (23). Therefore, vimentin is required for restoration of proper glucose transport following kidney injury.

Vimentin is expressed in neurons, glial cells, and multiple other cell types that comprise the nervous system. In the nervous system, several other IFs are expressed including nestin, synemin, glial fibrillary acidic protein (GFAP). These IFs, in addition to vimentin, are upregulated during astrocyte activation (24). In *Vim*$^{-/-}$ mice subjected to neurotrauma, astrocytes are less reactive and less migratory than those of WT mice (25, 26). Additionally, these mice display slower neurite outgrowth and take longer to recover sensation following sciatic nerve injury (27). GFAP can play a compensatory role in the absence of vimentin; therefore, to best evaluate the effects of vimentin in

the nervous system, many studies utilize *GFAP*$^{-/-}$*Vim*$^{-/-}$ mice (28, 29). These mice display less astrocyte reactivity and slower wound healing than WT mice (25, 29) . They are also unable to resist mechanical stress to the central nervous system and are more susceptible to ischemia (30-35). *GFAP*$^{-/-}$*Vim*$^{-/-}$ mice display less Notch signaling between astrocytes and neural stem cells, making them less likely to undergo adult neurogenesis (36, 37). Compared to WT mice, *GFAP*$^{-/-}$*Vim*$^{-/-}$ mice also exhibit a metabolic difference: in the double knockout, astrocytes have decreased glutamine, impaired glutamate transport, and lower resistance to oxidative stress, suggesting that vimentin and GFAP are required for the neuroprotective effects of astrocytes following ischemic stroke (33, 34, 38). Relatedly, *GFAP*$^{-/-}$*Vim*$^{-/-}$ mice are also more susceptible to models of Alzheimer's and Batten disease (39-41). In contrast, in an unchallenged *GFAP*$^{-/-}$*Vim*$^{-/-}$ mouse model, hippocampal neurogenesis is increased compared to WT mice (37, 42). Furthermore, these mice display increased neurogenesis following ischemia and neurotrauma, along with elevated regeneration of neuronal axons and synapses (25, 43, 44). Therefore, vimentin seems to act as both a protective and deleterious protein in the nervous system.

One of the earliest defects identified in the *Vim*$^{-/-}$ mice was their inability to properly heal wounds (45, 46). Embryos from *Vim*$^{-/-}$ mice fail to heal wounds as rapidly as WT embryos. In adult mice, healing times are delayed in *Vim*$^{-/-}$ mice compared to WT mice (45). This wound healing defect is not injury specific; interestingly, excision, incision, and burn wounds all heal more slowly in *Vim*$^{-/-}$ mice compared to WT mice (46). This impaired wound healing response illustrates an important role for vimentin in regulating cell motility. Following injury, *Vim*$^{-/-}$ mice exhibit delayed fibroblast migration to the wound site, resulting in impaired wound contraction (45). Further characterization of the fibroblast compartment highlights a role for vimentin in conferring proper functions. Fibroblasts isolated from *Vim*$^{-/-}$ mouse embryos (MEFs) are less motile, less mechanically stable, and undergo less directional migration (47). The requirement of vimentin for proper cell

migration is intimately tied to its relationship with the actin cytoskeleton. Vimentin IFs (VIFs) restrict the retrograde flow of actin which controls the size of lamellipodia and location of the nucleus during migration (48). This control of actin flow serves as a buffer for traction forces (49). Vimentin mediates actin stress fiber formation via RhoA activation (50). Vimentin works with actin to execute wound healing signaling events.

When the normal wound healing process is dysregulated, tissue fibrosis can occur. Specifically, this process is characterized by excess deposition of collagen through activation of myofibroblasts, leading to tissue stiffening, disrupted tissue architecture, and organ dysfunction. Fibrosis is initiated by tissue injury that can be caused by a range of pathophysiological insults. For example, lung fibrosis can be initiated by exposure to bleomycin, asbestos, viral, or bacterial agents. *Vim*$^{-/-}$ mice are protected from lung fibrosis following each of these challenges (51). This is due, in part, to decreased TGF-β signaling in *Vim*$^{-/-}$ mice. TGF-β is a critical profibrogenic cytokine that potentiates the development of fibrosis in a range of tissues. TGF-β signals through Smad to upregulate vimentin in mouse alveolar cells to initiate epithelial-to-mesenchymal transition (EMT). Inversely, inhibiting TGF-β receptor signaling leads to decreased vimentin expression which causes alveolar cells to undergo mesenchymal-to-epithelial transition (MET) (52-54). Together, these studies show that vimentin is required for expansion of mesenchymal cells during the fibrosis disease course.

Excessive collagen deposition is a hallmark of fibrosis and is produced by activated mesenchymal cells (fibroblasts and myofibroblasts). When challenged with profibrogenic agents, *Vim*$^{-/-}$ mice produce lower levels of collagen than WT mice (51). This results in improved lung function in *Vim*$^{-/-}$ mice because they are able to maintain lung compliance. When challenged with a unilateral ureteral obstruction, a model used to reproduce renal fibrosis, *Vim*$^{-/-}$ mice display improved outcomes compared to WT mice (55). These mice deposit significantly less collagen in the

kidneys compared to WT mice. These results are likely due to the role of VIFs as stabilizer for collagen mRNAs; without stabilization, these mRNAs are quickly degraded and are therefore unable to be translated, offering a potential explanation for the decreased collagen deposition observed in *Vim*$^{-/-}$ mice (56).

Along with mechanisms involving the role of vimentin in mesenchymal cells, immune cells rely on vimentin to promote inflammatory responses. For leukocytes to successfully traffic to tissues, they must first adhere to the blood vessel wall. This adhesion relies on formation of microvilli on both leukocytes and endothelial cells. Microvilli are enriched in vimentin but not other cytoskeletal proteins like actin or tubulin (57). In *Vim*$^{-/-}$ mice, lymphocyte trafficking to peripheral lymph nodes and the spleen is reduced compared to WT mice. This is likely due to reduced expression of ICAM-1 and VCAM-1 on endothelial cells in *Vim*$^{-/-}$ mice. These molecules are required for leukocyte docking; without their proper expression, *Vim*$^{-/-}$ leukocytes cannot polarize and move across the endothelial barrier (57). During extravasation, VIFs are reorganized to allow for mechanical deformation of the cell through pores in the endothelium (58). Mechanistically, Pi3K-Akt signaling causes this reorganization and is required for extravasation (59). In macrophages, vimentin is localized to filopodia and podosomes, two structures required for directional migration and extravasation *in vivo* (60). Additionally, vimentin complexes with fimbrin, an adhesion molecule which crosslinks actin during filopodia formation (61). Together, vimentin plays an important role in coordinating cellular events that allow for leukocyte trafficking.

Mechanistically, vimentin coordinates signaling events in immune cells. Vimentin is required for assembly of the NLRP3 inflammasome which coordinates secretion of IL-1β (51, 62). Lipopolysaccharide (LPS), a potent activator of the NLRP3 inflammasome, causes a strong inflammatory response leading to tissue injury. *Vim*$^{-/-}$ mice are protected from LPS-induced lung injury (51). This effect is myeloid cell specific; adoptive transfer of bone marrow from *Vim*$^{-/-}$ mice

to WT mice is sufficient to protect the mice from injury by preventing IL-1β secretion. Additionally, VIFs interact directly with macrophage inhibitory factor, a molecule required for NLRP3 inflammasome activation (63). These studies suggest a scaffolding role for vimentin in inflammasome activation.

Regulatory T cells (Tregs) may rely on vimentin to suppress pro-inflammatory responses. Tregs are a subpopulation of CD4+ T cells that suppress immune activation via an interaction with antigen-presenting cells (APCs). During this interaction, vimentin expression is upregulated and VIFs localize to the distal pole complex (DPC) of Tregs, suggesting that they may play an activating role in Treg function (64). Interestingly, in a murine model of graft-versus-host disease (GvHD), vimentin-knockdown Tregs better suppress alloreactive T cell priming that WT controls (65). Specifically, vimentin is a protein kinase C-θ (PKC-θ) phosphorylation target; during T cell polarization, PKC-θ accumulates on the vimentin-rich DPC. Because of its rapid reorganization and ability to bind PKC-θ, vimentin may play a signaling role in Treg activation.

Vimentin affects the oxidative state of cells. Reactive oxygen species (ROS) are present at low levels under homeostasis, where they are used as signaling moieties. ROS levels can increase due to endogenous factors like mitochondrial respiration or exogenous factors like pollutants or ionizing radiation. High levels of ROS lead to damage to DNA and RNA, lipid peroxidation, and oxidation of amino acids, which can cause protein damage, inflammation, and cell death. Interestingly, *Vim*$^{-/-}$ macrophages produce higher levels of ROS than WT macrophages (66). Nitric oxide, another inducer of oxidative stress, is decreased in *Vim*$^{-/-}$ mice compared to WT mice following partial nephrectomy (22). The protective or deleterious relationship between vimentin and oxidative stress is not yet fully characterized, and it likely differs between cell types and tissues.

The vasculature in *Vim*$^{-/-}$ mice is distinct from that of WT mice. *Vim*$^{-/-}$ embryos develop fewer vessels with less branching (67). Embryonic stem cells *Vim*$^{-/-}$ mice display impaired differentiation to endothelial cells (68). Additionally, VEGF treated aortas from *Vim*$^{-/-}$ mice undergo sprout fewer and smaller blood vessels than WT mice. When subject to shear stress, the vasculature of *Vim*$^{-/-}$ mice display impaired arterial remodeling and smooth muscle cell differentiation (69). Mechanistically, this effect is due to the ability of vimentin to modulate Notch signaling strength; shear stress leads to phosphorylation of vimentin, which allows it to bind Jagged1. This interaction between vimentin and Jagged1 regulates Notch activation potential, contributing to proper remodeling of the arterial wall. Additionally, vimentin interacts with focal adhesions and the actomyosin network (70, 71). This interaction allows for rapid reorganization of VIFs in response to shear flow, suggesting that vimentin plays a role in mechanotransduction in response to shear force (72). Relatedly, *Vim*$^{-/-}$ mice display impaired endothelial barrier function (57, 67). Vimentin rearranges in response to hemodynamic stress and participates in proangiogenic signaling; therefore vimentin is required for mechanical maintenance of endothelial function.

Vimentin has unique biophysical properties that may contribute to its role as a signaling protein. Early studies characterized the viscoelastic properties of vimentin *in vitro* (73, 74). Vimentin polymers undergo strain stiffening; as shear stress increases, they harden and resist rupture. Single nonstabilized vimentin filaments have a bending modulus between 300 and 400 mPa (75). This property allows vimentin to be much more flexible than actin and microtubules. In skin fibroblasts, oncogene activation causes vimentin IFs to collapse, causing an increase in cell stiffness (76). Similarly, vimentin-null breast carcinoma cells are softer and less contractile than vimentin-expressing cells (77, 78). Vimentin increases stiffness of both the intracellular and the cortical region in MEFs and Schlemm's canal endothelial cells (79). The unique mechanical properties of vimentin contribute to its role in promoting cancer and fibrosis.

This thesis considers the role of vimentin as a signaling protein, mechanical regulator, and therapeutic target. In the next chapter, I show that vimentin is required for rapid progression of lung cancer. Mechanistically, vimentin regulates cell motility and metastasis and protects cells from ferroptosis, a form of regulated cell death. In Chapter 3, I characterize the role of vimentin in platelet function, showing that vimentin increases viscoelasticity and contraction in blood clots. These properties allow for rapid clotting in WT, but not *Vim*$^{-/-}$, mice. In Chapter 4, I describe a nanocarrier that can target vimentin in macrophages and show proof-of-principle evidence that this particle suppresses IL-1β *in vitro*. Finally, in Chapter 5, I discuss future directions for characterizing the requirement of vimentin in fibrosis and delineating its possible role as a mechanosensor. Together, I provide robust evidence that vimentin plays a critical role in a variety of disease contexts.

Chapter 2. Vimentin is required for lung cancer progression and metastasis.

2.1 Background

Lung adenocarcinoma (LUAD) is a type of non-small cell lung cancer (NSCLC) and is the jmost common subtype of lung cancer, representing 40% of all lung cancers diagnoses (80). Vimentin, a type III intermediate filament, is highly expressed in lung cancer and is associated with metastatic tissue and lower survival rates in patients with NSCLC (81-83). Despite this association, a causal, *in vivo* link between vimentin and disease progression has not been established.

Vimentin's role in the metastatic process has been extensively investigated *in vitro*. During epithelial-to-mesenchymal transition (EMT) epithelial cells lose their apicobasal polarity and intercellular adhesion properties by downregulating epithelial cell-associated genes, including E-cadherin and cytokeratins, and progressively acquire migratory and invasive capabilities associated with the mesenchymal cell phenotype by upregulating genes, such as N-cadherin and vimentin (84, 85). EMT-mediated tumor metastasis is stimulated by transcription factors, such as TWIST1, SNAI1, and ZEB1, known to upregulate vimentin (77, 86-88). Formation and elongation of the invadopodia, a proteolytically active plasma membrane projection that facilitates cancer cell invasion across the basement membrane and migration through the collagen-rich interstitial space, requires vimentin (89). Vimentin is crucial for establishing front-rear polarity, which is necessary for the efficient migration of tumor cells (10). Previous studies identified these vimentin-dependent mechanisms for driving cancer cell invasive migration, promoting metastasis, and poor prognosis in patients with lung, breast, head and neck, and bone cancer cells (77, 78, 90-97).

Tumors must maintain redox homeostasis to survive and grow. An emerging mechanism by which tumor cells manage oxidative stress is ferroptosis. Ferroptosis is a form of iron-dependent regulated cell death (RCD) initiated by the peroxidization of phospholipids (PL) containing

polyunsaturated fatty acid chains (PUFA-PLs). Ferroptosis can be induced through extrinsic or intrinsic pathways (98). The extrinsic pathway is initiated by inhibiting cell membrane transporters, such as the system Xc− cystine/glutamate transporter (consisting of SLC7A11 and SLC3A2 subunits) or through iron uptake via transferrin and lactotransferrin transporters. The intrinsic pathway is activated by blocking intracellular antioxidant enzymes, such as glutathione peroxidase 4 (GPX4). Glutathione serves as a cofactor for GPX4 to neutralize lipid hydroperoxides and protect the cell from ferroptosis. KRAS-mutant LUAD cells express high levels of SLC7A11 and GPX4, and pharmacological or genetic inhibition of either attenuates tumor growth *in vivo* (99, 100). Of note, the regulation of ferroptosis is not entirely understood.

While previous studies established a role for vimentin in cancer cells, these experiments relied on either cell lines treated with exogenous agents to suppress vimentin expression or used cells derived from vimentin knockout ($Vim^{-/-}$) mice that lack oncogene activation. Therefore, in the present study, we used the clinically-relevant *LSL-Kras*^{G12D}; *Tp53*$^{fl/fl}$ ($KPV^{+/+}$) genetically engineered mouse model (GEMM), which reliably recapitulates human NSCLC in pathology, disease progression, clinical outcome, and response to therapies (101). To identify the role of vimentin in LUAD, we crossed the *LSL-Kras*^{G12D}; *Tp53*$^{fl/fl}$ with $Vim^{-/-}$ mice, thereby creating $KPV^{-/-}$ mice (12). We show that $KPV^{-/-}$ mice have reduced lung tumor burden and increased survival rates compared to $KPV^{+/+}$ mice. Using a second pharmacological method of vimentin disruption, we show that withaferin A (WFA) treatment decreases $KPV^{+/+}$ mouse tumor burden when administered therapeutically. Finally, we use an allograft tumor model to demonstrate that $KPV^{-/-}$ cells are unable to metastasize to the lung. Compared to $KPV^{+/+}$ cells, $KPV^{-/-}$ cells display impaired EMT and increased susceptibility to ferroptosis. Together, we show that an intact vimentin intermediate filament network is required for the rapid progression and metastasis of LUAD.

2.2 Results

2.2.1 Generation of an LSL-Kras$^{G12D/+}$;*Tp53*$^{fl/fl}$;Vim$^{-/-}$ (KPV$^{-/-}$) genetically engineered mouse model

In patients with LUAD, 30% have activating mutations in the *Kras* proto-oncogene, and 60% have inactivating mutations in the tumor suppressor gene *Tp53* (102-105). Therefore, we used the *LSL-Kras*$^{G12D/+}$;*Tp53*$^{fl/fl}$ (*KPV*$^{+/+}$) GEMM to recapitulate the tumorigenesis and metastasis observed in LUAD (101). When adenoviral Cre recombinase (Ad-Cre) is delivered intratracheally to *KPV*$^{+/+}$ mice, tumors develop as early as 2 weeks post-infection (w.p.i.) (101), with ~50% of mice developing metastatic lesions in the mediastinal lymph nodes and the pleural spaces of the thoracic cavity (106). We crossed the *Vimentin*$^{-/-}$ mouse to the *LSL-Kras*$^{G12D/+}$;*Tp53*$^{fl/fl}$ mouse to create the *KPV*$^{-/-}$ mouse (12) (**Figure 2.1A**).

This novel *KPV*$^{-/-}$ mouse lacks vimentin expression throughout the lungs (**Figure 2.1B**). *Rosa26-LSL-LacZ* reporter mice were used to validate the intratracheal delivery of Ad-Cre (107). Mice infected with Ad-Cre demonstrated homogenous, positive lacZ expression, while mice treated with the adenoviral null construct (Ad-null) did not express lacZ (**Figure 2.1C**). Ad-Cre was administered intratracheally, and disruption of the *Kras* allele and accumulation of mutant KRAS protein was validated by PCR and Western blot, respectively (**Figure 2.1D-E**). Similarly, p53 deletion was confirmed by qPCR and Western blot (**Figure 2.1F-G**). These results demonstrate the utility of a novel *KPV*$^{-/-}$ GEMM to define a causal role of vimentin in lung adenocarcinoma metastasis.

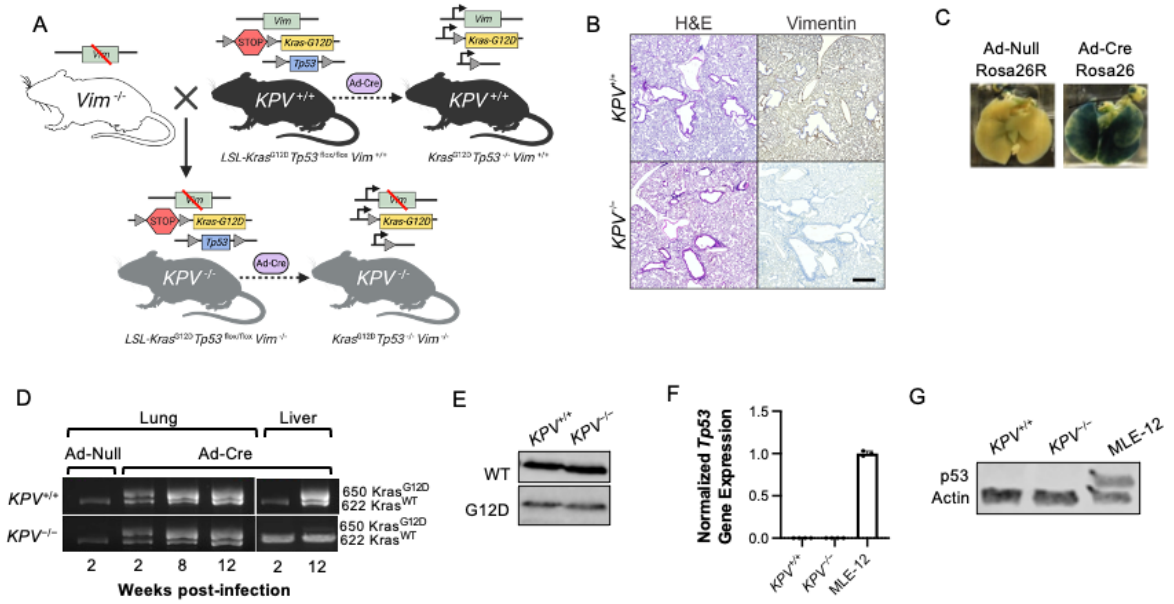

Figure 2.1. Generation of a genetically engineered mouse model to study the role of vimentin in non-small cell lung cancer progression. Experimental design. *LSL-Kras*$^{G12D/+}$*Tp53*$^{flox/flox}$ (*KPV*$^{+/+}$) mice were crossed with vimentin-knockout (*Vim*$^{-/-}$) mice. *KPV*$^{+/+}$ and *KPV*$^{-/-}$ mice were administered adenoviral Cre recombinase (Ad-Cre) which resulted in gene recombination at LoxP sites. As a control, null adenovirus (Ad-null) was administered to an independent cohort of mice. (**B**) Lungs were isolated from Ad-null-treated *KPV*$^{+/+}$ and *KPV*$^{-/-}$ mice, fixed, sectioned, and subjected to H&E staining and vimentin immunohistochemical staining. Positive vimentin staining is brown, and nuclei are blue. Scale bar: 200 µm. (**C**) *Rosa26-LSL-LacZ* reporter mice were administered Ad-Null or Ad-Cre, and β-galactosidase staining was performed on whole lung samples; positive staining appears blue. (**D**) *KPV*$^{+/+}$ and *KPV*$^{-/-}$ mice were administered Ad-Null or Ad-Cre. Lungs were harvested at 2, 8, and 12 weeks following adenoviral infection. DNA was isolated from the tissue and PCR was performed to evaluate the presence of the wild-type (WT) and mutant (G12D) *Kras* transcript. (**E**) Tumor cells were isolated from Ad-Cre-infected mice at 6 weeks post-infection. A Western blot was performed on *KPV*$^{+/+}$ and *KPV*$^{-/-}$ whole cell lysates to detect WT and G12D-mutant KRAS. P53 mRNA (**F**) and protein levels (**G**) were detected through qRT-PCR and Western blot, respectively; MLE-12 cells were used as a positive control. Data are presented as the mean ± standard deviation.

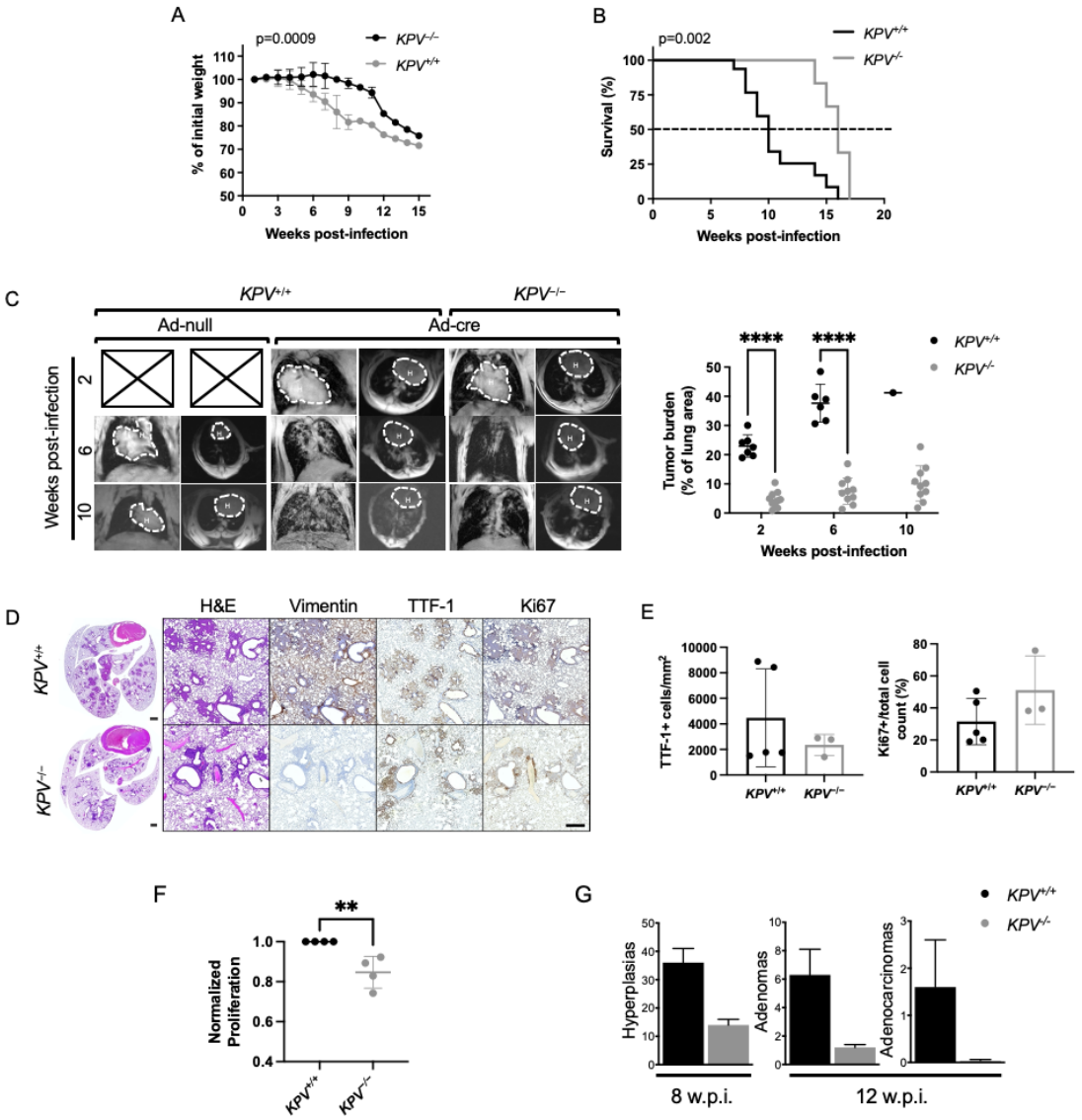

Figure 2.2. Vimentin-null mice have reduced tumor burden and improved survival in a preclinical *LSL-Kras^{G12D}Tp53$^{fl/fl}$*-driven mouse model of lung cancer. *LSL-Kras^{G12D}Tp53$^{fl/fl}$* (*KPV$^{+/+}$*) mice were crossed with *Vim$^{-/-}$* mice to produce *KPV$^{-/-}$* mice, then *KPV$^{+/+}$* and *KPV$^{-/-}$* mice were intubated with 10^9 PFUs of adenoviral Cre. (**A**) Weight loss (n=6 mice for *KPV$^{+/+}$* group; n=7 mice for KPV$^{-/-}$ group; mixed model ANOVA, for *KPV$^{+/+}$* versus *KPV$^{-/-}$*, p=0.0009) and (**B**) survival (n=15 mice for *KPV$^{+/+}$* group; n=10 mice for *KPV$^{-/-}$* group; Mantel-Cox log-rank test, p=0.002) were monitored. (**C**) *KPV$^{+/+}$* and *KPV$^{-/-}$* mice were infected with null or Cre recombinase adenovirus (Ad-Null and Ad-Cre, respectively) and were imaged at 2, 6, and 10 weeks post-infection (w.p.i.). Representative MRI coronal (*left*) and transverse (*right*) images are shown. Hearts (H) are outlined in white. Tumor burden was quantified using Jim software (*right*). Each point represents one mouse (****p<0.0001 by unpaired, two-tailed t-test). (**D**) Lungs were isolated from *KPV$^{+/+}$* mice (6 weeks post-infection shown) and *KPV$^{-/-}$* mice (7 weeks post-infection shown) infected with 10^9 PFUs of adenoviral Cre. Shown from left to right are representative fixed whole lung sections with H&E staining and close-up views of fixed lung sections with H&E staining and vimentin, TTF-1, and Ki67 immunohistochemical staining. Positively immunostained cells appear brown, and nuclei are dyed blue. Scale bars: 1 mm (whole lungs, *left*), 200 μm (*right*). (**E**) Positive staining was quantified from lung sections stained with either TTF-1 or Ki67 and normalized to either total lung area (TTF-1) or total tumor cell count (Ki67) (n=2-5). (**F**) *KPV$^{+/+}$* and *KPV$^{-/-}$* cells were plated overnight and were then treated with BrdU for 4 hours. BrdU incorporation was detected and normalized to the *KPV$^{+/+}$* condition for each independent trial (n=4). Data were compared using an unpaired, two-tailed t-test (**p<0.01). (**G**) H&E-stained lung sections from 8 or 12 w.p.i. were evaluated for tumor grade by a pathologist. This figure represents combined data from three independent experiments.

2.2.2 Vimentin deficiency increases survival and reduces tumor burden

Cancer cachexia is a common manifestation of morbidity in human cancer patients and is associated with a poor prognosis in patients with advanced disease. *KPV*$^{+/+}$ and *KPV*$^{-/-}$ mice were administered Ad-Cre, and their weight was recorded weekly. *KPV*$^{+/+}$ mice showed a rapid and profound decline in total body weight starting at 4 w.p.i., while *KPV*$^{-/-}$ mice did not exhibit weight loss until 9 w.p.i., suggesting less advanced disease in the vimentin-deficient mice (**Figure 2.2A**). *KPV*$^{-/-}$ mice lived significantly longer than *KPV*$^{+/+}$ mice, with a median survival of 15.5 w.p.i. compared to 10 w.p.i. in the *KPV*$^{+/+}$ mice (**Figure 2.2B**). Lung tumor development was assessed using Magnetic Resonance Imaging (MRI). At 6 w.p.i., *KPV*$^{-/-}$ mice had an average lung tumor burden of 7.5%, significantly lower than the 37% tumor burden observed in *KPV*$^{+/+}$ mice (**Figure 2.2C**). Immunohistochemistry (IHC) staining for vimentin, TTF-1, and Ki67 was performed on serial sections of lung tissue from *KPV*$^{+/+}$ and *KPV*$^{-/-}$ mice at 6 w.p.i. Vimentin was expressed in *KPV*$^{+/+}$ tumors and normal adjacent lung tissue but was not expressed in *KPV*$^{-/-}$ lung tissue (**Figure 2.2D**). TTF-1 is a biomarker associated with LUAD (108). *KPV*$^{-/-}$ lungs had fewer TTF-1-positive cells than *KPV*$^{+/+}$ lungs (**Figure 2.2D-E**). *KPV*$^{+/+}$ and *KPV*$^{-/-}$ lung tumors displayed similar levels of Ki67 staining by IHC (**Figure 2.2D-E**). However, *KPV*$^{+/+}$ cells had increased proliferation rates, as quantitatively measured by BrdU incorporation, compared to *KPV*$^{-/-}$ cells isolated from primary lung tumors 6 w.p.i. (**Figure 2.2F**). At 8 w.p.i., *KPV*$^{+/+}$ mice displayed significantly more hyperplastic lesions than *KPV*$^{-/-}$ mice (36 ± 5 vs. 14 ± 2, respectively). At 12 w.p.i., *KPV*$^{+/+}$ mice displayed an increased number of adenomas and adenocarcinomas (6.3 ± 1.8 adenomas and 1.2 ± 0.2 adenocarcinomas per *KPV*$^{+/+}$ mouse) compared to *KPV*$^{-/-}$ mice (1.6 ± 1.0 adenomas and 0.04 ± 0.02 adenocarcinomas per *KPV*$^{-/-}$ mouse) (**Figure 2.2G**). Additionally, mutant *Kras* transcripts were detected in liver tissue from *KPV*$^{+/+}$ mice, but not *KPV*$^{-/-}$ mice, suggesting that vimentin-expressing cells form metastatic lesions (**Figure 2.1D**). Together, these data indicate that loss of vimentin suppresses tumor development in a murine model

of LUAD, contributing to prolonged survival. In agreement with these findings, we observed that vimentin protein increases with tumor grade in human LUAD sections and corresponding lymph node sections that contained LUAD metastatic lesions (**Figure 2.3**).

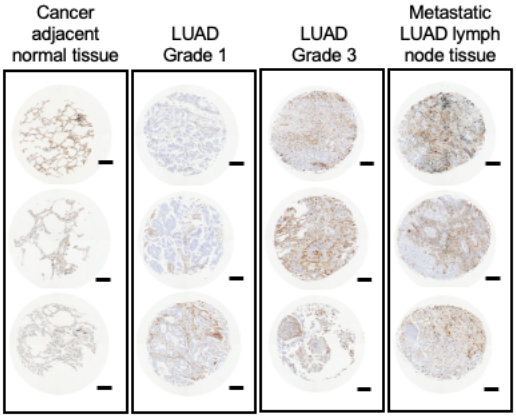

Figure 2.3. Vimentin expression correlates with lung adenocarcinoma grade. Human lung tissue sections (or lymph node tissue where indicated) were stained with antibodies against vimentin. LUAD=lung adenocarcinoma. Positive vimentin staining is brown, and nuclei are blue. Scale bar: 200 μm.

2.2.3 Transcriptional profiling reveals a less differentiated cancer phenotype in vimentin-null cancer cells

To better understand how vimentin is involved in the molecular pathways of LUAD, we used RNA sequencing (RNA-seq) to identify genes that have altered expression in the absence of vimentin. Epithelial-derived cancer cells (CD45-negative, EpCAM-positive) were isolated from *KPV*$^{+/+}$ and *KPV*$^{-/-}$ lungs at 6 w.p.i. with Ad-Cre (hereafter referred to as *KPV*$^{+/+}$ and *KPV*$^{-/-}$ cells). The absence of vimentin in *KPV*$^{-/-}$ cells was confirmed by Western blot and immunofluorescence staining (**Figure 2.4A-B**). We isolated messenger RNA (mRNA) from *KPV*$^{+/+}$ and *KPV*$^{-/-}$ cells and performed RNA-seq. *KPV*$^{+/+}$ and *KPV*$^{-/-}$ cells clustered together by genotype via principal component analysis (PCA). Loss of vimentin in *KPV*$^{-/-}$ cells was the main driver of sample variance (PC1: 97.6%) (**Figure 2.4C)** and Pearson's correlation revealed minimal variance in intragroup replicates (**Figure 2.4D**). We identified 904 differentially expressed genes (DEGs) between the *KPV*$^{+/+}$ and *KPV*$^{-/-}$ cells (**Figure 2.4E**). Using k-means clustering, we defined two clusters that correspond to 316 upregulated genes (Cluster 1) and 588 downregulated genes (Cluster 2) in *KPV*$^{+/+}$ cells compared to *KPV*$^{-/-}$ cells (**Figure 2.5A**). Cluster 1 was enriched for genes associated with Gene Ontology (GO) processes *mesenchymal cell proliferation* and *cell migration*. In contrast, Cluster 2 was enriched for genes associated with *metabolic processes, epithelial*

cell differentiation and *cell adhesion* (**Figure 2.5B**). By exploring the DEGs that contribute to *mesenchymal cell proliferation* and *epithelial cell differentiation*, we found several EMT-associated genes upregulated in $KPV^{+/+}$ cells, including *Vimentin, Twist1* and *Cdh2,* the gene that codes for N-cadherin (**Figure 2.5C**). This finding was confirmed by IHC of tumors and Western blots on isolated tumor cells, which showed an increase in N-cadherin in $KPV^{+/+}$ cells compared to $KPV^{-/-}$ cells (**Figure 2.4A, 2.6A-B**). In contrast, genes associated with epithelial cell phenotype, including claudins *Cldn2, Cldn8,* and *Cldn18,* and the epithelial marker *Epcam* and the surfactant protein *Sftpd*, were upregulated in $KPV^{-/-}$

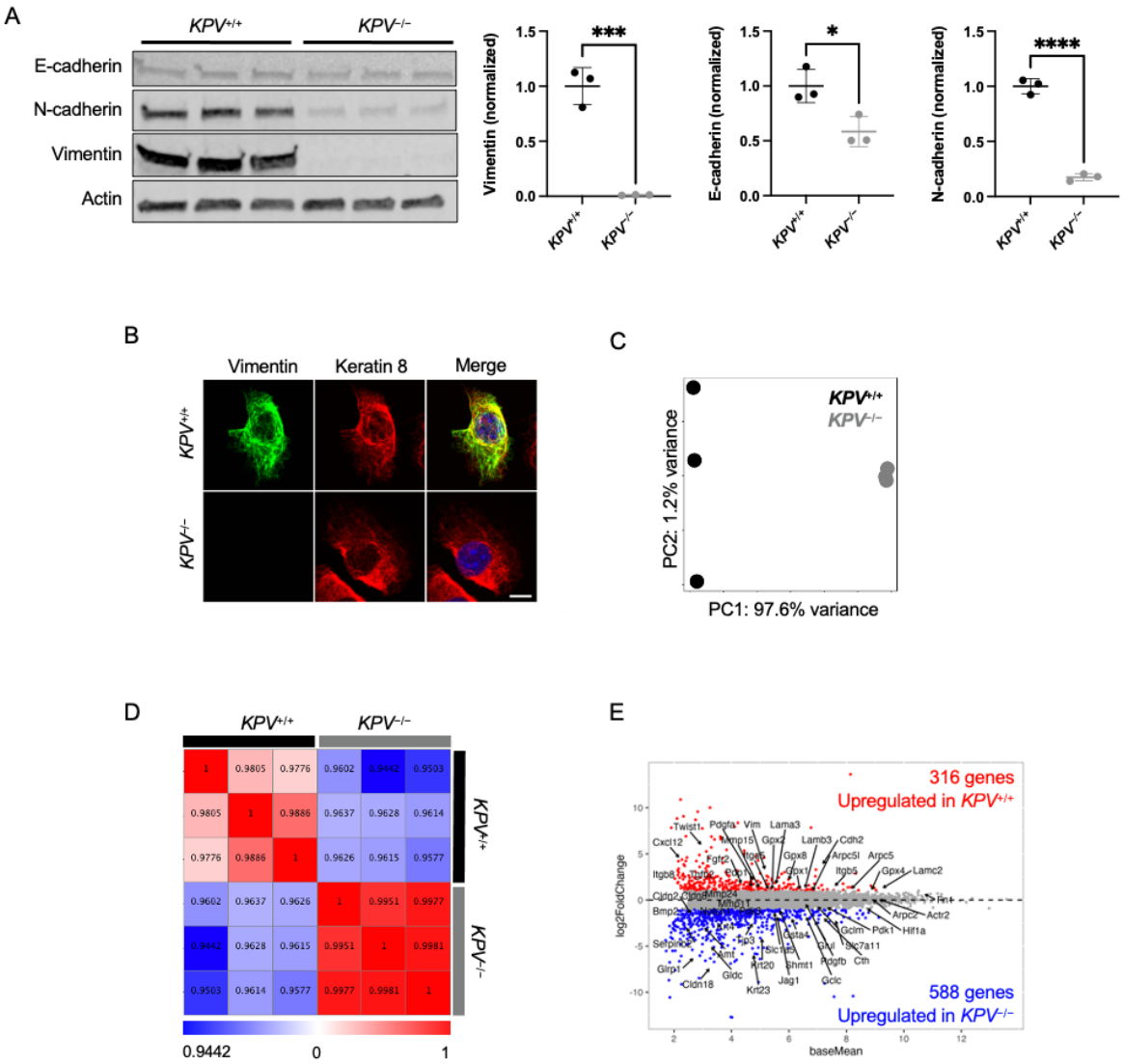

Figure 2.4. *KPV*$^{-/-}$ cells retain epithelial marker expression. (**A**) *KPV*$^{+/+}$ and *KPV*$^{-/-}$ cell lysates were subjected to a Western blot for detection of E-cadherin, N-cadherin, vimentin, and actin. Band signal was quantified and normalized to actin loading controls and average *KPV*$^{+/+}$ signal. Data were compared using an unpaired, two-tailed t-test (*p<0.01; ***p<0.001; ****p<0.0001). (**B**) *KPV*$^{+/+}$ and *KPV*$^{-/-}$ cells were stained for vimentin (*green*), for keratin 8 (*red*), and with Hoechst nuclear dye (*blue*). Scale bar: 10 µm. (**C-E**) Messenger RNA from *KPV*$^{+/+}$ and *KPV*$^{-/-}$ cell lysates was quantified via RNA sequencing. (**C**) Principal component analysis (PCA) plot with each point representing one replicate (*black, KPV*$^{+/+}$; *grey, KPV*$^{-/-}$). (**D**) Pearson's correlation plot. The correlation coefficient for each comparison is shown. (**E**) MA plot. Genes of interest are indicated.

cells. These data suggest that *KPV*$^{-/-}$ cells, but not *KPV*$^{+/+}$ cells, fail to upregulate key mesenchymal genes that confer metastatic potential.

We then explored the DEGs that contribute to the GO processes *cell motility* and *cell migration,* processes enriched in $KPV^{+/+}$ cells. Cells must form invadopodia, a process that relies on vimentin, to cross the basement membrane (89). Accordingly, invadopodia-associated genes (*Arpc2, Arpc5, Arpc5l,* and *Actr2*) are significantly downregulated in $KPV^{-/-}$ cells but upregulated in $KPV^{+/+}$ cells (**Figure 2.5C**). Invasion is potentiated by matrix metalloproteases (MMPs), which break down the basement membrane, allowing cells to move toward adjacent capillaries, a key process in the metastatic cascade. *Mmp11, Mmp15,* and *Mmp24* are significantly upregulated in $KPV^{+/+}$ cells, but not in the $KPV^{-/-}$ cells (**Figure 2.5C**). Cells must then migrate across a collagen-rich interstitial space to reach the bloodstream. This process is coordinated by chemokines (*Cxcl12*), integrins (*Itga5* and *Itgb5*), and alterations in the ECM (*Lama3, Lamb3, Lamc2,* and *Fn1*); these genes are significantly downregulated in $KPV^{-/-}$ cells compared to $KPV^{+/+}$ cells (**Figure 2.5C**). Together, these results suggest that vimentin is involved in regulating the early cellular events associated with the metastatic cascade.

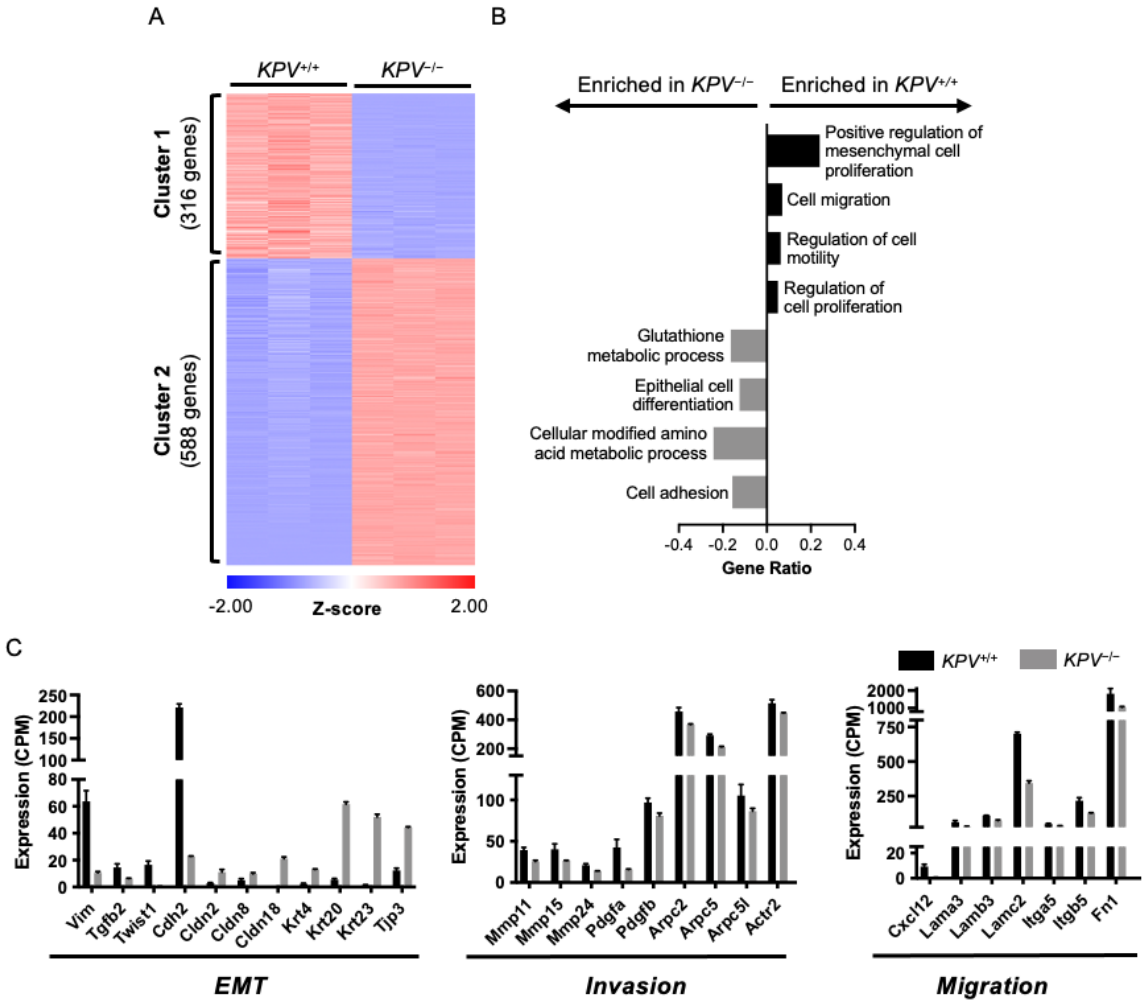

Figure 2.5. *KPV*$^{-/-}$ cells have decreased expression of genes involved in EMT. Messenger RNA collected from *KPV*$^{+/+}$ and *KPV*$^{-/-}$ cells was subjected to RNA sequencing. (A) Differentially expressed genes (DEGs) between *KPV*$^{+/+}$ and *KPV*$^{-/-}$ cells were clustered using K-means clustering. (B) Genes enriched in Cluster 1 (316 genes) and Cluster 2 (588 genes) were subjected to GO enrichment analysis. GO Processes with FDR<0.05 are shown. GeneRatio is the number of genes present in the cluster that are associated with the GO process divided by the total number of genes in that GO process. (C) Expression values (counts per million; CPM) of select genes are shown. N=3 for each group. Data in panel C are presented as the mean ± standard deviation. All gene comparisons shown (*KPV*$^{+/+}$ vs. *KPV*$^{-/-}$) have FDR<0.05 after adjusting for multiple comparisons; therefore, all gene differences shown between *KPV*$^{+/+}$ vs. *KPV*$^{-/-}$ cells are statistically significant.

2.2.4 An intact vimentin network is required for cancer cell migration and invasion

Given that cell motility pathways were downregulated in *KPV*$^{-/-}$ cells, we assessed whether cell-intrinsic motility properties required vimentin. Cell migration was evaluated using a scratch wound-healing assay. Within 6 hours, *KPV*$^{+/+}$ cells had closed ~76% more of the wound area than *KPV*$^{-/-}$

cells (72.71 ± 3.267% versus 17.71 ± 3.267%, **Figure 2.7A**). To test the invasive potential of $KPV^{+/+}$ and $KPV^{-/-}$ cells, a Matrigel-coated transwell assay was used to mimic invasion across the alveolar basement membrane. $KPV^{+/+}$ cells had a 16-fold increased rate of invasion compared to $KPV^{-/-}$ cells (invasive index, 230 ± 41.76 vs. 14.58 ± 2.68, respectively, **Figure 2.7B**). Three-dimensional invasion and migration were modeled by generating $KPV^{+/+}$ and $KPV^{-/-}$ spheroids. After 48 hours of culture in collagen, $KPV^{+/+}$ spheroids were 4.65 times larger than $KPV^{-/-}$ spheroids, suggesting that, in a three-dimensional model, $KPV^{-/-}$ cells have impaired migration and invasion (**Figure 2.7C**).

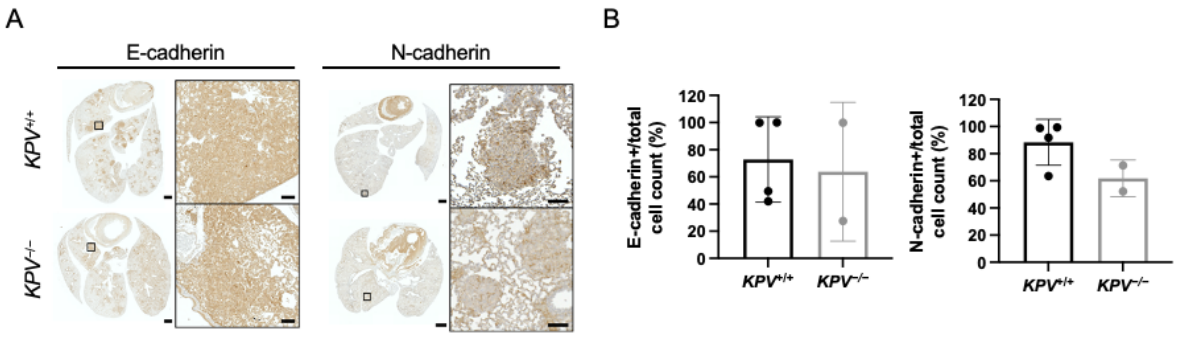

Figure 2.6. E-cadherin and N-cadherin expression in the lungs of $KPV^{+/+}$ and $KPV^{-/-}$ mice. (**A-B**) Lungs were harvested from $KPV^{+/+}$ and $KPV^{-/-}$ mice at 7 w.p.i., fixed, sectioned, and subjected to immunohistochemistry with antibodies against E-cadherin and N-cadherin. Scale bar: 1 mm (whole lung), 100 μm (insets). Representative images (**A**) and quantification (**B**) of positive staining are shown (n=2-5).

Withaferin A (WFA) is a steroidal lactone used as an anticancer agent in various murine tumor models, including breast, prostate, and ovarian cancer (109-111). WFA phosphorylates vimentin serine 38 (Ser38) and serine 56 (Ser56), resulting in the aggregation of vimentin intermediate filaments (IFs) (112). To test the hypothesis that WFA disrupts vimentin IFs and impairs migration and invasion *in vitro,* we treated $KPV^{+/+}$ cells and human lung adenocarcinoma (A549) cells with WFA (**Figure 2.8A-B**). In untreated cells, vimentin IFs were extended to the plasma membrane from the nucleus. In WFA-treated cells, vimentin IFs were retracted from the plasma membrane and collapsed around the nucleus (**Figure 2.8A-B).** There was no change in vimentin protein levels in cells treated with WFA

(**Figure 2.8C**) (113). WFA treatment decreased *KPV*$^{+/+}$ cell migration by ~46% (**Figure 2.8D**) and completely suppressed cell invasion (**Figure 2.8E**). We observed a similar trend in human-derived A549 cells, which exhibited a dose-dependent decrease in cell migration following treatment with WFA (**Figure 2.8F**). These data suggest that the vimentin intermediate filament network is required for migration and invasion in an *in vitro* model of NSCLC.

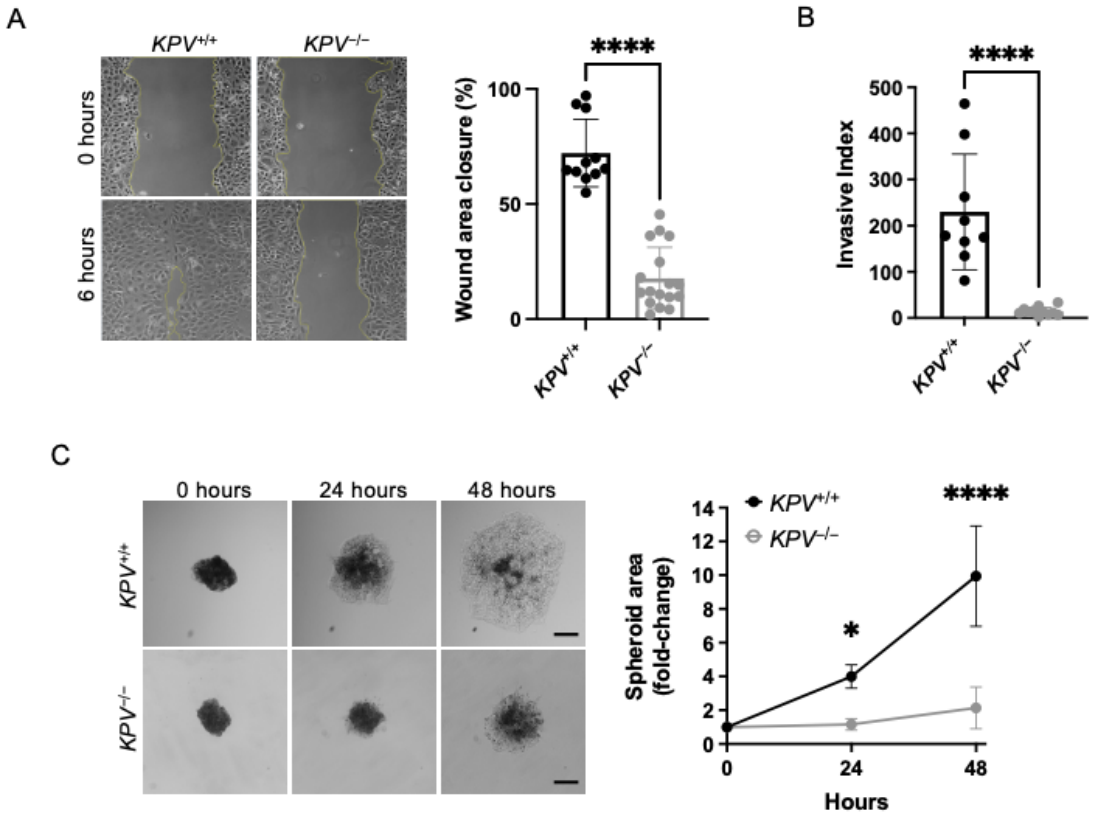

Figure 2.7. Vimentin is required for *in vitro* cancer cell migration and invasion. (**A**) A scratch wound assay was used to evaluate cell migration. Representative images are shown at 0 and 6 hours following scratch formation. Wound area closure was compared to the starting value and quantified for *KPV*$^{+/+}$ (n=11) and *KPV*$^{-/-}$ (n=17) cells; each point represents a separate scratch wound. (**B**) Cell invasion through a Matrigel-coated transwell was measured over 48 hours. Invasive index is the mean number of cells invaded per 20× magnification imaging field. *KPV*$^{+/+}$ (n=9) and *KPV*$^{-/-}$ (n=11) cell invasion data are plotted so that each point represents data from a single transwell assay. (**C**) *KPV*$^{+/+}$ and *KPV*$^{-/-}$ spheroids were suspended in type I collagen and spheroid growth was tracked over 48 hours. Spheroid area was quantified relative to the initial area of each spheroid (n=4 independent experiments). Scale bar: 200 μM. Data are presented as the mean ± standard deviation. The p-values were calculated using an unpaired, two-tailed t-test, except for panel **C**, in which data were compared using a repeated-measure two-way ANOVA with multiple comparisons. (*p<0.05; **p<0.01; ***p<0.001; ****p<0.0001).

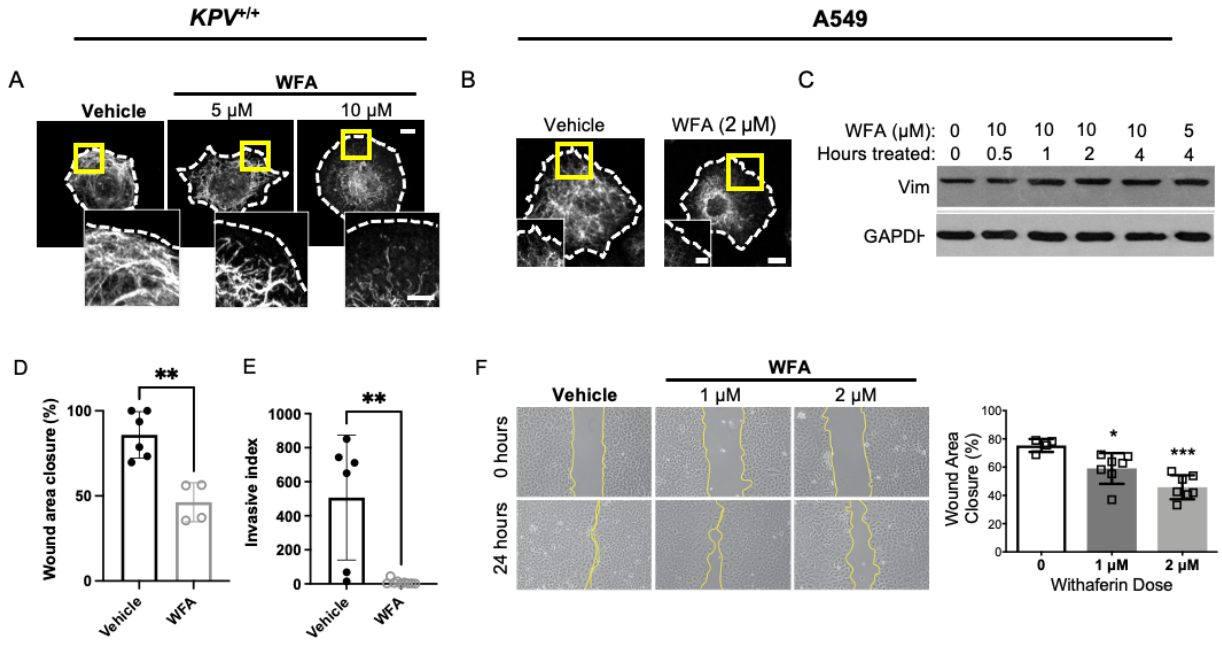

Figure 2.8. Withaferin A attenuates cancer cell migration and invasion. (**A-B**) *KPV*$^{+/+}$ (**A**) or A549 (**B**) cells were treated with withaferin A (WFA; 2, 5 or 10 μM) or DMSO vehicle control for 6 hours (*KPV*$^{+/+}$) or 1 hour (A549). Cells were stained for vimentin (white; dotted line represents cell outline). Scale: 10 μm; inset: 5 μm. (**C**) A549 cells were treated with WFA for the indicated dose and time and subject to a Western blot to detect vimentin and GAPDH. (**D**) *KPV*$^{+/+}$ cells were treated with vehicle (n=6) or 5 μM WFA (n=4) and were subjected to a scratch wound assay. Wound area was quantified at 6 hours. (**E**) KPV$^{+/+}$ cells were plated atop a Matrigel-coated transwell and were treated with vehicle control (n=6) or 5 μM WFA (n=9); invasion was quantified at 48 hours via invasive index as described above. (**F**) A549 cells were treated with DMSO control or with 1 or 2 μM WFA and were subjected to a scratch wound assay. After 24 hours, wound closure was assessed. Representative images (*left*) and quantitation (*right*) are shown. Data are presented as the mean ± standard deviation. The p-values were calculated using an unpaired, two-tailed t-test (*p<0.05; **p<0.01; ***p<0.001; ****p<0.0001).

2.2.5 Withaferin A treatment attenuates cancer progression

To determine whether WFA-mediated disruption of vimentin IF impairs LUAD progression, *KPV*$^{+/+}$ mice were administered WFA (4 mg/kg, QOD, p.o.) 2 weeks after Ad-Cre treatment to initiate tumor development (**Figure 2.9A**). At 6 w.p.i., WFA-treated *KPV*$^{+/+}$ mice developed smaller tumors (tumor burden, 15.65 ± 2.518%) than vehicle-treated mice (tumor burden, 25.1 ± 3.842%) (**Figure 2.9B**). Lungs sections were immunostained for vimentin, TTF-1, and Ki67 (**Figure 2.9C-D**). Lung tumors from vehicle-treated *KPV*$^{+/+}$ mice had enhanced TTF-1 and Ki67 expression. In contrast, WFA-treated mice had reduced tumor burden with diminished TTF-1 and Ki67 expression (**Figure 2.9C-D**). Additional lung tissue sections were stained with pSer56-vimentin antibody to assess the *in vivo*

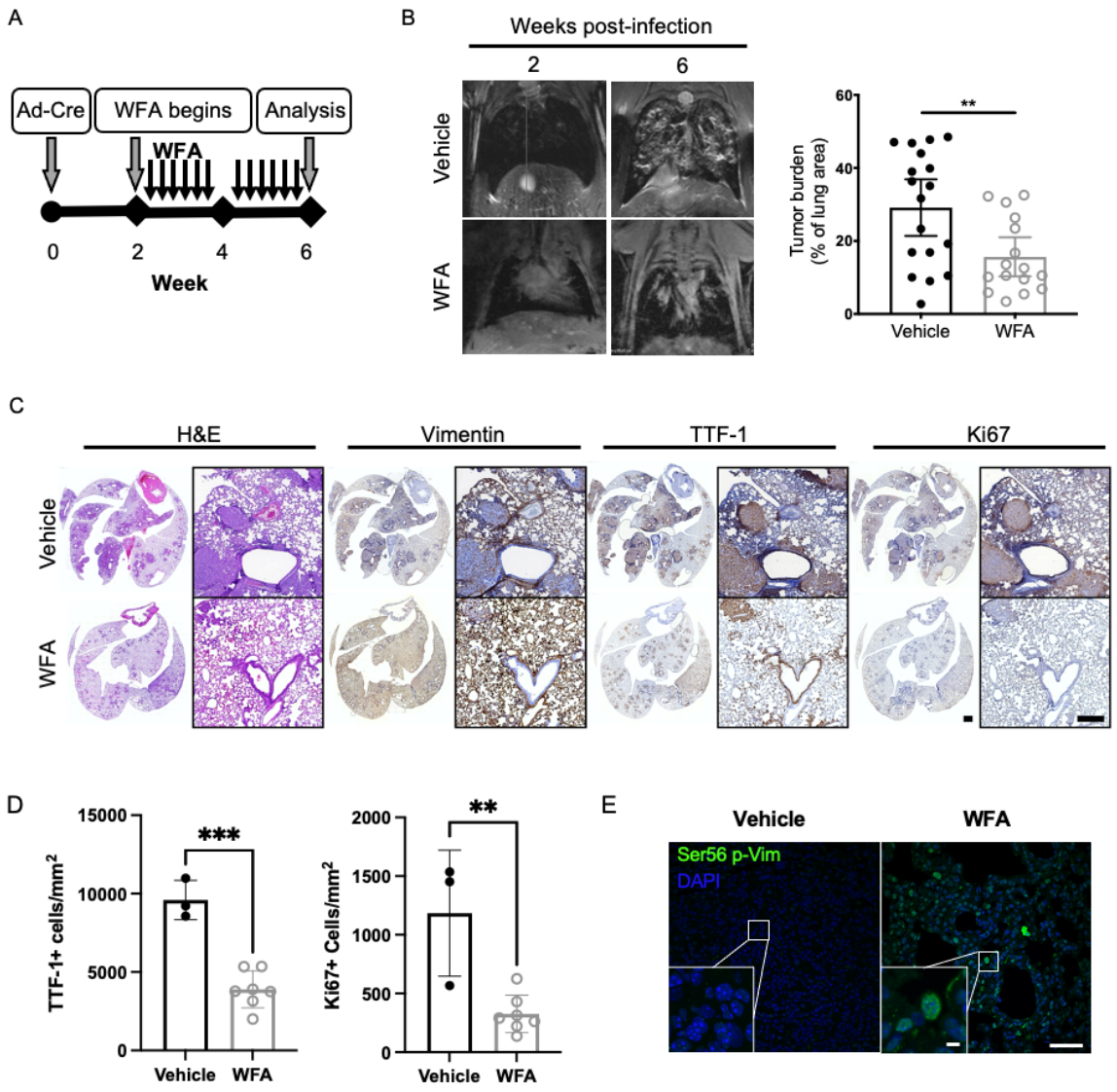

Figure 2.9. WFA treatment attenuates lung cancer progression. (**A**) Schematic of experimental design. *KPV*$^{+/+}$ mice were treated with withaferin A (WFA; 4 mg/kg; Q.O.D., p.o.) or vehicle control (DMSO) at 2 weeks post-infection with 10^7 PFUs of adenoviral Cre. (**B**) Representative MRI scans show WFA-treated *KPV*$^{+/+}$ lung tumors at 6 weeks post-infection with 10^7 PFUs of adenoviral Cre (*left*). Dot plot illustrates the tumor volume between WFA-treated or vehicle-treated control *KPV*$^{+/+}$ mice (*right*). Each point represents, for one mouse, the percentage of lung area on MRI occupied by tumor, as measured using Jim software. (**C**) Lungs isolated from vehicle- or WFA-treated KPV$^{+/+}$ mice at 6 weeks after adenoviral Cre infection were fixed, sectioned, and subjected to H&E staining and vimentin, TTF-1, and Ki67 immunohistochemical staining. Positively immunostained cells appear brown, and nuclei are dyed blue. Scale bars: 2 mm (whole lungs, *left*), 200 µM (*right*). (**D**) Slides were scanned and signal was quantified using Histoquest. TTF-1 and Ki67 were normalized to total lung area. Data were subject to an unpaired, two-tailed t-test (**p<0.01; ***p<0.001). (**E**) Lungs isolated from vehicle- and WFA-treated *KPV*$^{+/+}$ mice were sectioned and stained for phospho-Serine56 vimentin (green) and DAPI. Scale bar: 50 µm, 5 µm (*insets*). Data are presented as the mean ± standard deviation (**p<0.01, ***p<0.001 by unpaired, two-tailed t-test).

efficacy of WFA-mediated vimentin disassembly (114) (**Figure 2.9E**). Collectively, these data suggest that vimentin can be pharmacologically targeted *in vivo* to disrupt the ability of lung cancer cells to

invade and migrate away from the primary tumor.

2.2.6 Vimentin confers cancer cell protection from ferroptosis

KRAS-mutant lung adenocarcinoma cells were shown to be susceptible to SLC7A11 inhibitor-induced cell death, resulting in attenuated tumor growth *in vivo* (99). SLC7A11 and SLC3A2 make up the cystine/glutamine antiporter; this transporter brings cystine into the cell, where it is immediately converted to cysteine, the rate-limiting precursor of the antioxidant glutathione. $KPV^{-/-}$ cells express much higher levels of *Slc7a11* and *Slc3a2* than $KPV^{+/+}$ cells yet produce similar levels of SLC7A11 protein (**Figure 2.10A-B**). We hypothesized that upregulation of this transporter might lead to higher levels of glutathione in $KPV^{-/-}$ cells. Indeed, we identified genes involved in glutathione production, including *Slc1a5,* a glutamine transporter; *Glul,* the enzyme involved in the conversion of glutamine to glutamate; *Shmt1,* an enzyme required for the metabolism of serine to glycine; and *Gclm* and *Gclc,* enzymes involved in the conversion of glutamate to glutathione (**Figure 2.10A)**. Accordingly, $KPV^{-/-}$ cells had much higher levels of glutathione and other metabolites involved in its production than $KPV^{+/+}$ cells (**Figure 2.10C-E**). To test whether $KPV^{-/-}$ cells rely on glutathione for survival, we treated the cells with BSO, a well-characterized glutathione-depleting agent (115). As expected, BSO treatment significantly reduced the glutathione levels compared to cells at baseline and abrogated the difference between $KPV^{+/+}$ and $KPV^{-/-}$ cells (**Figure 2.10E**). Interestingly, BSO treatment caused elevated cell death in $KPV^{-/-}$ cells compared to $KPV^{+/+}$ cells, suggesting that $KPV^{-/-}$ cells are more reliant on glutathione for survival than $KPV^{+/+}$ cells (**Figure 2.11A**).

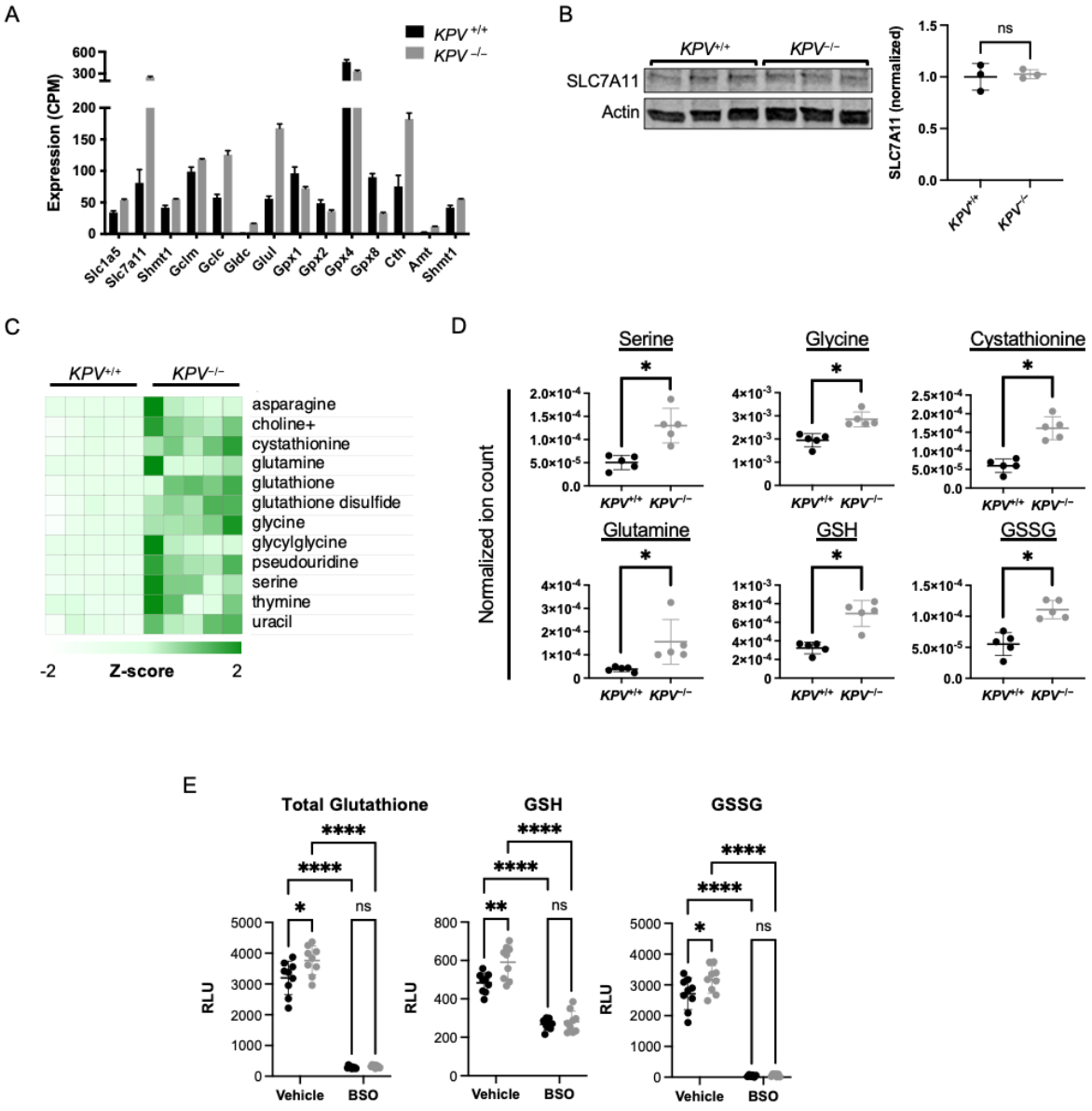

Figure 2.10. *KPV*$^{-/-}$ cells accumulate glutathione. (**A**) Select gene expression values from RNA sequencing. All gene comparisons shown (*KPV*$^{+/+}$ vs. *KPV*$^{-/-}$) have FDR<0.05 after adjusting for multiple comparisons; therefore, all gene differences shown between *KPV*$^{+/+}$ vs. *KPV*$^{-/-}$ cells are statistically significant. (**B**) SLC7A11 levels were measured by Western blot and normalized to an actin loading control and the average *KPV*$^{+/+}$ control. (**C-D**) Differentially produced metabolites are plotted with each row representing z-scores for each metabolite. Metabolite data was log-transformed and then subjected to an unpaired two-tailed t-test; p-values were corrected for multiple comparisons. Heatmap of normalized values (z-scores) of all metabolites that are significantly different (**C**) and plots of ion count normalized to total ion count (**D**) are shown (all comparisons shown have adjusted p-value<0.05). (**E**) Total glutathione and GSSG were quantified in *KPV*$^{+/+}$ and *KPV*$^{-/-}$ cells treated with a vehicle control or BSO for 24 hours using a luminescence-based assay (RLU = relative light units). GSH levels were calculated by subtracting GSSG from total glutathione. Groups were compared using a 2-way ANOVA with multiple comparisons. All data are presented as the mean ± standard deviation. (*p<0.05; **p<0.01; ****p<0.0001).

The accumulation of lipid peroxides triggers ferroptosis. Long-chain fatty acid–CoA ligase 4 (ACSL4) promotes the incorporation of polyunsaturated fatty acids (PUFAs) into phospholipids (PUFA-PLs), which are oxidized into PL-PUFA-OOHs (116, 117). *Acsl4* is upregulated in $KPV^{-/-}$ cells compared to $KPV^{+/+}$ cells, suggesting that there may be an elevation of lipid peroxides in $KPV^{-/-}$ cells (**Figure 2.11B**). Using BODIPY-C11, we found that lipid peroxidation was significantly higher in $KPV^{-/-}$ cells than $KPV^{+/+}$ cells under oxidative stress (**Figure 2.11C**). To test whether BSO-mediated cell death in $KPV^{-/-}$ cells occurred via ferroptosis, cells were treated with ferrostatin-1 (Fer-1), a drug that blocks lipid peroxidation. Ferrostatin-1 attenuated oxidized lipid levels and reduced the BSO-induced $KPV^{-/-}$ cell death (**Figure 2.11A and C**). In agreement with these findings, the ferroptosis biomarker *Ptgs2* is upregulated in $KPV^{-/-}$ cells (**Figure 2.11D**) (118). Together, these results indicate that $KPV^{-/-}$ cells are subject to increased lipid peroxidation and ferroptosis under oxidative stress compared to $KPV^{+/+}$ cells.

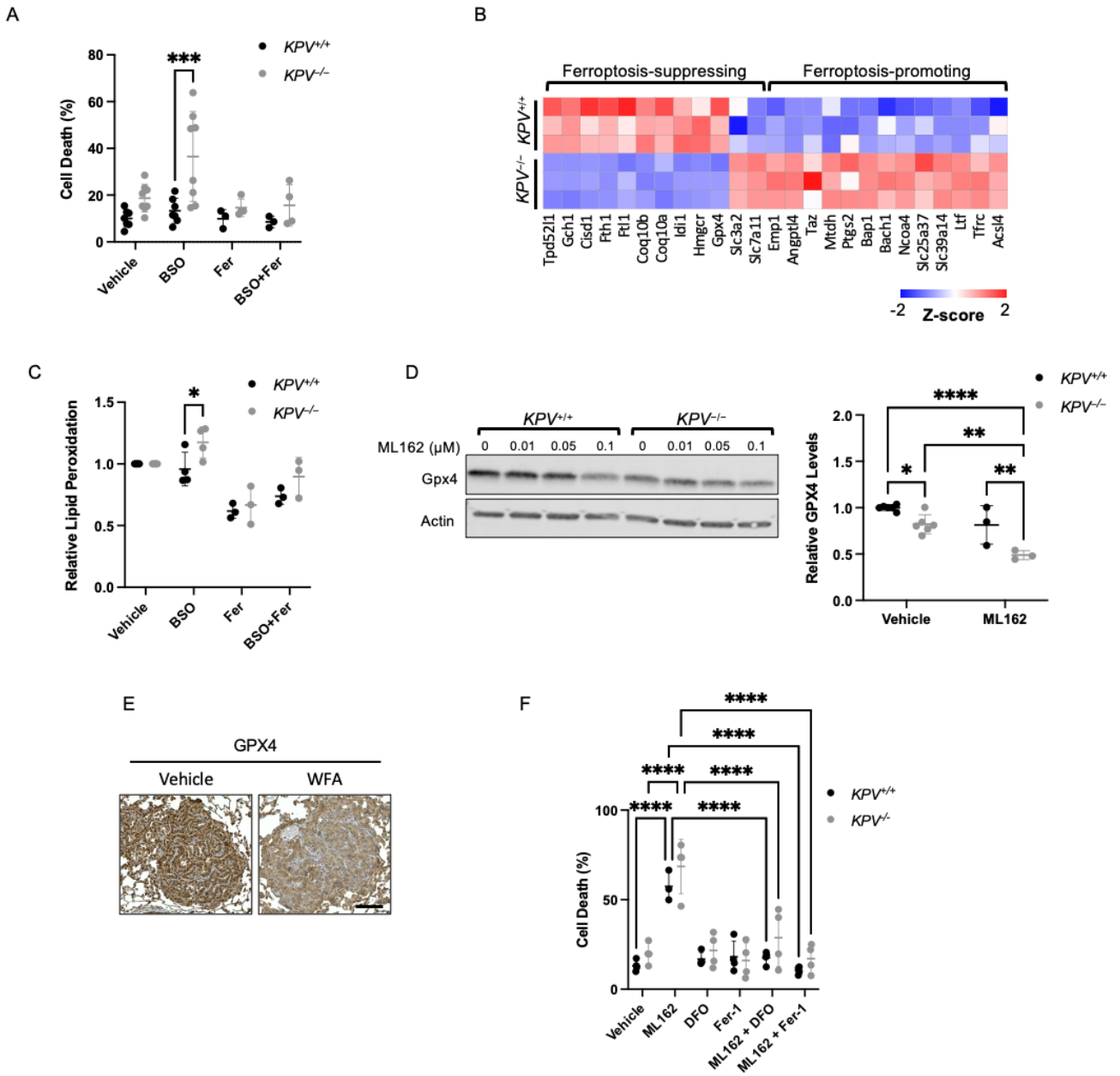

Figure 2.11. *KPV*$^{-/-}$ cells are susceptible to ferroptosis. (**A**) Cells were treated with indicated reagents for 48 hours. Cell death was measured through flow cytometry (n=6-8). (**B**) Z-scores representing gene expression data from RNA-sequencing. All gene comparisons shown (*KPV*$^{+/+}$ vs. *KPV*$^{-/-}$) have FDR<0.05 after adjusting for multiple comparisons; therefore, all gene differences shown between *KPV*$^{+/+}$ vs. *KPV*$^{-/-}$ cells are statistically significant. (**C**) BODIPY was measured by flow cytometry and normalized to the average vehicle values per experiment (n=6-8). (**D**) GPX4 levels were measured by Western blot and normalized to an actin loading control and the *KPV*$^{+/+}$ vehicle control. Quantification is from cells treated with 0.1 μM ML162; data was collected from three independent blots (n=3-6). (**E**) Lungs were harvested from *KPV*$^{+/+}$ mice treated with WFA or vehicle control at 6 weeks after adenoviral Cre infection, fixed, sectioned, and subjected to anti-GPX antibody staining. Scale bar: 1 mm. (**F**) *KPV*$^{+/+}$ and *KPV*$^{-/-}$ cells were treated with the ML162 (1 μM), DFO (100 μM), and/or Fer-1 (10 μM) for 48 hours; cell death was quantified with an LDH assay. Groups were compared using a 2-way ANOVA with multiple comparisons. All data are presented as the mean ± standard deviation. (****p<0.0001). In **A**, **C**, **D**, and **F** groups were compared using a 2-way ANOVA with multiple comparisons. All data are presented as the mean ± standard deviation. (*p<0.05; **p<0.01; ***p<0.001; ****p<0.0001).

Ferroptosis is regulated by extrinsic factors and intrinsic factors. The primary extrinsic factors include the cystine-glutathione axis and iron transport. Because of the seemingly contradictory evidence of increased ferroptosis despite higher levels of the protective antioxidant glutathione in *KPV*$^{-/-}$ cells, we explored other pathways of ferroptosis regulation, including intrinsic factors, namely the antioxidant molecule GPX4 and the extrinsic pathway of iron transport. Recently, WFA, which disrupts the vimentin intermediate filament network (**Figure 2.8A-B**), was shown to induce lipid peroxidation and ferroptosis in a murine model of neuroblastoma via an interaction with GPX4 (119). GPX4, a key upstream regulator of ferroptosis, is responsible for both converting GSH to glutathione disulfide (GSSG) and reducing phospholipid hydroperoxides (PL-OOHs) to their corresponding alcohol (PL-OHs), thereby preventing the accumulation of lipid peroxides and leading to suppression of ferroptosis. We found that *KPV*$^{-/-}$ cells had reduced *Gpx4* gene expression compared to *KPV*$^{+/+}$ cells (458.0 ± 31.0 versus 334.2 ± 12.7 CPM, respectively) (**Figure 2.11B)**. GPX4 is a selenoperoxidase; its biosynthesis is regulated through the mevalonate pathway (120). *Hmgcr* and *Idi1* are key components of the mevalonate pathway, giving rise to *Coq10a* and *Coq10b*; these genes are expressed at lower levels in *KPV*$^{-/-}$ cells compared to *KPV*$^{+/+}$ cells (**Figure 2.11B**). GPX4 protein expression, assessed by Western blot on isolated tumor cells and IHC of tumors, was significantly lower in *KPV*$^{-/-}$ cells than in *KPV*$^{+/+}$ cells and in tumors from WFA-treated *KPV*$^{+/+}$ mice compared to vehicle control (**Figure 2.11D-E**). Treatment with ML162, a drug that directly targets GPX4, leads to greater loss of GPX4 in *KPV*$^{-/-}$ cells compared to *KPV*$^{+/+}$ cells (**Figure 2.11D**). The ML162-mediated decrease of GPX4 protein expression in *KPV*$^{-/-}$ and *KPV*$^{+/+}$ cells was associated with increased cell death, which was prevented by treatment with Fer-1 (**Figure 2.11F**). Interestingly, genes that promote iron metabolism like *Tfrc, Ltf, Slc39a14*, *Slc25a37*, *Ncoa4*, and *Bach1* were upregulated in *KPV*$^{-/-}$ cells, while genes that decrease the cytosolic labile iron pool, like *Ftl*, *Fth1*, and *Cisd1* were downregulated (121-124) (**Figure 2.11B,**

2.11F). In agreement with the hypothesis that iron transport also mediates ferroptosis in our system, ML162-induced cell death was rescued by the iron chelator desferoxamine (DFO) (**Figure 2.11F**). Together, these results show that several ferroptosis-associated pathways, including loss of intrinsic antioxidant molecules and upregulation of iron transport factors, are working in tandem to induce cell death in *KPV*$^{-/-}$ cells (**Figure 2.12**). Therefore, we conclude that vimentin confers protection against ferroptosis.

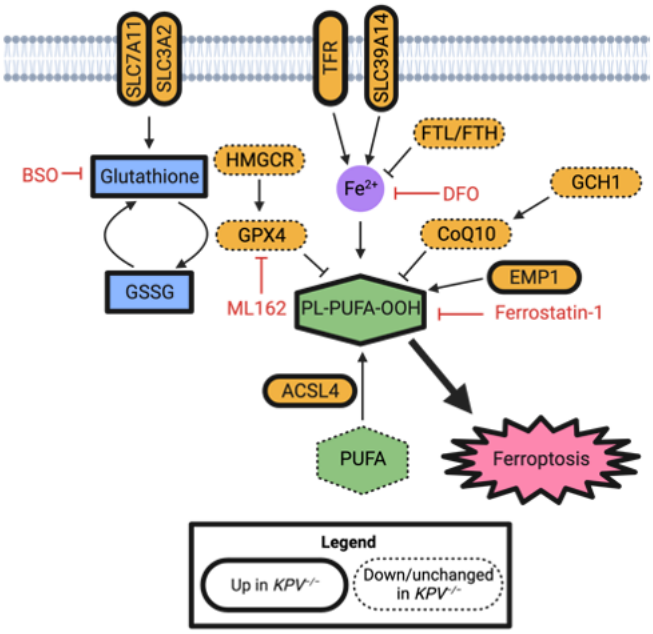

Figure 2.12. Vimentin confers protections from ferroptosis. A schematic model representing the ferroptosis-related mechanisms that are affected by loss of vimentin in KRAS-mutant, p53-null lung adenocarcinoma cells. Created with BioRender.com.

2.2.7 Vimentin is required for lung cancer metastasis

We set out to determine if vimentin is required for *in vivo* metastasis. The cell-autonomous ability of vimentin-expressing cells to metastasize was assessed using an allograft tumor model. *Luc-KPV*$^{+/+}$ cells, a luciferase (*Luc)* expressing cell line that reproducibly colonizes to the lung following subcutaneous injection (125, 126), were transfected with CRISPR/Cas9 vimentin knockout plasmid to generate *Luc-KPV*$^{-/-}$ cells (**Figure 2.13A**). To determine whether an intact vimentin network is

required for metastasis, we also generated *Luc-KPV*^{Y117L} cells, which express a mutant form of vimentin that cannot form full-length vimentin and instead form punctate unit-length filaments (8) (**Figure 2.13B**). Briefly, nude mice were subcutaneously injected in the right flank with either *Luc-KPV*$^{+/+}$, *Luc-KPV*$^{-/-}$, or *Luc-KPV*^{Y117L} cells (**Figure 2.13A-B**). Lung radiance, flank tumor radiance, and flank tumor volume was measured weekly (**Figure 2.13B-G**). At week 4 after injection, mice injected with *Luc-KPV*$^{+/+}$ cells had considerably lung tumor burdens, as assessed by IVIS imaging and H&E staining (**Figure 2.13B-E**). In contrast, *Luc-KPV*$^{-/-}$ and *Luc-KPV*^{Y117L} cells failed to form lung tumors. When quantified, the metastatic signal in the lung was significantly higher in *Luc-KPV*$^{+/+}$ mice (15.3E8±18.1E8 photons•cm^{-2}sr^{-1}sec^{-1}) than *Luc-KPV*$^{-/-}$ mice (0.564E7±0.754E8 photons•cm^{-2}sr^{-1}sec^{-1}) or *Luc-KPV*^{Y117L} mice (2.63E8±3.78E8 photons•cm^{-2}sr^{-1}sec^{-1}) (**Figure 2.13E**). The lungs of *KPV*$^{+/+}$-injected mice displayed large, vimentin-positive metastatic lesions (**Figure 2.13D**). Conversely, the few metastatic tumors that formed in the lungs with *KPV*$^{-/-}$ cells were sparse and small; as expected, these tumors did not express vimentin.

While there was no significant difference in flank tumor size between *Luc-KPV*$^{+/+}$, *Luc-KPV*$^{-/-}$, or *Luc-KPV*^{Y117L} conditions at week 1, by week 2 *Luc-KPV*$^{+/+}$ flank tumor radiance was higher (23.9E8±12.1E8 versus 9.10E8±4.62E8 and 8.48E8±3.97E8 photons•cm^{-2}sr^{-1}sec^{-1}, respectively), suggesting that *Luc-KPV*$^{+/+}$ tumors grow faster than *Luc-KPV*$^{-/-}$ and *Luc-KPV*^{Y117L} *in vivo* (**Figure 2.13E-F**). To remove the effects on metastasis due to differences in proliferation, flank tumors were excised at week 3. The mass of excised *Luc-KPV*$^{+/+}$ (0.859±0.344 grams) flank tumors was greater than *Luc-KPV*$^{-/-}$ (0.545±0.170 grams) and *Luc-KPV*^{Y117L} (0.611±0.212 grams) tumors (**Figure 2.13G**). Excised tumors were stained with H&E and immunostained for vimentin (**Figure 2.13D**). *Luc-KPV*$^{+/+}$ cells formed dense tumors that displayed uniform vimentin expression. *Luc-KPV*$^{-/-}$ and *Luc-KPV*^{Y117L} cells also formed dense tumors; surprisingly, some cells within the tumor expressed vimentin. Based on their spindly or round shapes, we inferred that these cells were infiltrating fibroblasts or

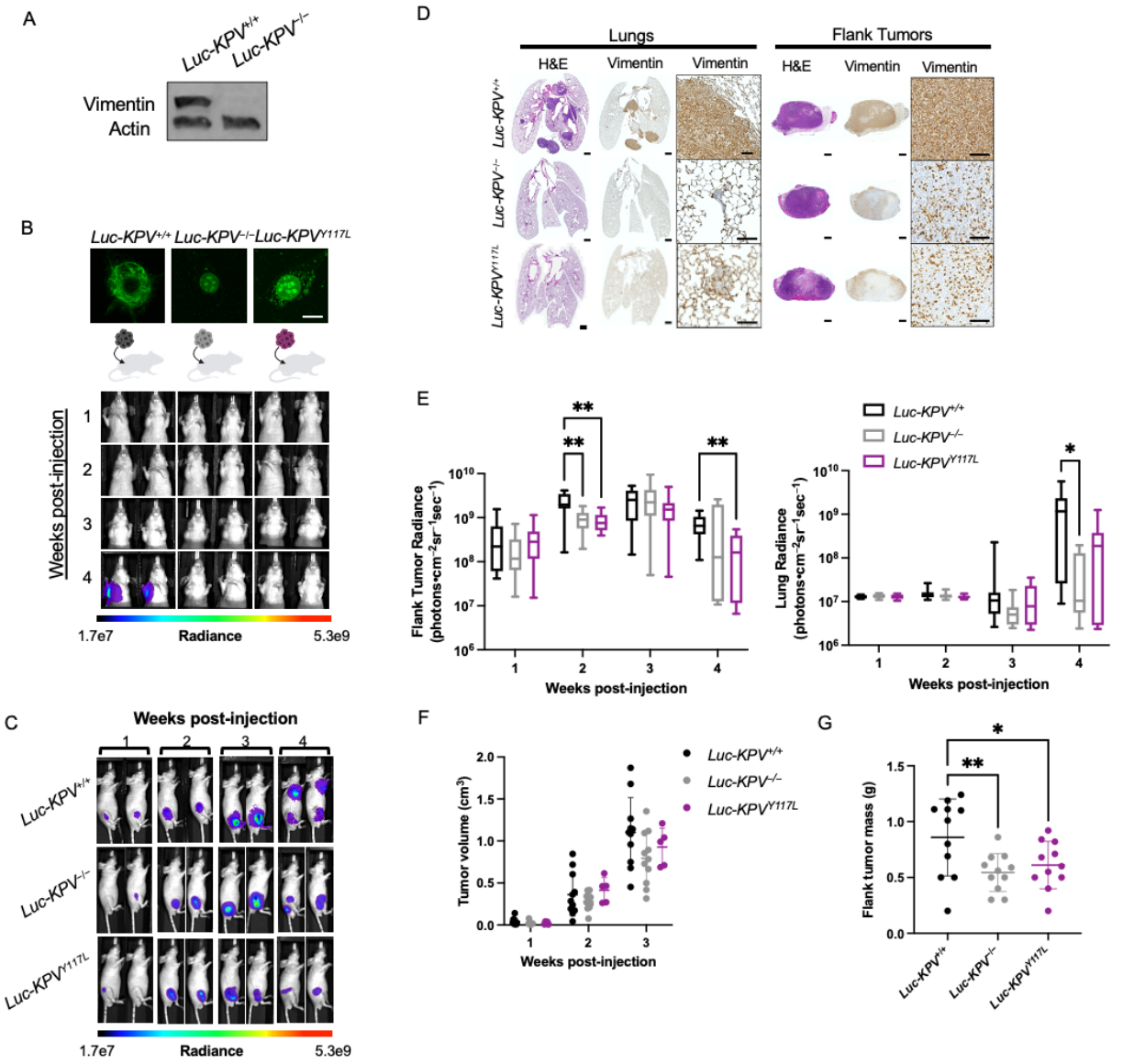

Figure 2.13. Vimentin is required for accelerated lung cancer metastasis. (**A**) Luciferase-tagged $KPV^{+/+}$ (*Luc-*$KPV^{+/+}$) cells were treated with CRISPR-Cas9 to knock out vimentin (*Luc-*$KPV^{-/-}$). Cells were subjected to a Western blot and probed for vimentin and actin. (**B-C**) (*Top*) *Luc-*$KPV^{-/-}$ cells were transfected with vimentin-Y117L to create *Luc-*KPV^{Y117L} cells. Cells were stained with DAPI and an anti-vimentin antibody (*green*). Scale: 10 µm. (*Bottom*) A total of 1×10^6 $KPV^{+/+}$, $KPV^{-/-}$, or KPV^{Y117L} cells labeled with luciferase (*Luc-*$KPV^{+/+}$, *Luc-*$KPV^{-/-}$, and *Luc-*KPV^{Y117L} respectively) were injected subcutaneously into the right flank of nude mice. At 3 weeks post-injection, primary tumors were removed and lung metastases were tracked for an additional 1 week. Shown are representative IVIS images of mice (n=9-11 per group). Shown are the coronal views (**B**), which were acquired after masking the flank tumor to minimize bleed-through of the signal, and the full-animal view (**C**). Intensity overlay shows the accumulation of luciferase-labeled cells. (**D**) Lungs at week 4 and excised flank tumors from week 3 were fixed, sectioned, and subjected to H&E staining and vimentin immunohistochemical staining. Positive vimentin staining is brown, and nuclei are blue. Scale bars: 1 mm (whole tumor/lung, *left*), 100 µm (inset, *right*). (**E**) Luciferin signal was quantified from primary flank tumors and the lungs. (**F**) Flank tumor volume was measured with calipers each week. Volume was calculated using the formula Volume=(length^2 x width)/2. For **E-F**, data were subjected to a two-way ANOVA with multiple comparisons. (**G**) At week 3, tumors were removed and weighed. For **G**, data were subjected to a one-way ANOVA with multiple comparisons. (*p<0.05; **p<0.01). Data are presented as the mean ± standard deviation.

macrophages, two cell types that canonically express vimentin. Together, we conclude that vimentin

is required for the metastatic spread of murine NSCLC cells. Furthermore, vimentin unit-length filaments are not sufficient to rescue metastasis. Therefore, an intact, mature vimentin intermediate filament network is required for NSCLC metastasis.

2.3 Discussion

Clinically, vimentin expression correlates with increased metastatic potential (95) (**Figure 2.3**), high nuclear grade (127), and poor overall survival across most solid tumor types, including lung, prostate, and breast cancers (81-83). Vimentin has also been implicated in many aspects of cancer initiation and progression, including tumorigenesis, EMT, and the metastatic spread of cancer (84). These reports often relied on *in vitro* experiments comparing cancer cell lines and suppressing vimentin expression with siRNA, shRNA, and pharmacologic agents or with cells derived from *Vim*$^{-/-}$ mice but lacking oncogene expression. Our data provide causal evidence that vimentin is required for the metastasis of *Kras*-mutant, *Tp53*-null lung cancer cells *in vivo and in vitro*. Data from the *KPV*$^{-/-}$ GEMM show that vimentin is required for metastasis and tumor progression (**Figures 2.2 and 2.13**), as *KPV*$^{-/-}$ mice had decreased lung tumor burden (**Figure 2.2C-D**), lower-grade tumors (**Figure 2.2G)**, and no metastasis from primary tumors in the flank to the lung (**Figure 2.13B-E**). Consistent with the decreased metastatic rates, we observed a survival advantage in the *KPV*$^{-/-}$ mice (**Figure 2.2B**). These results were recapitulated in *KPV*$^{+/+}$ mice by disrupting vimentin filaments with WFA treatment two weeks post-tumor initiation (**Figure 2.9**). Collectively, these data provide evidence that vimentin is integral in the progression and metastasis of lung cancer.

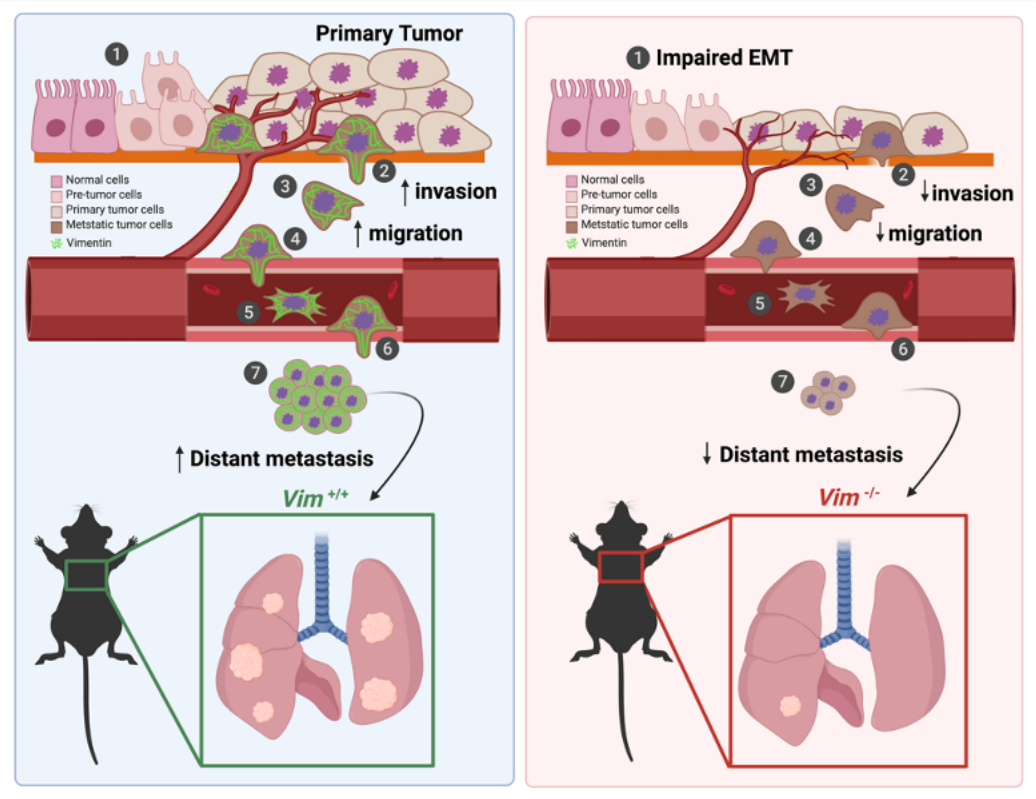

Figure 2.14. Vimentin is required for many of the initiating events associated with lung cancer metastasis.

EMT is the canonical mechanism by which cancer cells lose their epithelial morphology, form invadopodia and degrade the surrounding basement membrane to promote the invasive spread of cancer (84, 89). Vimentin expression is upregulated in epithelial cells undergoing EMT in malignant tumors, and several studies support the notion that vimentin functions as a positive regulator of EMT (46, 55, 84, 86, 128). In this respect, it has been proposed that vimentin intermediate filaments provide a scaffold for the recruitment of transcription factors, such as Twist1 and Slug (86). Specifically, Twist1 upregulates Cullin2 circular RNA, which absorbs vimentin-targeting miRNAs, and thus increases vimentin expression (88). Accordingly, we found that *KPV*$^{-/-}$ cells lack expression of *Twist1* (**Figure 2.5C**). Similarly, when Transforming Growth Factor (TGF)-β is used to activate Smad-mediated EMT in primary alveolar epithelial cells, cells undergo a rapid induction of vimentin expression regulated by a Smad-binding-element located in the 5' promotor region of the *Vim* gene (54). Presently, we used

RNA-seq to show that *KPV*$^{-/-}$ cells derived from primary lung tumors display a distinct transcriptional phenotype, which is characterized by the suppression of genes directly involved in EMT (**Figure 2.5**). Collectively, these data suggest that vimentin should no longer be considered a biomarker of EMT but rather a required protein for transcriptional activation and interaction with transcription factors such Twist and Slug, which serve to induce EMT in epithelial cells.

After a tumor cell has undergone EMT, it will invade the surrounding tissue. We previously reported that the transient expression of vimentin in epithelial cells, which typically express type I and type II keratin intermediate filaments, causes epithelial cells to be transformed into mesenchymal cells, which is accompanied by changes in cell shape, increased cell motility, and focal adhesion dynamics (54, 77). Using four different methods, we show that vimentin is required for cancer cell invasion across the basement membrane and through the interstitial matrix. Direct evidence supporting the role of vimentin in the migration of *Kras*-mutant, *Tp53*-null lung cancer cells was demonstrated by disrupting vimentin expression genetically (**Figure 2.7A)** and pharmacologically in mouse (**Figure 2.8D**) and human-derived (**Figure 2.8F**) cancer cells resulting in impaired migration. Furthermore, loss of vimentin through genetic manipulation (**Figure 2.7B**) and pharmacological interference with WFA (**Figure 2.8E**) confers an inability of cells to invade a layer of the basement membrane. *KPV*$^{-/-}$ cells also fail to invade through a collagen-rich matrix in a 3-dimensional experimental model (**Figure 2.8C**). Importantly, we provide evidence that vimentin is required for *in vivo* metastasis. In the *KPV*$^{+/+}$ mice, we observed metastases in the liver at 12 weeks post-tumor induction; *KPV*$^{-/-}$ mice had no evidence of metastatic lesions (**Figure 2.1D**). To confirm this observation, we implanted cells in the flanks of mice. *KPV*$^{+/+}$ cells, but not *KPV*$^{-/-}$ cells nor *KPV*^{Y117L} cells, were able to invade and migrate away from the primary tumor and seed metastatic lesions in the lung (**Figure 2.13**). Together, these results provide direct evidence that an intact vimentin intermediate filament network is required for the cell motility that leads to metastasis.

To our knowledge, this is the first report to show that vimentin protects cancer cells from ferroptosis (**Figure 2.11**). Specifically, we show that *KPV*$^{-/-}$ cells are more susceptible to BSO-induced death than *KPV*$^{+/+}$ cells, and that this effect can be rescued with Fer-1. Importantly, we show that several convergent mechanisms of ferroptosis are activated in *KPV*$^{-/-}$, but not *KPV*$^{+/+}$, cells (**Figure 2.11F**). These include loss of the intrinsic mechanism of GPX4-mediated protection from lipid peroxidation and elevation of the extrinsic mechanism of iron transport. Interestingly, previous studies support our findings that suggest vimentin may interact with GPX4, be involved in iron metabolism, and play a role in lipid droplet (LD) maintenance. A report from Hassannia et al. recently showed that WFA treatment, which directly targets vimentin, also binds and inactivates GPX4, thus inducing ferroptosis (119). In line with this finding, we show that GPX4 levels are lower *KPV*$^{-/-}$ cells compared to *KPV*$^{+/+}$ cells (**Figure 2.11B**, **2.11D**). Additionally, suppressors of the redox pathway upstream of GPX4 (glutathione, SLC7A11) are increased or unchanged in *KPV*$^{-/-}$ cells (**Figure 2.10**). In contrast, downstream readouts like lipid peroxidation and cell death are decreased (**Figure 2.11A-C**), suggesting that there may be a direct relationship between GPX4 and vimentin. Several iron-related genes, including the transferrin receptor (*Trfc*), *Ltf*, *Slc39a14*, *Slc25a37*, *Ncoa4*, and *Bach1* are upregulated in *KPV*$^{-/-}$ cells (**Figure 2.11B**). In contrast, genes associated with negative regulation of the cytosolic iron pool, like *Ftl*, *Fth1*, and *Cisd1* are downregulated in *KPV*$^{-/-}$ cells. Additionally, treating cells with the iron-chelator DFO is sufficient to rescue ML162-induced cell death (**Figure 2.11F**). In line with our findings, vimentin-knockdown regulatory T cells (T-regs) express higher levels of the transferrin receptor and take up more fatty acids than wildtype T-regs (65). However, the precise role of vimentin in iron metabolism remains to be explored. Degradation of LDs promotes ferroptosis (129). Interestingly, vimentin forms a cage around LDs and physically anchors LDs via the linker protein perilipin (14). Vimentin-null cells have smaller LDs, impaired lipid motility, and impaired lipolysis (16, 17). In support of the hypothesis that differences in

lipolysis might lead to susceptibility to ferroptosis in *KPV*$^{-/-}$ cells, we observed that *Gch1*, which is the rate-limiting enzyme of BH_4-mediated lipid remodeling, and *Tpd52l1*, which promotes lipid storage, are upregulated in *KPV*$^{+/+}$ cells compared to *KPV*$^{-/-}$ cells (129, 130) (**Figure 2.11B**). These data suggest that the interaction between vimentin and lipid droplets may mediate ferroptosis. Of note, many of the studies mentioned in this section were conducted in non-cancer cell types, and the precise role of vimentin in regulating ferroptosis in KRAS-mutant cancer remains to be identified.

In the *Kras*-mutant, *Tp53*-null model of lung cancer, global vimentin depletion confers a survival advantage. Additionally, by treating *KPV*$^{+/+}$ mice with WFA following tumor development, we show that the delayed tumor growth and metastasis observed when vimentin is suppressed is not due solely to delayed onset of tumor growth, but rather to attenuated growth kinetics in tumor cells that lack an intact vimentin network. Although vimentin-null mice were first reported to display no obvious phenotype, these data along with previous report suggest that loss of vimentin is protective against a range of disease states including lung cancer, acute lung injury, acute respiratory distress syndrome, idiopathic pulmonary fibrosis, bacterial meningitis, cerebral ischemia, and acute colitis (12, 51, 66, 131-133). These global vimentin knockout mice lack vimentin expression in tumor cells and lack vimentin in the tumor microenvironment (TME). The TME, which includes immune and stromal cells, can promote metastasis of primary tumor cells. The cytokine interleukin 1b (IL-1b), produced by macrophages in the lung, is a mediator of cancer growth, metastasis, and tumor-associated macrophage infiltration (51, 134). Our group has reported that vimentin is required for mature IL-1b release (51). Because of the potential contribution of the TME in vimentin-null mice, we set out to ensure that vimentin is sufficient in cancer cells to promote metastasis. We injected *KPV*$^{+/+}$ or *KPV*$^{-/-}$ cells into wildtype nude mice; these mice lack T cells but retain innate immune cells. We observed recruited mesenchymal and immune cells in subcutaneous flank tumors (**Figure 2.13D**), suggesting that the vimentin-positive TME in this model participates in growth of the primary tumor. Despite

being in the presence of vimentin-expressing stromal and immune cells, *KPV*$^{-/-}$ cells failed to metastasize. Therefore, while other groups have found that vimentin deficiency impairs function in cancer-associated fibroblasts and immune cells such as macrophages and T cells (46, 51, 65, 135), a vimentin-expressing microenvironment is not sufficient to promote metastasis in the time frame evaluated. To better understand how vimentin participates in different compartments of the TME, we recognize that animal models with immune-, mesenchymal-, and epithelial-specific deletion of vimentin will need to be created.

This study fills a major gap in the literature by providing novel causal data that vimentin is required for the *in vivo* progression of NSCLC at several steps of the metastatic cascade. Importantly, our *in vivo* data validated both our *in vitro* data and *in vitro* data from previously published reports (10, 49, 56, 89, 136, 137). Additionally, this work gives causal context to clinical data associating vimentin expression with tumor progression in patients (81, 95, 138). By using *in vivo* models and disrupting vimentin both genetically and pharmacologically, we have presented physiological context to these reports. We have identified vimentin as a new clinical target for metastatic lung cancer through this study.

2.4 Materials and Methods

2.4.1 Murine lung cancer model

All animal experiments were approved by Northwestern University's Institutional Animal Care and Use Committee (IACUC). Sex-matched 6–10-week-old mice were used for all *in vivo* experiments. *LSL-Kras*$^{G12D/+}$;*Tp53*$^{flox/flox}$ (*KPV*$^{+/+}$) mice were bred as described by DuPage and colleagues and were generously gifted to us by Dr. Navdeep Chandel (Northwestern University, Chicago, IL) (101). Vimentin-knockout mice were a gift from Albee Messing (University of Wisconsin, Madison, WI). Vimentin-knockout mice were crossed with *KPV*$^{+/+}$ mice to create *KPV*$^{-/-}$ mice. *KPV*$^{+/+}$, *KPV*$^{-/-}$, and the validated *Rosa26-LSL-LacZ* mice were administered adenovirus expressing Cre recombinase

(Ad-Cre; ViraQuest) or a null adenovirus (Ad-Null) via intratracheal instillation (1×10^9 pfu unless otherwise noted) under isoflurane anesthesia (107). Survival was monitored daily. Weight was monitored weekly.

2.4.2 Magnetic resonance imaging

Scheduled magnetic resonance imaging (MRI) was performed at Northwestern University Center for Translational Imaging (Chicago, IL) via a 7-tesla system (Clinscan, Bruker) using a four-channel mouse body coil at set time points (2, 6, and 10 weeks after Ad-Cre administration). Mice were anesthetized with isoflurane (2% isoflurane in oxygen for induction, followed by 1.5–2% via nose cone for maintenance during imaging) to permit tolerance to imaging. Pulse oximetry and respiration were recorded and used to trigger the MRI to avoid motion artifacts. Turbo Multi Spin Echo imaging sequence was used in conjunction with respiratory triggering to acquire *in vivo* MRI coronal images covering all the lung area and portions of abdomen, including liver and kidneys (ST = 0.5 mm, In plane = 120 μm, TR =1000 msec, TE= 20 msec). Gradient Echo sequence was used with cardiac triggering (using pulse oximeter rate) covering the lung area transversally (ST = 0.5 mm, In plane = 120 μm, TR ~20 msec, TE ~ 2 msec). Jim software was used to quantify tumor burden (Xinapse).

2.4.3 Immunohistochemistry

Mice were anesthetized and lungs were perfused via the right ventricle with 4% paraformaldehyde in phosphate-buffered saline (PBS). A 20-gauge angiocatheter was sutured into the trachea, heart and lungs were removed en bloc, and then lungs were inflated with 0.8 mL of 4% paraformaldehyde at a pressure not exceeding 16 cm H_2O. Tissue was fixed in 4% paraformaldehyde in PBS overnight at 4°C, then processed, embedded in paraffin, and sectioned (4–5 μm). Tissue sections were stained with hematoxylin and eosin (H&E) or used for immunohistochemistry. After rehydration, tissues were subjected to antigen retrieval in 10 mM sodium citrate (pH = 6.0) with 0.05% Tween-20 for 20 minutes at 96–98°C, followed by 20 minutes of cooling. Tissue sections were blocked in 3% hydrogen peroxide for 5 min, then a Vector Laboratories avidin/biotin blocking kit (SP-2001), Vectastain ABC kit (PK-

4001), and 3,3'-diaminobenzidine (DAB) peroxidase substrate kit (SK-4100) were used according to the manufacturer's protocols. Nuclei were counterstained with hematoxylin (Thermo Scientific 72604) and treated with bluing solution (Thermo Scientific 7301), and then coverslips were mounted with Cytoseal 60 (Thermo Scientific 8310-4). A TissueGnostics automated slide imaging system was used to acquire whole-tissue images and measure area. Human tissue was purchased in microarray format from Biomax (LC2083) and stained as described above.

2.4.4 Cell isolation and culture

KPV$^{+/+}$ and *KPV*$^{-/-}$ mice were treated with Ad-Cre as described above; after 6 weeks, mice were sacrificed and lung tumors were excised. Tissue was dissociated into a single cell suspension in 0.2 mg/mL DNase and 2 mg/mL collagenase D and was filtered through a 40 μm filter. Cells then underwent two rounds of selection. First, cells were treated with anti-CD45 magnetic beads (Miltenyi Biotec, 130-052-301) and were passed through a magnetic column. CD45-negative cells were then subjected to anti-EPCAM magnetic beads (Miltenyi Biotec, 130-105-958) and underwent positive selection. CD45-negative, EPCAM-positive cells were expanded *in vitro* and were used in experiments between passages 1 and 10. Cells derived from a human lung adenocarcinoma (A549) were obtained from the American Type Culture Collection (ATCC, Manassas, VA). All cells were maintained in Dulbecco's modified Eagle medium (DMEM) supplemented with 10% fetal bovine serum, 100 U/mL penicillin, 100 μg/mL streptomycin, and HEPES buffer. All cells were grown in a humidified incubator of 5% CO_2/95% air at 37°C.

2.4.5 Polymerase chain reaction

Mice were infected with Ad-Null or Ad-Cre; at 2, 8, and 12 w.p.i., mice were sacrificed and lungs were harvested. Lungs were lysed, and DNA was extracted and amplified by polymerase chain reaction (PCR) using the following primers: *Kras* forward, GGC CTG CTG AAA ATG ACT GAG TAT A; *Kras* reverse, CTG TAT CGT CAA GGC GCT CTT; *Kras-G12D* forward,

CTTGTGGTGGTTGGAGCTGA; and *Kras-G12D* reverse, TCCAAGAGACAGGTTTCTCCA. DNA products were run on an agarose gel and imaged with the Li-Cor Odyssey imaging system.

2.4.6 Western blotting

Western blot analysis was utilized to quantify protein levels in cell lysates. The protein was separated using 12% sodium dodecyl sulfate polyacrylamide gel electrophoresis (SDS-PAGE) and transferred onto nitrocellulose membranes. Membranes were then blocked with Odyssey blocking buffer (Li-Cor Biosciences) and subsequently incubated with the appropriate primary antibodies overnight at 4°C. IRDye secondary antibodies were then used (Li-Cor Biosciences, 1:10,000) for 2 hours at room temperature. Images of blots were acquired using the Li-Cor Odyssey Fc Imaging System.

2.4.7 RNA-sequencing

Tumor cells were isolated from *KPV*$^{+/+}$ and *KPV*$^{-/-}$ mice at 6 w.p.i. and underwent CD45-negative, EpCAM-positive magnetic-activated cell sorting (MACS) selection as described above. Cells were cultured for one passage, then lysed using RLT lysis buffer (Qiagen), and total RNA was isolated with the RNeasy Plus Mini Kit (Qiagen). Quality of RNA was confirmed with a TapeStation 4200 (Agilent); all samples had an RNA integrity number (RIN) score equal to or greater than 9.8. Next, mRNA was isolated via poly(A) enrichment (NEBNext). Libraries were prepared using NEBNext RNA Ultra chemistry (New England Biolabs). Sequencing was performed on an Illumina NextSeq 500 using a 75-cycle single-end high-output sequencing kit. Reads were demultiplexed (bcl2fastq), and fastq files were aligned to the mm10 mouse reference genome with TopHat2. Htseq was used to obtain counts. The resulting data were filtered, and differentially expressed genes (DEGs) were identified using the edgeR package. DEGs were selected using a false discovery rate (FDR) cutoff of <0.05, with a 1.0-fold change cutoff for pairwise comparison. K-means clustering and heat map visualization was performed using the Morpheus web tool (https://software.broadinstitute.org/morpheus). Enrichment analysis was performed using Gorilla (139, 140).

2.4.8 Withaferin A treatments

Withaferin A (WFA) was purchased from Enzo Life Sciences and dissolved in dimethyl sulfoxide (DMSO; Sigma-Aldrich) to a final concentration of 5 mM unless noted otherwise. For *in vivo* experiments, jelly pellets were utilized to provide an oral, voluntary method of drug delivery. Using a 24-well flat-bottom tissue culture plate as the jelly mold, WFA (4 mg/kg in DMSO) or vehicle control (DMSO only) were combined with gelatin and Splenda for flavoring as described elsewhere (141). Tumor development was induced with Ad-Cre as described above. Two weeks following Ad-Cre administration, mice were fed jelly pellets every other day for 4 weeks. Survival was tracked daily and weight was measured weekly.

2.4.9 Scratch wound assay

Cells were grown to 100% confluence in 6-well plates. A pipette tip was used to make a single scratch in the monolayer. The cells were washed with 1× PBS to remove debris and imaged at 0 and 6 hours. For WFA conditions, WFA or DMSO was added at 0 hours (when the scratch was created). Rate of cell migration was calculated using ImageJ software. Results were normalized to the initial wound area at 0 hours.

2.4.10 Matrigel invasion assay

Transwell inserts with 8 mm pores were coated with Matrigel (200 mg/mL), and 5×10^4 $KPV^{+/+}$ or $KPV^{-/-}$ cells were seeded atop each transwell in serum-free media. For WFA experiments, cells were resuspended in WFA or DMSO containing media directly before being seeded in transwells. Media containing 10% fetal bovine serum was added to the bottom well to serve as a chemoattractant. Cells were placed at 37°C for 48 hours. Following incubation, the Matrigel with the cells remaining on the upper surface of the transwell was removed with a cotton swab. The cells remaining on the bottom of the membrane were fixed in 2% paraformaldehyde and incubated with Hoechst nuclear dye (Invitrogen; 1:10,000 in 1× PBS). Five random 10× magnification fields were imaged, and the average number of cells per field was quantified; this average is reported as the "invasive index."

2.4.11 Spheroid culture

Spheroids were generated as described by Gilbert-Ross et al. (142). Briefly, cells were grown in Nunclon Sphera 96-well plates (Thermo-Fisher Scientific) at a concentration of 3000 cells per well. After 3 days in culture, cells were transferred using a wide-bore pipette tip to 2 mg/mL collagen (Corning) in 4-well LabTek plates (Nunc). Collagen was allowed to gel at 37°C for 1 hour; then, complete media was added to the spheroids. Gels were imaged using a Ti2 widefield microscope (Nikon) at 0, 24, and 48 hours. Spheroid area was quantified using Fiji software. Reported spheroid area values are normalized to 0-hour spheroid area of the same spheroid.

2.4.12 Metabolomics

KPV$^{+/+}$ and *KPV*$^{-/-}$ cells were grown in 6-well plates. High-performance liquid chromatography (HPLC) grade methanol (80% in water) was added to cells, and plates were incubated at −80°C for 20 minutes. Lysates were collected and centrifuged, and the supernatant was collected and analyzed by High-Performance Liquid Chromatography and High-Resolution Mass Spectrometry and Tandem Mass Spectrometry (HPLC-MS/MS). Specifically, system consisted of a Thermo Q-Exactive in line with an electrospray source and an Ultimate3000 (Thermo) series HPLC consisting of a binary pump, degasser, and auto-sampler outfitted with a Xbridge Amide column (Waters; dimensions of 4.6 mm × 100 mm and a 3.5 μm particle size). The mobile phase A contained 95% (vol/vol) water, 5% (vol/vol) acetonitrile, 20 mM ammonium hydroxide, 20 mM ammonium acetate, pH = 9.0; B was 100% Acetonitrile. The gradient was as following: 0 min, 15% A; 2.5 min, 30% A; 7 min, 43% A; 16 min, 62% A; 16.1-18 min, 75% A; 18-25 min, 15% A with a flow rate of 400 μL/min. The capillary of the ESI source was set to 275 °C, with sheath gas at 45 arbitrary units, auxiliary gas at 5 arbitrary units and the spray voltage at 4.0 kV. In positive/negative polarity switching mode, an m/z scan range from 70 to 850 was chosen and MS1 data was collected at a resolution of 70,000. The automatic gain control (AGC) target was set at 1×10^6 and the maximum injection time was 200 ms. The top 5

precursor ions were subsequently fragmented, in a data-dependent manner, using the higher energy collisional dissociation (HCD) cell set to 30% normalized collision energy in MS2 at a resolution power of 17,500. Besides matching m/z, metabolites are identified by matching retention time with analytical standards and/or MS2 fragmentation pattern. Data acquisition and analysis were carried out by Xcalibur 4.1 software and Tracefinder 4.1 software, respectively (both from Thermo Fisher Scientific). For each sample, peak area of each metabolite was normalized to total ion count per sample. Data were log-transformed and compared with a two-tailed, unpaired t-test. Data was analyzed with MetaboAnalyst software (143).

2.4.13 Preparation of cells for subcutaneous flank injection

KPV$^{+/+}$ cells labeled with luciferase (*Luc-KPV*$^{+/+}$ cells) were a generous gift from Dr. Navdeep Chandel. To create *Luc-KPV*$^{-/-}$ cells, *Luc-KPV*$^{+/+}$ cells were transfected with a commercially available CRISPR/Cas9 vimentin knockout plasmid according to manufacturer's directions (Santa Cruz Biotechnology sc-423676). *Luc-KPV*^{Y117L} cells were created as previously described (8).

2.4.14 Tracking of tumor growth in subcutaneous flank injection model

Male nude (NU/J) mice were purchased from Jackson Laboratories; 8–12-week-old mice were anesthetized with 2% isoflurane in oxygen and were given a subcutaneous injection of cells (1×10^6 cells in 100 μL of 1× PBS) on their right flanks. Weight and tumor volume were monitored weekly. For IVIS imaging, mice were injected with 150 mg of D-luciferin per kilogram of body weight (PerkinElmer 770504). After 10 minutes, IVIS images were captured. At week 3 post-injection, tumors were removed. Briefly, mice were anesthetized with ketamine (100 mg/kg body weight) and xylazine (10 mg/kg body weight). Tumor area was disinfected with 70% ethanol and iodide solution. Tumors were excised and placed in 4% paraformaldehyde for immunohistochemistry. Wounds were closed with simple interrupted nylon sutures (Ethilon). Mice were monitored until they recovered from

anesthesia; they were then housed singly and treated with Meloxicam as an analgesic. The following week, mice underwent a final IVIS imaging session and were sacrificed.

2.4.15 Immunofluorescence confocal microscopy

Cells were grown on no. 1 glass coverslips for all immunofluorescent immunocytochemistry experiments. Following treatment, *KPV*$^{+/+}$ and *KPV*$^{-/-}$ cells were fixed in methanol for 3–5 minutes. A549 cells were fixed with 2% paraformaldehyde for 7–10 minutes. *KPV*$^{+/+}$ and *KPV*$^{-/-}$ cells were blocked in 5% normal goat serum (NGS) for 1 hour at room temperature. A549 cells were blocked with 1.5% NGS for 30 minutes at 37°C. Cells were then treated with the indicated primary antibodies overnight at 4°C. Cells were washed twice in PBS with 0.10% Tween-20 for 3 minutes each and treated with secondary antibodies conjugated with Alexa Fluor 488 (Invitrogen A-11039, 1:200) and/or Alexa Fluor 568 (Invitrogen A-11004, 1:200), as well as Hoechst nuclear dye (Invitrogen H3570, 1:10,000). Coverslips were mounted and sealed. A Nikon A1R+ laser scanning confocal microscope equipped with a 60× and 100× objective lens was used to acquire images. For experiments with A549 cells, a Zeiss LSM 510 laser scanning confocal microscope equipped with a 63× objective lens was used to acquire images. Nikon NIS-Elements software and ImageJ were used for image processing.

2.4.16 Flow cytometry

Cells were plated in 12-well plates overnight at a density of $0.5x10^5$ cells/well. Cells were then treated with BSO (1 mM) and/or Fer-1 (20 mM) for 48 hours. To accurately measure cell death, we collected the supernatant and all washes in addition to the adherent cells. Briefly, cells were washed with 1X PBS, trypsinized, and suspended in media. Cells were then stained with C-11 BODIPY 581/591 (ThermoFisher) according to the manufacturer's instructions. Finally, cells were stained with Ghost Dye Red 780 (Tonbo Biosciences) and analyzed by flow cytometry immediately.

2.4.17 Reagents

Antibody Target	Company	Host Species	Clone	Catalog Number	Use

Actin	Santa Cruz Biotechnology	Mouse	C-2	sc-8432	WB
Actin	Santa Cruz Biotechnology	Goat	C-11	sc-1615	WB
E-cadherin	Santa Cruz Biotechnology	Rabbit	H-108	sc-7870	WB
GAPDH	Cell Signaling Technology	Rabbit	14C10	2118	WB
GPX4	Abcam	Rabbit	EPNCIR144	ab125066	WB
Keratin	Fitzgerald	Mouse	Ks8.7	10R-C177ax	IF
Ki67	Abcam	Rabbit	polyclonal	ab66155	IHC
Kras	Abcam	Rabbit	polyclonal	ab180772	WB
N-cadherin	Calbiochem	Rabbit	polyclonal	205606	WB
pERK1/2	Cell Signaling Technology	Rabbit	D13.14.4E	4370	IHC
Ras(G12D)	NewEast Biosciences	Mouse		26036	WB
SLC7A11	Invitrogen	Rabbit	polyclonal	PA1-16893	WB
TTF-1	Abcam	Rabbit	EPR8190	ab133638	IHC
Vimentin	Abcam	Rabbit	EPR3776	ab92547	IHC, IF
Vimentin	Biolegend	Chicken	Poly29191	919101	IF
Vimentin	Cell Signaling Technology	Rabbit	R28	3932	IF
Vimentin	Sigma-Aldrich	Mouse	V9	V6630	WB
Vimentin (phospho-Ser55)	Abcam	Mouse	4A4	ab22651	IF

Chapter 3. Vimentin is required for rapid blood clot formation.

3.1 Background

Following injury, hemostasis must occur to initiate wound healing. Endothelial cells secrete von Willebrand factor (vWF), a glycoprotein that activates formation of the platelet plug. Additionally, denuded endothelial cells expose collagen I to the blood vessel; platelets can bind directly to collagen through GP VI and GP Ia/IIa or to collagen-bound vWF via GP Ib-V-IX (144). Activated platelets upregulate integrins which strengthen platelet adhesion to fibrinogen, fibronectin, and vWF (145). Activated platelets also undergo degranulation, releasing vWF, ADP, fibrinogen, and other procoagulants. The coagulation cascade, initiated by tissue factor-induced thrombin activation, leads to the formation of fibrin from circulating fibrinogen. Individual platelets can kink fibrin filaments, leading to compaction of the fibrin network and formation of platelet clusters. This process is actomyosin- and $\alpha_{IIb}\beta_3$-integrin-dependent (146). Once a blood clot has formed, the entire clot contracts, thereby stabilizing the clot and allowing for restored blood flow past an otherwise obstructive thrombus.

Under normal conditions, tissues exist under a mechanical equilibrium, balancing forces like blood pressure, fluid shear stress, tissue stiffness, and fluid (147). Following injury, cells participating in hemostasis must maintain this mechanical equilibrium by sensing and modulating their environment. The primary drivers of changes in clot mechanics are fibrin and platelets. Fibrin fibers undergo strain stiffening, align in response to force, and form viscoelastic networks (148-150). Platelets are mechanoresponsive: they undergo more spread on surfaces with less fibrinogen and higher stiffnesses (151-153). Additionally, as substrate stiffness increases, platelets exert higher pulling forces (154). These feedback loops create a viscoelastic clot that ultimately restores mechanical homeostasis to the damaged tissue.

Vimentin is a cytoskeletal protein that, like fibrin, forms viscoelastic networks that undergo strain stiffening (73). While the roles of actin and non-muscle myosin are well-defined in platelet biology, other cytoskeletal elements, like the vimentin intermediate filament network, are less understood despite their expression in platelets (155, 156). Several reports have indicated a role for vimentin in hemostasis, especially in the early events of the platelet plug. For example, under high shear stress conditions, vimentin on the cell surface binds vWF, strengthening the binding of platelets to the vessel wall (157). This cell surface vimentin also complexes with vitronectin and type 1 plasminogen activator inhibitor, ultimately contributing to inhibition of fibrinolysis (158). However, no studies have fully characterized the contribution of vimentin to the mechanical properties of blood clots after formation. Therefore, we set out to identify how vimentin contributes to the viscoelasticity of clots. We found that vimentin increases both elasticity and viscosity of clots, and that vimentin-null clots are less contractile than WT clots. These clot properties ultimately lead to delayed clotting in vimentin knockout (Vim KO) compared to wildtype (WT) mice.

3.2 Results

3.2.1 Vimentin is ubiquitously expressed in platelets and undergoes a change in architecture during platelet activation

Resting platelets circulate in the blood as biconcave discs (**Figure 3.1A**). Platelets express actin and vimentin ubiquitously (**Figure 3.1A-C**). Interestingly, about 25% of resting human-derived platelets express vimentin in its filamentous and particulate form, while the other 75% only express punctate vimentin (**Figure 3.1A**). Platelets were cultured on glass for one hour to induce activation. When activated, platelets undergo cytoskeletal reorganization and change shape, dramatically increasing their surface area (**Figure 3.1B**). Of note, this activation is marked by a reorganization of vimentin entirely into its particle form in both human- and murine-derived platelets (**Figure 3.1B-C**). Platelets

interact with their environment via two distinct protrusions: lamellipodia and filopodia (159). Lamellipodia are spread, actin-cross linked projections, while filopodia are thin, actin-bundled protrusions. Interestingly, vimentin is present in both lamellipodia and filopodia, yet it does not colocalize with actin filaments.

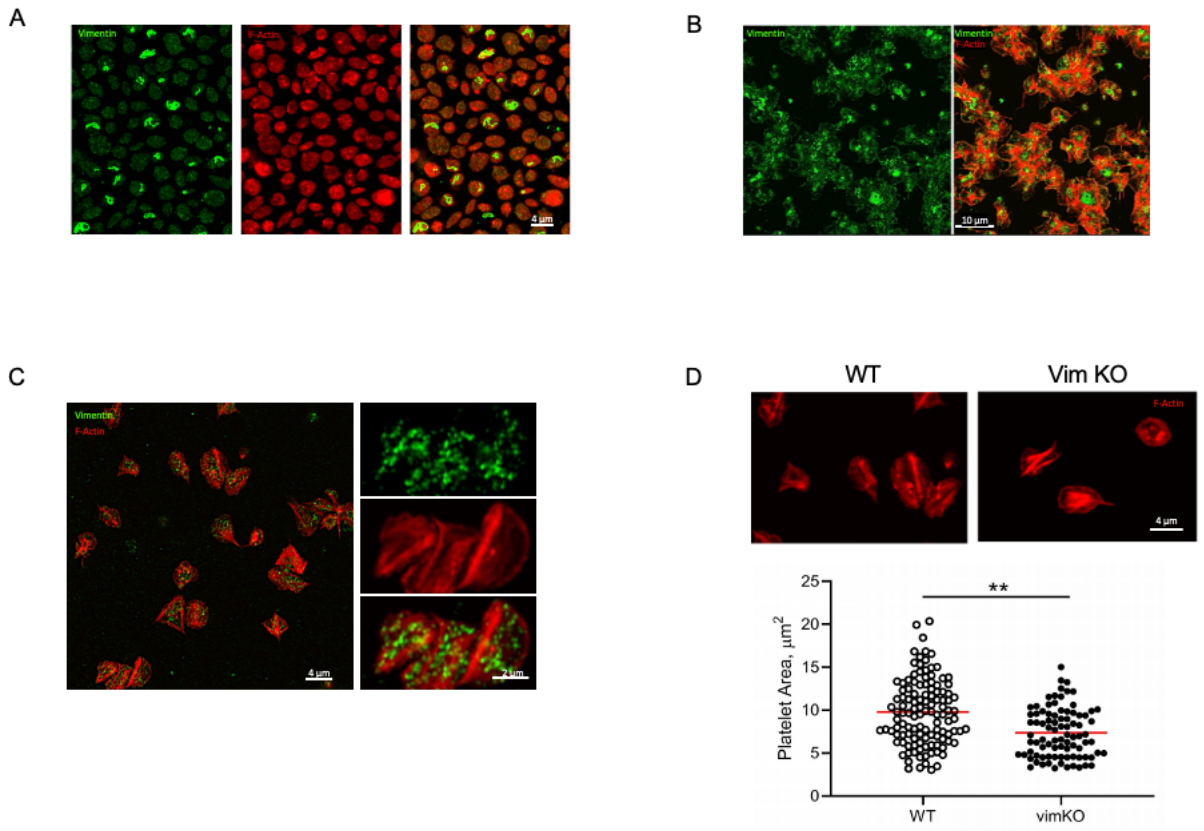

Figure 3.1. Vimentin is present in platelets and facilitates cell spread. (**A**) Human isolated resting platelets were fixed and stained for vimentin and F-actin. (**B**) Human platelets were cultured on glass coverslips for one hour and stained for vimentin and F-actin. (**C**) WT mouse platelets were cultured on fibrinogen for 90 minutes and stained for vimentin and F-actin. (**D**) WT and vimentin KO platelets were cultured on fibrinogen for 90 minutes and stained for F-actin. Platelet area was quantified and data were subject to an unpaired, two-tailed t-test (**p<0.01).

3.2.2 Vimentin knockout platelets undergo less cell spreading than WT platelets

Resting platelets are, on average, 2-3 µm in diameter. Following activation, their diameter increases to about 10 µm (**Figure 3.1A-B**). Larger platelets have greater surface area with which to bind to the vessel wall and to fibrinogen (160). Additionally, larger platelets have more phosphorylated proteins following thrombin stimulation, as well as a greater level of absolute proteins, ATP, and glycogen

(161, 162). Together, these data indicate size of platelets positively correlates with hemostatic potential (163). We cultured platelets isolated from WT or Vim KO mice on fibrinogen for 90 minutes to induce activation, then stained for actin and quantified cell size. Interestingly, Vim KO platelets are significantly smaller in area then WT platelets, indicating that Vim KO platelets undergo less cell spread.

3.2.3 Clots from vimentin knockout mice are less contractile than clots from WT mice

Because of our finding that Vim KO platelets undergo less cell spread than WT platelets, we set out to identify whether Vim KO clots also undergo less contraction. We isolated platelet-rich plasma (PRP) from WT and Vim KO mice, induced clot formation with $CaCl_2$ and thrombin, and traced clot contraction over 1800 seconds (**Figure 3.2A**). We analyzed the kinetics of clot contraction and observed three distinct phases (**Figure 3.2A-B**) as previously described (146). Interestingly, these phases were the same for both WT and Vim KO conditions (t_1: WT=3.0 min, Vim KO = 3.1 min; t_2: WT=7.6 min, Vim KO = 7.6 min), indicating that Vim KO clots do not form more slowly than WT clots. However, Vim KO clots display lower rates of contraction, especially at the "active contraction" (mean SD vs mean SD) and "final contraction" (mean SD vs mean SD) phases. In addition, total contraction is lower for Vim KO clots compared to WT clots. At the endpoint of the experiment, WT clots have contracted about 30%, while Vim KO clots have only contracted about 20%. Together, these results show that, while the relative kinetics of clot contraction are unchanged, Vim KO clots undergo less contraction than WT clots.

A

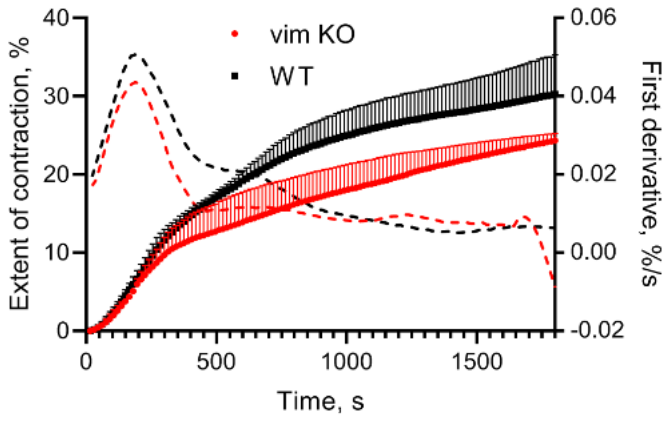

B

	t_1 (min)	t_2 (min)	k_1 (x10^{-2} %/s)	k_2 (x10^{-2} %/s)	k_3 (x10^{-2} %/s)
WT	3.1	7.6	3.6±1.0	3.6±1	1.4±0.5
Vim KO	3.0	7.6	3.1±0.9	2.6±1.2	0.91±0.9

Figure 3.2. Vim KO clots are less contractile than WT clots. (**A**) Whole blood contraction kinetic curves (symbols) for platelet-rich plasma from WT and Vim KO mice. First derivative of the contraction curve (dashed line) reveals three phases of clot contraction. (**B**) Kinetic parameters of the three phases of clot contraction.

We also used a rheological approach to better characterize the mechanical properties of the mouse-derived thrombi. Briefly, we induced clot formation of platelet-rich plasma within a parallel plate rheometer. We imposed a sinusoidal oscillatory shear strain and measured the stress exerted by the clot over a 50-minute period. This normal force, which directly measures the contraction of clot, increased for both WT and Vim KO clots for about 40 minutes before plateauing. However, compared to WT clots, Vim KO clots displayed lower normal forces over the entire course of the measurement. Additionally, Vim KO clots exerted a normal force at 40 minutes that was approximately 6-fold lower than the force exerted by WT clots. By imaging and direct contraction measurements, we conclude that Vim KO clots are less contractile than WT clots.

3.2.4 Vimentin-knockout blood forms less viscoelastic clots than WT blood

Blood clots are canonically viscoelastic, meaning they possess time-dependent mechanical properties. To characterize the viscoelasticity of these clots, we measured the phase shift in shear stress response to determine the storage (G') and loss (G") moduli (**Figure 3.3B-C**). Storage modulus, which describes the elastic properties of the material, increased for both WT and Vim KO clots over the entire time course (**Figure 3.3B**). Vim KO clots displayed a 1.6-fold lower G', and therefore lower elasticity, over the course of clotting compared to WT clots. Therefore, Vim KO clots are less elastic than WT clots.

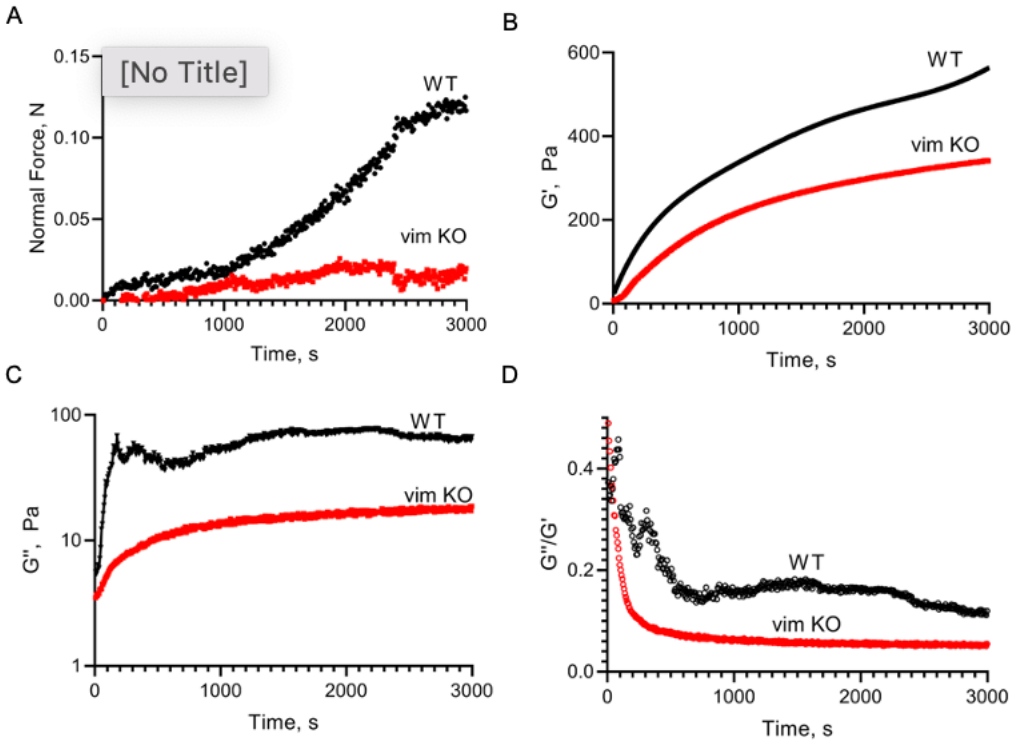

Figure 3.3. Vim KO clots are less elastic and less viscous than WT clots. Parallel plate rheometry was used to measure temporal changes in clot mechanics. (**A**) Dynamic contractile force generated by blood clots from platelet rich plasma isolated from either WT or Vim KO mice. (**B-D**) The storage modulus (G') (**B**), loss modulus (G'') (**C**), and ratio between the two moduli (**D**) were measured (n = 3).

The viscous portion of the clot, described by G", increased for both conditions in the first 200 seconds before reaching a plateau (**Figure 3.3C**). Throughout the course of the experiment, Vim KO clots displayed a 3.6-fold lower G" than WT clots, indicating that WT blood forms more viscous clots than Vim KO blood.

The damping factor of a viscoelastic material is characterized as the ratio of G" to G' and describes the degree of viscous to elastic properties a material displays. Both WT and Vim KO clots have G"/G' values under 1, indicating that both groups behave as a primarily elastic material over the course of clotting (**Figure 3.3D**). This value decreased more rapidly in Vim KO clots than in WT clots and was 2.2-times lower in Vim KO clots at the experimental endpoint. This suggests that vimentin may play a role in the dissipation of mechanical energy within blood clots.

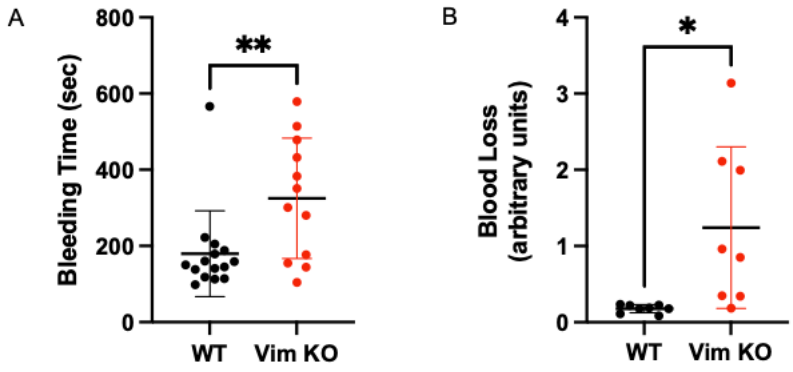

Figure 3.4. Vim KO mice have delayed bleeding cessation. WT and Vim KO mice were subject to a tail bleed assay. (**A**) Elapsed time between injury and first instance of bleeding cessation was measured. (**B**) Blood was collected and measured as OD575 absorbance. Data were subject to an unpaired, two-tailed t-test with *p<0.05, **p<0.01. Data are presented as the mean ± standard deviation.

3.2.5 WT mice form clots *in vivo* more rapidly than Vim KO mice

To determine whether clotting differences *in vitro* mirror *in vivo* differences in hemostasis, we employed a mouse model to study clotting times. Briefly, tails of WT or Vim KO mice were snipped and the time to bleeding cessation was measured. Vim KO mice displayed significantly longer bleeding times than WT mice (324.8±157.9 s vs. 179.7±112.5 s) (**Figure 3.4A**). Accordingly, Vim

KO mice also lost more blood than WT mice (**Figure 3.4B**). Together, these data show that vimentin is required for rapid hemostasis *in vivo*.

3.3 Discussion

In the present study, we found that blood from Vim KO mice forms clots that are less viscous, less elastic, and less contractile. *In vivo*, this corresponds to delayed clotting times in Vim KO compared to WT mice. This study identifies vimentin as a key player in hemostasis, highlighting its potential as molecular target in clotting diseases.

While we now know that vimentin is required for proper clotting, it is still unclear the mechanism by which it promotes hemostasis. We present two mechanisms by which vimentin could be contributing to clotting. The first is that vimentin is required for individual platelet contractility. We observe a change in vimentin architecture following platelet activation (**Figure 3.1A-B**). Vimentin aligns forces during mesenchymal cell migration, and it could play a similar role during platelet contraction (49). Additionally, the smaller size of Vim KO platelets could correspond with a decreased ability to exert force (**Figure 3.1D**). The second possible mechanism is that extracellular vimentin is binding platelets and encouraging their aggregation. This hypothesis is supported by increasing evidence that extracellular vimentin exists on the platelet surface and circulating in the serum (157, 158, 164, 165). Of note, circulating levels of vimentin are associated with a higher risk of stroke (166). It is therefore possible that extracellular vimentin acts along with fibrin as an additional polymer network to which platelets bind. Further study is needed to determine whether one or both mechanisms play a role in clot formation and contraction.

In summary, we have begun to characterize the role of vimentin in blood clot mechanics. Identifying the mechanism by which vimentin acts will determine the types of therapy that can be employed. For example, endogenous vimentin expression would require a therapy targeting vimentin

in platelets or megakaryocytes, while extracellular vimentin could be targeted through a blocking antibody. Together, this represents an exciting step in characterizing clot mechanics and ultimately improving patient outcomes.

3.4 Materials and Methods

3.4.1 Platelet isolation and culture

Whole blood was drawn by venipuncture into 3.8% trisodium citrate (9:1 v/v) from healthy volunteers not taking aspirin or other medications known to affect platelet function for at least 10 days. Informed consent was obtained in accordance with a protocol approved by the University of Pennsylvania Institutional Review Board. To obtain platelet-rich plasma (PRP), citrated blood was centrifuged at 210xg at 25°C for 15 min. PRP samples were kept at room temperature and studied within 4 hours of blood collection.

Vimentin knockout (Vim KO) 129/Sv6 mice were a generous gift from Albee Messing (Madison, WI). Blood from 129/Sv6 WT and Vim KO mice was collected using cardiac puncture and stabilized with 3.2% trisodium citrate (9:1 v/v). Blood was treated with $CaCl_2$ (2 mM) and thrombin (5 U/mL) to form clots.

3.4.2 Immunocytochemistry

Human platelets were cultured on glass and stained with anti-vimentin (Novus Biologicals, NB300-223). Then, cells were stained with an Alexa Fluor 488 secondary antibody and Alexa Fluor 594-phalloidin to probe for F-actin. Mouse platelets were cultured on fibrinogen (200 μg/mL) for 90 minutes then fixed and stained. Slides were imaged with a Zeiss 880 Airyscan confocal microscope.

3.4.3 Rheometry

Viscoelastic properties of whole blood clots were characterized using an AR-G2 rheometer. 100 μL of blood was treated with $CaCl_2$ and thrombin to form clots in a 300 μm gap between horizontal

parallel plates. To prevent liquid evaporation, a thin layer of silicon oil was applied at the edge of the clot. During a strain-controlled test, the rheometer imposed a sinusoidal oscillatory shear strain on the clot sample in the form of $\gamma = \gamma_0 \sin(\varpi t)$, where ϖ is the frequency and γ_0 is the strain amplitude, and the shear stress σ required to impose such a deformation was measured. For a linear viscoelastic material, shear stress is a sinusoidal function with some phase shift δ, i.e. $\sigma = \sigma_0 \sin(\varpi t+\delta)$, where σ_0 is the shear stress amplitude. The elastic response of the clot is characterized by the shear elastic modulus, G', corresponding to the part of shear stress, which isin phase with strain and is calculated as $G' = (\sigma_0/\gamma_0)\cos(\delta)$. The viscous response of the clot to applied shear is quantified in terms of the shear loss modulus, G", calculated as the out-of-phase part of the stress as $G" = (\sigma_0/\gamma_0)\sin(\delta)$. To probe a clot's shear stress-strain response, the shear strain of 3% at the oscillatory frequency of 1 Hz was applied to a 20 mm upper plate of the rheometer to produce a linear stress-strain response. The storage modulus (G'), the loss modulus (G"), and the normal force were measured during the oscillatory test for 3000 seconds.

3.4.4 Contraction of blood clots

Clot size changes were tracked by measuring temporal alterations of clot-induced light scattering followed by image analysis of the serial images acquired by a thrombodynamics Analyzer System (Hemacore, Moscow, Russia). Clots were formed in plastic cuvettes with walls coated in 4% v/v Triton X-100 in PBS; clotting was initiated with $CaCl_2$ (2 mM) and thrombin (5 U/mL). 80 μL of blood was transferred to cuvettes and imaged using a CCD camera every 15 seconds for 30 minutes. Image sequence was analyzed computationally to measure lag time, area under the curve, relative clot size at end point, and average velocity.

3.4.5 Tail bleed assay

Mice were anesthetized with ketamine (100 mg/kg) and xylazine (10 mg/kg). The distal 2 mm of the tail was cut with a fresh razor blade and the tail was immediately placed in 37°C 1X PBS. The time

to the first instance of bleeding cessation was recorded. The collected blood was centrifuged at 250xg for 15 minutes and resuspended in erythrocyte lysis buffer. Hemoglobin was measured as OD575.

Chapter 4. Design of an inflammasome-targeting nanotherapeutic.

4.1 Background

Acute respiratory distress syndrome (ARDS) is a prevalent and deadly disease, resulting in approximately 10% of intensive care unit admissions globally, with 75,000 deaths per year in the US (167). Despite its prevalence, there is no cure for ARDS and therapy is limited to supportive care. A wide range of insults, including bacterial and viral infections, can cause acute lung injury (ALI) which can ultimately lead to ARDS. While inflammation is critical to clear pathogens, prolonged inflammation can lead to tissue damage, which, in the lung, leads to dysregulated blood oxygenation and can ultimately cause organ failure and death. Most ARDS deaths occur days to weeks after disease onset, yet there are no viable treatment options that target mechanisms that are active in this late stage of inflammation.

ALI occurs when an insult damages the epithelial layer in the alveoli. This injury leads to recruitment of immune cells, which secrete pro-inflammatory factors. One of these factors, IL-1β, is critical to prolonging this inflammatory phase. Of note, transient expression of IL-1β is sufficient to cause lung injury (62). Therefore, interrupting IL-1β release is an attractive route for therapy. Our group found that vimentin knockout (Vim KO) mice challenged with several inducers of ALI (LPS, influenza, bleomycin, asbestos) are protected from lung injury (51). Specifically, vimentin is required for formation of the NLRP3 inflammasome, which is needed for production of IL-1β. Monocyte-derived alveolar macrophages (MoAMs) are the key player in potentiating this signal, and specifically knocking out vimentin in these cells is sufficient to prolong survival following influenza infection (51, 168).

We therefore set out to design a therapy that could disrupt vimentin assembly in MoAMs to improve ARDS/ALI outcomes. To this end, we employed Five1 and WFA, two well-characterized

drugs that cause vimentin intermediate filament (VIF) disassembly (112-114, 133, 169, 170). However, Five1 and WFA are both insoluble in water, making them hard to deliver. We used an established nanocarrier formula to solve this delivery issue. Five1 or WFA was encapsulated in the amphiphilic diblock copolymer poly(ethylene glycol)-*block*-poly(propylene sufide) (PEG-b-PPS) (171). This material is composed of a hydrophilic polymer, PEG, and a hydrophobic portion, PPS. PEG is already FDA-approved and is commonly used to mask nanoparticles, which leads to greater half-lives of the particles (172). PPS is advantageous because it disassembles under oxidative conditions (such as those in the endolysosome), allowing for release of its cargo inside the cell (173). Compared to free drug, PEG-b-PPS nanocarriers can increase bioavailability, *in vivo* half-life, and cell uptake (174, 175). Additionally, PEG-b-PPS micelles are taken up preferentially by macrophages compared to dendritic cells, neutrophils, lymphocytes, and NK cells (176). Furthermore, PEG-b-PPS nanostructures are non-toxic in mice and non-human primates, making them an appealing avenue for therapy (177).

We designed PEG-b-PPS micelles that disrupt VIF assembly in murine macrophages. We show that, *in vitro*, PEG-b-PPS micelles loaded with Five1 can effectively suppress IL-1β release from macrophages. This proof-of-principle study marks the first step in creating novel treatments for ARDS.

4.2 Results

4.2.1 Five1 and WFA inhibit formation of the NLRP3 inflammasome.

Five1 and WFA cause VIF disassembly by inducing vimentin phosphorylation at serine-55 (114, 169). We confirmed vimentin disassembly in BMDMs treated with both agents (**Figure 4.1A**). Following treatment with either Five1 or WFA, vimentin becomes phosphorylated at Ser-55 and the vimentin network collapses around the nucleus.

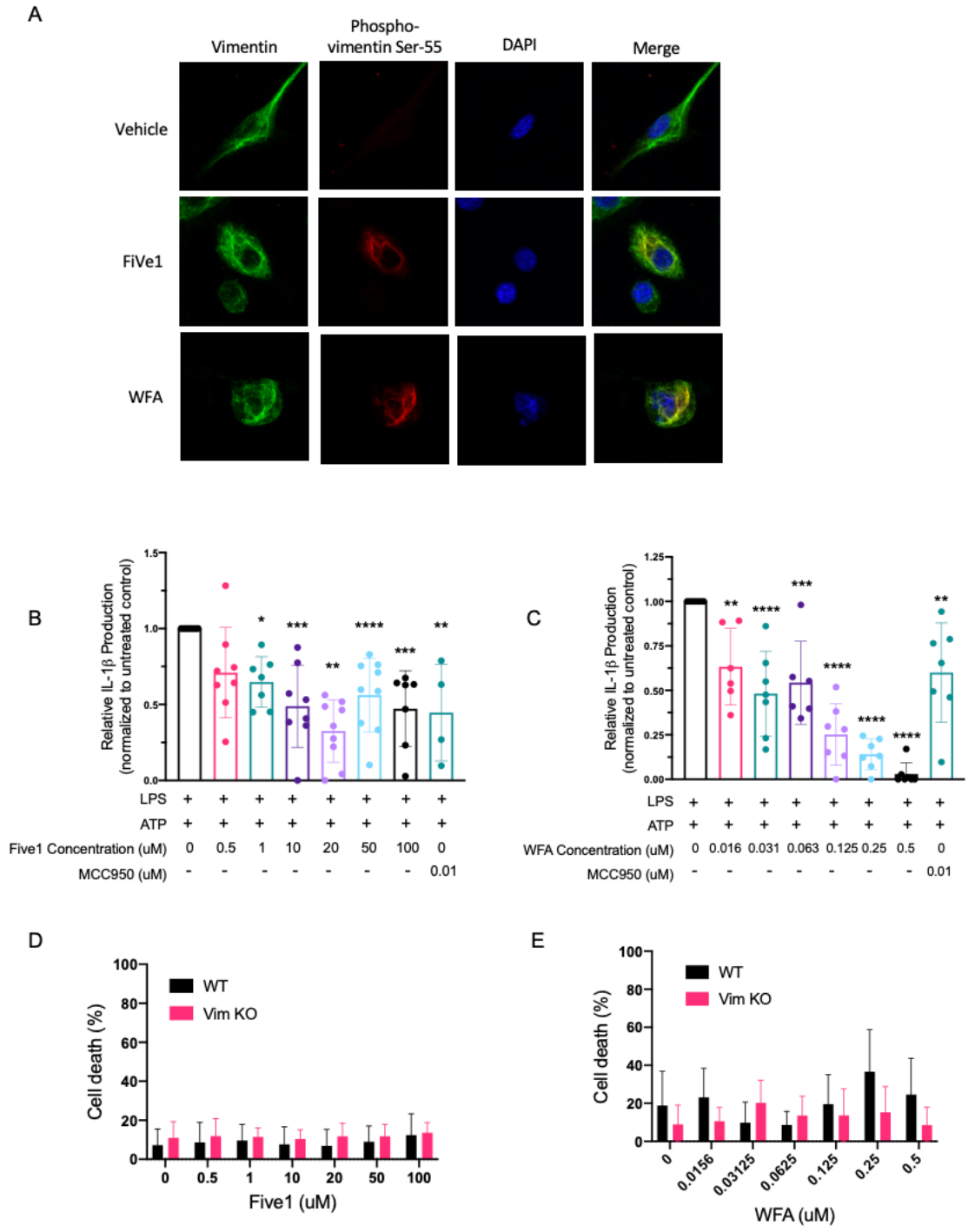

Figure 4.1. Five1 and WFA decrease IL-1β release in BMDMs. (**A**) BMDMs treated with Five1 or WFA and were stained with antibodies against vimentin and phospho-Vim-Ser55. (**B-E**) BMDMs were treated for 24 hours with LPS and Five1 (**B**) or WFA (**C**); ATP was added for 4 additional hours. IL-1β released in the supernatant was measured via ELISA (**B-C**). Cell death was measured at the tested concentrations (**D-E**). Groups were compared to the vehicle control and subject to a two-tailed t-test. Data are presented as mean ± SD.

Inflammasome activation requires two signaling events to occur. The first (signal 1) is an inflammatory stimulus that upregulates transcription of pro-IL-1β. The second signal (signal 2) is required for formation of the inflammasome complex, caspase-1 activation, and IL-1β maturation. To test whether pharmacologically disassembling vimentin leads to suppression of IL-1β release, we first induced NLRP3 inflammasome activation in BMDMs. To this end, BMDMs were treated with Five1 and WFA in combination with LPS for 24 hours to initiate signal 1. ATP (signal 2) was added for the last 4 hours and the IL-1β in the supernatant was measured. MCC950 was added as a control. Five1 displayed a dose-dependent decrease in IL-1β, with an IC50 of 1.22 μM (**Figure 4.1B**). However, even at the highest dose (100 μM), Five1 did not completely suppress IL-1β production. WFA also caused a dose-dependent decrease in IL-1β with an IC50 of 0.1729 μM, about 10-fold lower than the IC50 of Five1 (**Figure 4.1C**). Interestingly, WFA caused complete suppression of IL-1β at the highest tested dose (0.5 μM). We next tested whether Five1 or WFA induced cell death in BMDMs. Importantly, we used BMDMs derived from 129Sv/6 mice; these mice have an inactivating mutation in caspase-11 which eliminates their ability to undergo cell death in response to IL-1β signaling (178). Therefore, any cell death observed would be from the drug treatment, and not from inflammasome activation. Additionally, we used BMDMs from Vim KO mice as a negative control to test whether cell death was vimentin dependent. We did not observe any difference in cell death in the Five1 treated conditions compared to vehicle controls or in WT compared to Vim KO cells (**Figure 4.1D**). While not significant, cell death increased slightly in WFA-treated cells at 0.25 μM compared to vehicle control and was slightly higher in WT compared to Vim KO cells, suggesting that WFA causes cell death by a vimentin-dependent mechanism. However, the IC50 for WFA was lower than the dose that caused cell death, so we concluded that the IC50 for WFA was appropriate for the next steps.

4.2.2 Design of a Five1 micelle.

Because of the negligible effect of Five1 on cell death, we decided to load Five1 in PEG-b-PPS micelles. First, we performed a wavelength sweep of Five1 to determine if it had a unique absorbance that would allow us to measure its loading efficiency. We found that the peak absorbance of Five1 is at 337 nm, and that Five1 can be detected at a concentration as low as 0.125 mg/mL (**Figure 4.2A**). We used thin film (TF) and flash nanoprecipitation (FNP) to fabricate Five1-loaded micelles (Five1-MCs) dendritic cell activation (179). DiI, a lipophilic fluorophore, was added during fabrication as well. We then lyophilized and dissolved the micelles and measured the amount of drug that was loaded. We found that TF resulted in a loading efficiency of 12.878±7.145%, while FNP resulted in a loading efficiency of 40.283±23.406%. Therefore, we used FNP to fabricate micelles.

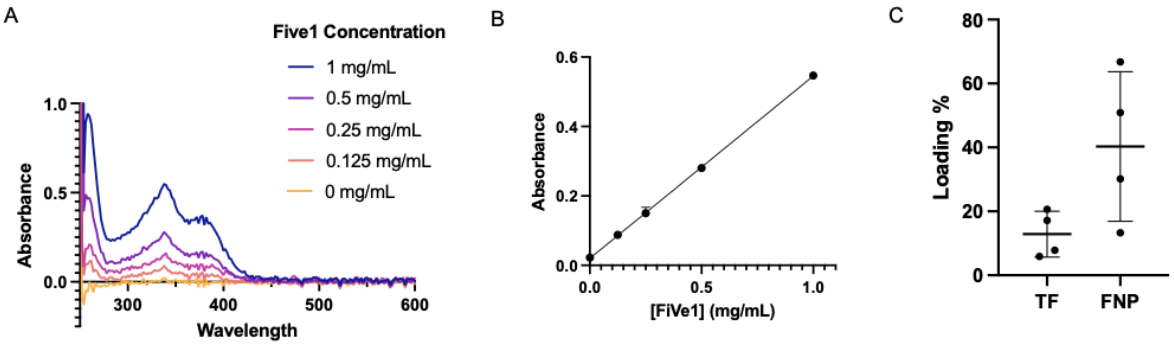

Figure 4.2. Five1 is encapsulated via flash nanoprecipitation. (**A**) Five1 was resuspended in DMF at the concentrations shown and its absorbance was measured over the full spectrum (200-800 nm). (**B**) The absorbance of Five1 at 337 nm was measured and was plotted against the known concentration. Linear regression was used to interpolate a standard curve. (**C**) Following micelle formulation using either thin film (TF) or flash nanoprecipitation (FNP), micelles were dissolved to solubilize the loaded drug. Using the absorbance measurements, loading efficiency was calculated. Data in (**C**) are presented as the mean ± SD.

4.2.3 Five1-MCs decrease IL-1β release in BMDMs.

To first assess whether BMDMs take up MCs, we treated BMDMs with blank MCs and measured their uptake by flow cytometry. About 14.5% of BMDMs take up micelles at a 1:50 concentration (**Figure 4.3A**). MCs were then loaded with a range of Five1 concentrations; the final concentrations

were calculated using the absorbance method described above. We used 3 final concentrations: 0.57

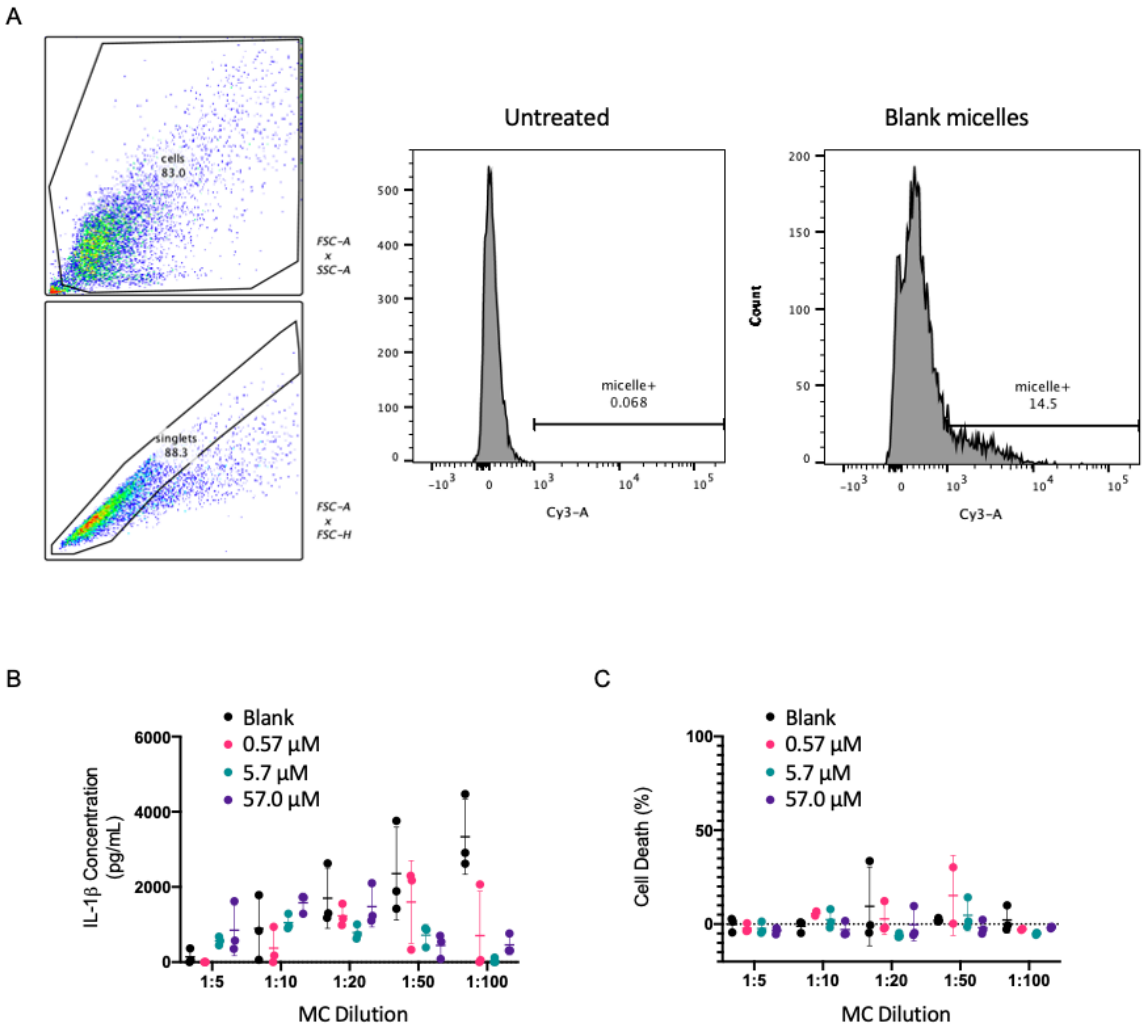

Figure 4.3. Five1-MCs suppress IL-1β release in BMDMs. BMDMs were treated with Five1-MCs and LPS for 24 hours and treated with ATP for 4 hours. (**A**) BMDMs were subject to flow cytometry. The gating strategy is shown. MCs contain a Cy3 tag. BMDMs were either untreated or treated with blank micelles and Cy3 signal was detected. (**B**) Three different concentrations of Five1 were loaded in micelles; cells were then treated with varying dilutions of Five1-MCs in media containing LPS. Following ATP treatment, IL-1β levels in the supernatant were measured by ELISA. (C) Cell death was measured by flow cytometry.

µM, 5.7 µM, and 57.0 µM. These Five1-MCs were then further diluted in media (1:5-1:100) and added, along with LPS, to the BMDMs. Following incubation with ATP, we collected the supernatant and analyzed IL-1β release (**Figure 4.3B**). Interestingly, under low MC dilutions (1:5, 1:10, 1:20), we observed no difference between blank-MC- and any of the Five1-MC-treated

conditions. Of note, blank-MC suppressed IL-1β release at these low dilutions. However, at higher particle dilutions, treatment with blank-MCs resulted in high levels of IL-1β release (between 2000-3500 pg/mL). In the 1:50 and 1:100 treatment groups, Five1-MCs decreased IL-1β release in a concentration-dependent manner. Importantly, we observed no significant cell death in the Five1-MC-treated cells, indicating that the MCs are nontoxic to BMDMs, even at high media levels. Together, we provide proof-of-principle evidence that Five1-MCs can suppress IL-1β release from BMDMs in culture without causing cell death.

4.3 Discussion

Here, we designed a Five1-MC that suppresses IL-1β release by causing vimentin disassembly. We show that these MCs get taken up by macrophages and do not cause cell death *in vitro*. Additionally, we have identified an IC50 for Five1 and WFA and show that WFA has the capacity to completely suppress IL-1β. Finally, we have optimized an in vitro dosing strategy for Five1-MCs.

Interestingly, we observed very low levels of IL-1β when BMDMs were treated with high concentrations of blank particles. This is surprising because we expect the MCs alone to not affect NLRP3 inflammasome function. Therefore, we expect that the MCs are directly binding to LPS and blocking its uptake by cells. Without this signal 1, the inflammasome does not become activated and IL-1β is not released. Therefore, we must be mindful that MCs are not quenching LPS *in vitro* when designing further experiments.

This project requires *in vivo* validation. To this end, we plan to infect mice with influenza A (IAV); the mortality rate of IAV-induced ARDS is approaching 40%, making treatment of IAV-induced lung injury a critical clinical target (180-183). We plan to assess the *in vivo* efficacy of therapeutic Five1-MCs following IAV infection. Additionally, we will characterize cell uptake to

ensure that Five1-MCs are being taken up preferentially by alveolar macrophages. If Five1-MCs are taken up by off-target cells, we can modify their surface to actively target macrophages (184). For example, we can add ligands specific to receptors expressed by macrophages such as mannose receptors, Fc receptors, or scavenger receptors (185). These experiments will allow us to identify whether this is a clinically feasible approach to treating IAV-induced ARDS.

4.4 Materials and Methods

4.4.1 Cell isolation and culture.

BMDMs were isolated from bone marrow extracted from 129/Sv6 mice and purified through a Ficoll-Paque gradient. Cells were differentiated to macrophages in DMEM containing 20% fetal bovine serum and 30% L929 cell supernatant for 5 days as described by Barish et al. (186). BMDMs were plated overnight in a 96-well plate at a concentration of 100,000 cells/well. Cells were washed with 1X PBS and treated with LPS (100 ng/mL) and the indicated drugs for 4 hours. ATP (5 mM) was added directly to the cells for an additional half hour.

4.4.2 Immunocytochemistry.

BMDMs were cultured on glass coverslips as described above and treated with the indicated reagents for 24 hours. Cells were fixed in methanol at -30C for 5 minutes then incubated with primary antibodies overnight (Anti-vimentin Thermo/Invitrogen PA1-10003, polyclonal chicken, 1:1000; anti-phospho-vimentin S55 antibody: Abcam ab22651, monoclonal mouse, 1:100). Secondary antibodies were added for two hours (Alexa Fluor 488 goat anti-chicken [GAC] IgY H+L, Life Technologies A11039, 1:200; Alexa Fluor 568 goat anti-mouse [GAM] IgG H+L, Life Technologies A11004, 1:200) then coverslips were mounted in DAPI-containing mounting media. Cells were imaged with a Nikon A1R Spectral microscope.

4.4.3 Enzyme-linked absorbance assay (ELISA)

At experimental endpoints, cell supernatant was collected and subject to an ELISA to probe for IL-1β (Invitrogen) subject to manufacturer's instructions.

4.4.4 LDH Assay

Cell death was measured using the Cytotoxicity Detection Kit-Plus LDH Kit (Roche). Cells were incubated with LPS and indicated concentrations of Five1 or WFA for 24 hours, with ATP added for the final 4 hours. Cells treated with 2% Triton X-100 for 1 hour were used as a high control. Media alone was used as the low control. Cell viability was calculated as

$$\frac{experimental\ value - low\ control}{high\ control - low\ control}\ x\ 100\%.$$

4.4.5 Five1-MC fabrication

Thin film hydration was conducted as previously described (174). For thin film (TF) hydration, 10 mg of polymer with 0.0625% by weight of hydrophilic DiI and stock Five1 (225 mg, 22.5 mg, or 2.25 mg) were dissolved in 1 mL of DCM (4.5 mg/mL). The organic phase was vacuum-desiccated overnight in glass HPLC vials, forming a thin film on the surface. Thin films were hydrated with 1X PBS and agitated overnight at room temperature to form Five1-loaded micelles (Five1-MCs). Samples were filtered through Sephadex LH-20 hydrophobic resin and washed with 1X PBS to remove free drug. Micelles were fabricated via flash nanoprecipitation following established methods (174, 187, 188). 20 mg polymer with 0.0625% by weight of DiI and Five1 (225 mg, 22.5 mg, or 2.25 mg) were solubilized in THF (4.5 mg/mL). Separate syringes were loaded with either the DiI-Five1-THF organic phase or 1X PBS in equal volumes and anchored to a confined impingement jet block (189). The phases were mixed in the block and the resulting micelles were collected in 1X PBS, desiccated overnight, filtered through Sephadex LH-20 resin, and washed with 1X PBS.

4.4.6 Flow cytometry

At experimental endpoints, cells were collected and stained with Ghost Dye Red780 viability dye (Tonbo Biosciences). Samples were analyzed on a 3C.A1 LSR Fortessa 1 Analyzer (RHLCCC).

Gating was performed to exclude debris and doublets. Dead cells were detected with the APC-Cy7 filter and DiI+ micelles were detected with the Cy3 filter. Cy3 is shown on live cells.

Chapter 5. Future directions.

5.5 Vimentin in fibrosis: a potential role for mechanosensing.

Idiopathic pulmonary fibrosis (IPF) is a progressive lung disease that is incurable due to the formation of scar tissue and resulting impaired lung function. Approximately 130,000 Americans suffer from IPF, with an estimated 50,000 new cases diagnosed each year. Mortality rates from IPF have increased significantly in recent years, thereby increasing the demand for pulmonary fibrosis research. Although it is well accepted that fibrosis is a central component of pathogenesis in IPF, the mechanisms that orchestrate fibrotic processes are poorly defined and represent a major knowledge gap in the field. The development of novel anti-fibrotic therapy will depend on better understanding of molecular mechanisms that contribute to fibrosis-associated fibroblast and myofibroblast cell accumulation.

In IPF, a buildup of connective tissue in the small airways causes the alveolar walls to become stiff, which limits proper oxygen diffusion into the bloodstream. Myofibroblasts are the main effector cell in IPF; they are defined by their expression of α-smooth muscle actin (α-SMA), high levels of collagen synthesis, and invasive phenotype. When activated from their fibroblast progenitors, myofibroblasts migrate to fibrotic lesions and synthesize a stiff, collagen-rich extracellular matrix (ECM). In turn, myofibroblasts respond to their stiff environment by synthesizing more ECM and becoming more migratory (190). This positive feedback loop between myofibroblasts and the fibrotic extracellular matrix sustains and amplifies fibrosis. The development of novel therapeutic approaches for IPF would be greatly facilitated by mechanistic understanding of the aberrant behavior of the lung mesenchymal cells that accumulate and drive IPF pathogenesis.

Vimentin is a type III intermediate filament that is expressed in mesenchymal cells, such as fibroblasts and myofibroblasts. However, the function of vimentin has not been identified in adult fibrotic lung diseases. We previously reported that vimentin-null mice were protected from bleomycin-induced pulmonary fibrosis (51). Specifically, we demonstrated that bleomycin-treated, vimentin-null mice had decreased collagen deposition and reduced lung stiffness compared to wild-type mice. In addition, our preliminary data provides direct clinical evidence of vimentin upregulation in lung mesenchymal cells derived from fibrotic lesions in patients with IPF (**Figure 5.1A-B**). Collectively, these results suggest that vimentin functions as a positive regulator of ECM production and myofibroblast activation in pulmonary fibrosis.

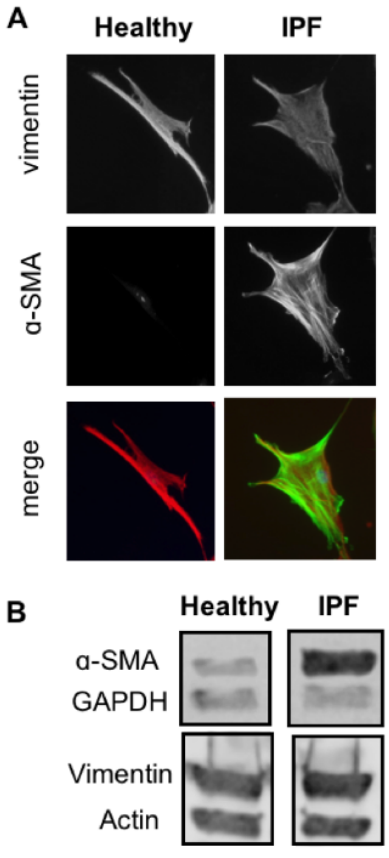

Figure 5.1. Increased α-SMA and stable vimentin expression in IPF-derived fibroblasts. (**A**) Representative images of α-SMA (*green*) and vimentin (*red*) expression in healthy and IPF lung fibroblasts. (**B**) Western blot of α-SMA and vimentin in lung fibroblasts derived from healthy and IPF patients. GAPDH and actin are used as lane loading controls.

We propose to study the role of vimentin in pulmonary fibrosis, with an emphasis on the role of vimentin in myofibroblasts. Previous studies have highlighted the role of vimentin in cell motility and collagen production, two important facets of lung mesenchymal cells that drive IPF pathogenesis. Specifically, vimentin promotes fibroblast migration and collagen contraction (47). Vimentin also binds and stabilizes *Col1a1* and *Col1a2* mRNA (56). Furthermore, vimentin intermediate filaments have unique mechanical properties through which they respond to the extracellular environment: they are flexible, can resist breakage under high mechanical strains, and can increase cell stiffness in response to mechanical stress (73, 191). The

role of vimentin in cell motility and collagen production may be directly dependent on its distinct mechanical properties.

Table 1. Measurements of lung injury and fibrosis.		
Outcome	Assay	Specimen
Lung mechanics	Flexivent	Lung
Characterization of acute lung injury	Wet-to-dry ratio	Lung
	Protein content	BAL fluid
	Cell count	BAL fluid
Tissue stiffness	Tissue slices will be subject to atomic force microscopy with a 5-um sphere-tipped probe. Force and indentation depth will be converted to elastic modulus using the Hertz spherical indentation model.	200 um lung slices
Histological analysis of fibrosis	Lungs and heart will be removed en bloc, fixed, embedded in paraffin, sectioned, and stained with H&E	4 um lung sections
Overall collagen deposition	Picosirius red, Masson's trichrome staining	4 um lung sections
	qRT-PCR, Western blot	Lung homogenates
Insoluble collagen deposition	Sircol assay	Lung
Soluble collagen deposition	Hydroxyproline assay	Lung
Vimentin content	Vimentin immunohistochemistry	4 um lung sections
	qRT-PCR, Western blot	Lung homogenates
Myofibroblast activation	α-SMA immunohistochemistry	4 um lung sections
	α-SMA qRT-PCR, Western blot	Lung homogenates
	Lungs will be dissociated into single-cell suspensions and subjected to flow cytometry (CD45-/CD31-/CD326-/MHY11-/a-SMA+)	Lung homogenates
Inflammatory cytokines (IL-6, TNFa)	ELISA	BAL fluid
Fibrotic cytokines (TGF-β, PDGF)	ELISA	BAL fluid

Table 5.1. Methods for evaluating lung injury and fibrosis.

We hypothesize that vimentin is required by fibroblasts for development of pulmonary fibrosis through regulation of the stiffness-mediated differentiation of fibroblasts to myofibroblasts. We first aim to test the requirement of fibroblast vimentin expression in promoting lung fibrosis. To this end, we created a mouse in which we can conditionally knockout vimentin in fibroblasts. These mice were created by crossing the $Vim^{fl/fl}$ mouse with a mouse that expresses estrogen-receptor-restricted Cre recombinase driven by the *Col1a2* promoter (*Col1a2-CreERT*$^{+/-}$). *Col1a2* is a gene that codes for type I collagen; it is expressed in fibroblasts and is upregulated in lung injury (192). We plan to administer bleomycin to these mice and characterize their outcomes as described in **Table 5.1**. By comparing mice with WT versus Vim KO fibroblasts, we can evaluate myofibroblast differentiation in the absence of vimentin and determine if vimentin is required by mesenchymal cells for the development of lung fibrosis.

We next aim to identify if vimentin is required for stiffness-induced myofibroblast differentiation. While stiff tissue has traditionally been considered merely a consequence of fibrosis, recent evidence suggests that it is sufficient to cause myofibroblast differentiation and is thus a key driver of IPF (190, 193-195). Additionally, the mechanical properties of vimentin are important for cell function. Vimentin filaments can withstand large strains without rupturing and can cause cells to stiffen at high levels of stress (73, 191). In addition, exposure to stiff substrates causes a change in vimentin organization: filament networks dissociate into soluble subunits that can serve as signaling molecules (196). Because of vimentin's unique response to cellular stress, we hypothesize that vimentin is necessary for stiffness-mediated myofibroblast differentiation. To test this hypothesis, we will create tunable polyacrylamide (PA) gels as described previously (197). We will fabricate substrates with elastic moduli within the range of healthy (E=0.5 kPa) and fibrotic (E=20 kPa) stiffnesses (193). PA gels will then be coated with a thin layer of collagen I which will provide cells

physiologically relevant binding sites, while preserving the stiffness of the underlying PA. We can then culture WT and Vim KO (or normal and CRISPR-edited human cells) on these PA gels of varying stiffnesses and evaluate outcomes of myofibroblast differentiation, including gene expression profiles, collagen production, and cell motility. Together, these experiments will allow us how vimentin is involved in myofibroblast signaling in response to stiffness.

The existing paradigm of myofibroblast differentiation lacks a detailed explanation of how fibroblasts differentiate into pathogenic myofibroblasts in response to substrate stiffness. We hypothesize that vimentin is the missing link between substrate stiffness and myofibroblast differentiation. Importantly, these proposed experiments aim to identify key molecular targets to expand understanding of fibrosis and ultimately to improve treatment options for patients with IPF.

References

1. Ishikawa H, Bischoff R, Holtzer H. Mitosis and intermediate-sized filaments in developing skeletal muscle. J Cell Biol. 1968;38(3):538-55. Epub 1968/09/01. doi: 10.1083/jcb.38.3.538. PubMed PMID: 5664223; PMCID: PMC2108373.
2. Oshima RG. Intermediate filaments: a historical perspective. Exp Cell Res. 2007;313(10):1981-94. Epub 2007/05/12. doi: 10.1016/j.yexcr.2007.04.007. PubMed PMID: 17493611; PMCID: PMC1950476.
3. Ridge KM, Eriksson JE, Pekny M, Goldman RD. Roles of vimentin in health and disease. Genes Dev. 2022;36(7-8):391-407. Epub 2022/04/30. doi: 10.1101/gad.349358.122. PubMed PMID: 35487686; PMCID: PMC9067405.
4. Starger JM, Goldman RD. Isolation and preliminary characterization of 10-nm filaments from baby hamster kidney (BHK-21) cells. Proc Natl Acad Sci U S A. 1977;74(6):2422-6. Epub 1977/06/01. doi: 10.1073/pnas.74.6.2422. PubMed PMID: 329284; PMCID: PMC432184.
5. Zackroff RV, Goldman RD. In vitro assembly of intermediate filaments from baby hamster kidney (BHK-21) cells. Proc Natl Acad Sci U S A. 1979;76(12):6226-30. Epub 1979/12/01. doi: 10.1073/pnas.76.12.6226. PubMed PMID: 293716; PMCID: PMC411836.
6. Herrmann H, Kreplak L, Aebi U. Isolation, characterization, and in vitro assembly of intermediate filaments. Methods Cell Biol. 2004;78:3-24. PubMed PMID: 15646613.
7. Hyder CL, Pallari HM, Kochin V, Eriksson JE. Providing cellular signposts--post-translational modifications of intermediate filaments. FEBS Lett. 2008;582(14):2140-8. Epub 2008/05/27. doi: 10.1016/j.febslet.2008.04.064. PubMed PMID: 18502206.
8. Robert A, Rossow MJ, Hookway C, Adam SA, Gelfand VI. Vimentin filament precursors exchange subunits in an ATP-dependent manner. Proc Natl Acad Sci U S A. 2015;112(27):E3505-14. Epub 2015/06/26. doi: 10.1073/pnas.1505303112. PubMed PMID: 26109569; PMCID: PMC4500282.
9. Eriksson JE, He T, Trejo-Skalli AV, Harmala-Brasken AS, Hellman J, Chou YH, Goldman RD. Specific in vivo phosphorylation sites determine the assembly dynamics of vimentin intermediate filaments. J Cell Sci. 2004;117(Pt 6):919-32. Epub 2004/02/06. doi: 10.1242/jcs.00906. PubMed PMID: 14762106.
10. Helfand BT, Mendez MG, Murthy SN, Shumaker DK, Grin B, Mahammad S, Aebi U, Wedig T, Wu YI, Hahn KM, Inagaki M, Herrmann H, Goldman RD. Vimentin organization modulates the formation of lamellipodia. Mol Biol Cell. 2011;22(8):1274-89. Epub 2011/02/25. doi: 10.1091/mbc.E10-08-0699. PubMed PMID: 21346197; PMCID: PMC3078081.
11. Mendez MG, Restle D, Janmey PA. Vimentin enhances cell elastic behavior and protects against compressive stress. Biophys J. 2014;107(2):314-23. doi: 10.1016/j.bpj.2014.04.050. PubMed PMID: 25028873; PMCID: PMC4104054.
12. Colucci-Guyon E, Portier MM, Dunia I, Paulin D, Pournin S, Babinet C. Mice lacking vimentin develop and reproduce without an obvious phenotype. Cell. 1994;79(4):679-94. Epub 1994/11/18. doi: 10.1016/0092-8674(94)90553-3. PubMed PMID: 7954832.
13. Wilhelmsson U, Stillemark-Billton P, Boren J, Pekny M. Vimentin is required for normal accumulation of body fat. Biol Chem. 2019;400(9):1157-62. Epub 2019/04/18. doi: 10.1515/hsz-2019-0170. PubMed PMID: 30995202.
14. Heid H, Rickelt S, Zimbelmann R, Winter S, Schumacher H, Dorflinger Y, Kuhn C, Franke WW. On the formation of lipid droplets in human adipocytes: the organization of the perilipin-vimentin cortex. PLoS One. 2014;9(2):e90386. Epub 2014/03/04. doi: 10.1371/journal.pone.0090386. PubMed PMID: 24587346; PMCID: PMC3938729.

15. Franke WW, Hergt M, Grund C. Rearrangement of the vimentin cytoskeleton during adipose conversion: formation of an intermediate filament cage around lipid globules. Cell. 1987;49(1):131-41. Epub 1987/04/10. doi: 10.1016/0092-8674(87)90763-x. PubMed PMID: 3548999.
16. Shen WJ, Patel S, Eriksson JE, Kraemer FB. Vimentin is a functional partner of hormone sensitive lipase and facilitates lipolysis. J Proteome Res. 2010;9(4):1786-94. Epub 2010/02/11. doi: 10.1021/pr900909t. PubMed PMID: 20143880; PMCID: PMC2849902.
17. Shen WJ, Zaidi SK, Patel S, Cortez Y, Ueno M, Azhar R, Azhar S, Kraemer FB. Ablation of vimentin results in defective steroidogenesis. Endocrinology. 2012;153(7):3249-57. Epub 2012/04/27. doi: 10.1210/en.2012-1048. PubMed PMID: 22535769; PMCID: PMC3380307.
18. Kumar N, Robidoux J, Daniel KW, Guzman G, Floering LM, Collins S. Requirement of vimentin filament assembly for beta3-adrenergic receptor activation of ERK MAP kinase and lipolysis. J Biol Chem. 2007;282(12):9244-50. Epub 2007/01/26. doi: 10.1074/jbc.M605571200. PubMed PMID: 17251187.
19. Cogne B, Bouameur JE, Hayot G, Latypova X, Pattabiraman S, Caillaud A, Si-Tayeb K, Besnard T, Kury S, Chariau C, Gaignerie A, David L, Bordure P, Kaganovich D, Bezieau S, Golzio C, Magin TM, Isidor B. A dominant vimentin variant causes a rare syndrome with premature aging. Eur J Hum Genet. 2020;28(9):1218-30. Epub 2020/02/19. doi: 10.1038/s41431-020-0583-2. PubMed PMID: 32066935; PMCID: PMC7609319.
20. Eriksson JE. Harmful vimentin manifests itself as multiorgan failure. Eur J Hum Genet. 2020;28(9):1139-40. Epub 2020/07/15. doi: 10.1038/s41431-020-0684-y. PubMed PMID: 32661328; PMCID: PMC7608120.
21. Haversen L, Sundelin JP, Mardinoglu A, Rutberg M, Stahlman M, Wilhelmsson U, Hulten LM, Pekny M, Fogelstrand P, Bentzon JF, Levin M, Boren J. Vimentin deficiency in macrophages induces increased oxidative stress and vascular inflammation but attenuates atherosclerosis in mice. Sci Rep. 2018;8(1):16973. Epub 2018/11/20. doi: 10.1038/s41598-018-34659-2. PubMed PMID: 30451917; PMCID: PMC6242955.
22. Terzi F, Henrion D, Colucci-Guyon E, Federici P, Babinet C, Levy BI, Briand P, Friedlander G. Reduction of renal mass is lethal in mice lacking vimentin. Role of endothelin-nitric oxide imbalance. J Clin Invest. 1997;100(6):1520-8. Epub 1997/09/18. doi: 10.1172/JCI119675. PubMed PMID: 9294120; PMCID: PMC508333.
23. Runembert I, Queffeulou G, Federici P, Vrtovsnik F, Colucci-Guyon E, Babinet C, Briand P, Trugnan G, Friedlander G, Terzi F. Vimentin affects localization and activity of sodium-glucose cotransporter SGLT1 in membrane rafts. J Cell Sci. 2002;115(Pt 4):713-24. Epub 2002/02/28. doi: 10.1242/jcs.115.4.713. PubMed PMID: 11865027.
24. Hol EM, Pekny M. Glial fibrillary acidic protein (GFAP) and the astrocyte intermediate filament system in diseases of the central nervous system. Curr Opin Cell Biol. 2015;32:121-30. Epub 2015/03/03. doi: 10.1016/j.ceb.2015.02.004. PubMed PMID: 25726916.
25. Wilhelmsson U, Li L, Pekna M, Berthold CH, Blom S, Eliasson C, Renner O, Bushong E, Ellisman M, Morgan TE, Pekny M. Absence of glial fibrillary acidic protein and vimentin prevents hypertrophy of astrocytic processes and improves post-traumatic regeneration. J Neurosci. 2004;24(21):5016-21. Epub 2004/05/28. doi: 10.1523/JNEUROSCI.0820-04.2004. PubMed PMID: 15163694; PMCID: PMC6729371.
26. Lepekhin EA, Eliasson C, Berthold CH, Berezin V, Bock E, Pekny M. Intermediate filaments regulate astrocyte motility. J Neurochem. 2001;79(3):617-25. Epub 2001/11/10. doi: 10.1046/j.1471-4159.2001.00595.x. PubMed PMID: 11701765.

27. Perlson E, Hanz S, Ben-Yaakov K, Segal-Ruder Y, Seger R, Fainzilber M. Vimentin-dependent spatial translocation of an activated MAP kinase in injured nerve. Neuron. 2005;45(5):715-26. Epub 2005/03/08. doi: 10.1016/j.neuron.2005.01.023. PubMed PMID: 15748847.
28. Eliasson C, Sahlgren C, Berthold CH, Stakeberg J, Celis JE, Betsholtz C, Eriksson JE, Pekny M. Intermediate filament protein partnership in astrocytes. J Biol Chem. 1999;274(34):23996-4006. Epub 1999/08/14. doi: 10.1074/jbc.274.34.23996. PubMed PMID: 10446168.
29. Pekny M, Johansson CB, Eliasson C, Stakeberg J, Wallen A, Perlmann T, Lendahl U, Betsholtz C, Berthold CH, Frisen J. Abnormal reaction to central nervous system injury in mice lacking glial fibrillary acidic protein and vimentin. J Cell Biol. 1999;145(3):503-14. Epub 1999/05/04. doi: 10.1083/jcb.145.3.503. PubMed PMID: 10225952; PMCID: PMC2185074.
30. Lundkvist A, Reichenbach A, Betsholtz C, Carmeliet P, Wolburg H, Pekny M. Under stress, the absence of intermediate filaments from Muller cells in the retina has structural and functional consequences. J Cell Sci. 2004;117(Pt 16):3481-8. Epub 2004/07/01. doi: 10.1242/jcs.01221. PubMed PMID: 15226376.
31. Verardo MR, Lewis GP, Takeda M, Linberg KA, Byun J, Luna G, Wilhelmsson U, Pekny M, Chen DF, Fisher SK. Abnormal reactivity of muller cells after retinal detachment in mice deficient in GFAP and vimentin. Invest Ophthalmol Vis Sci. 2008;49(8):3659-65. Epub 2008/05/13. doi: 10.1167/iovs.07-1474. PubMed PMID: 18469190; PMCID: PMC2650509.
32. Ding M, Eliasson C, Betsholtz C, Hamberger A, Pekny M. Altered taurine release following hypotonic stress in astrocytes from mice deficient for GFAP and vimentin. Brain Res Mol Brain Res. 1998;62(1):77-81. Epub 1998/10/31. doi: 10.1016/s0169-328x(98)00240-x. PubMed PMID: 9795147.
33. Li L, Lundkvist A, Andersson D, Wilhelmsson U, Nagai N, Pardo AC, Nodin C, Stahlberg A, Aprico K, Larsson K, Yabe T, Moons L, Fotheringham A, Davies I, Carmeliet P, Schwartz JP, Pekna M, Kubista M, Blomstrand F, Maragakis N, Nilsson M, Pekny M. Protective role of reactive astrocytes in brain ischemia. J Cereb Blood Flow Metab. 2008;28(3):468-81. Epub 2007/08/30. doi: 10.1038/sj.jcbfm.9600546. PubMed PMID: 17726492.
34. de Pablo Y, Nilsson M, Pekna M, Pekny M. Intermediate filaments are important for astrocyte response to oxidative stress induced by oxygen-glucose deprivation and reperfusion. Histochem Cell Biol. 2013;140(1):81-91. Epub 2013/06/13. doi: 10.1007/s00418-013-1110-0. PubMed PMID: 23756782.
35. Wunderlich KA, Tanimoto N, Grosche A, Zrenner E, Pekny M, Reichenbach A, Seeliger MW, Pannicke T, Perez MT. Retinal functional alterations in mice lacking intermediate filament proteins glial fibrillary acidic protein and vimentin. FASEB J. 2015;29(12):4815-28. Epub 2015/08/08. doi: 10.1096/fj.15-272963. PubMed PMID: 26251181.
36. Lebkuechner I, Wilhelmsson U, Mollerstrom E, Pekna M, Pekny M. Heterogeneity of Notch signaling in astrocytes and the effects of GFAP and vimentin deficiency. J Neurochem. 2015;135(2):234-48. Epub 2015/06/30. doi: 10.1111/jnc.13213. PubMed PMID: 26118771.
37. Wilhelmsson U, Faiz M, de Pablo Y, Sjoqvist M, Andersson D, Widestrand A, Potokar M, Stenovec M, Smith PL, Shinjyo N, Pekny T, Zorec R, Stahlberg A, Pekna M, Sahlgren C, Pekny M. Astrocytes negatively regulate neurogenesis through the Jagged1-mediated Notch pathway. Stem Cells. 2012;30(10):2320-9. Epub 2012/08/14. doi: 10.1002/stem.1196. PubMed PMID: 22887872.

38. Pekny M, Eliasson C, Siushansian R, Ding M, Dixon SJ, Pekna M, Wilson JX, Hamberger A. The impact of genetic removal of GFAP and/or vimentin on glutamine levels and transport of glucose and ascorbate in astrocytes. Neurochem Res. 1999;24(11):1357-62. Epub 1999/11/11. doi: 10.1023/a:1022572304626. PubMed PMID: 10555775.
39. Macauley SL, Pekny M, Sands MS. The role of attenuated astrocyte activation in infantile neuronal ceroid lipofuscinosis. J Neurosci. 2011;31(43):15575-85. Epub 2011/10/28. doi: 10.1523/JNEUROSCI.3579-11.2011. PubMed PMID: 22031903; PMCID: PMC3218425.
40. Kraft AW, Hu X, Yoon H, Yan P, Xiao Q, Wang Y, Gil SC, Brown J, Wilhelmsson U, Restivo JL, Cirrito JR, Holtzman DM, Kim J, Pekny M, Lee JM. Attenuating astrocyte activation accelerates plaque pathogenesis in APP/PS1 mice. FASEB J. 2013;27(1):187-98. Epub 2012/10/06. doi: 10.1096/fj.12-208660. PubMed PMID: 23038755; PMCID: PMC3528309.
41. Kamphuis W, Kooijman L, Orre M, Stassen O, Pekny M, Hol EM. GFAP and vimentin deficiency alters gene expression in astrocytes and microglia in wild-type mice and changes the transcriptional response of reactive glia in mouse model for Alzheimer's disease. Glia. 2015;63(6):1036-56. Epub 2015/03/04. doi: 10.1002/glia.22800. PubMed PMID: 25731615.
42. Larsson A, Wilhelmsson U, Pekna M, Pekny M. Increased cell proliferation and neurogenesis in the hippocampal dentate gyrus of old GFAP(-/-)Vim(-/-) mice. Neurochem Res. 2004;29(11):2069-73. Epub 2005/01/25. doi: 10.1007/s11064-004-6880-2. PubMed PMID: 15662841.
43. Menet V, Prieto M, Privat A, Gimenez y Ribotta M. Axonal plasticity and functional recovery after spinal cord injury in mice deficient in both glial fibrillary acidic protein and vimentin genes. Proc Natl Acad Sci U S A. 2003;100(15):8999-9004. Epub 2003/07/16. doi: 10.1073/pnas.1533187100. PubMed PMID: 12861073; PMCID: PMC166427.
44. Cho KS, Yang L, Lu B, Feng Ma H, Huang X, Pekny M, Chen DF. Re-establishing the regenerative potential of central nervous system axons in postnatal mice. J Cell Sci. 2005;118(Pt 5):863-72. Epub 2005/02/26. doi: 10.1242/jcs.01658. PubMed PMID: 15731004; PMCID: PMC1351228.
45. Eckes B, Colucci-Guyon E, Smola H, Nodder S, Babinet C, Krieg T, Martin P. Impaired wound healing in embryonic and adult mice lacking vimentin. J Cell Sci. 2000;113 (Pt 13):2455-62. Epub 2000/06/15. doi: 10.1242/jcs.113.13.2455. PubMed PMID: 10852824.
46. Cheng F, Shen Y, Mohanasundaram P, Lindstrom M, Ivaska J, Ny T, Eriksson JE. Vimentin coordinates fibroblast proliferation and keratinocyte differentiation in wound healing via TGF-beta-Slug signaling. Proc Natl Acad Sci U S A. 2016;113(30):E4320-7. doi: 10.1073/pnas.1519197113. PubMed PMID: 27466403; PMCID: PMC4968728.
47. Eckes B, Dogic D, Colucci-Guyon E, Wang N, Maniotis A, Ingber D, Merckling A, Langa F, Aumailley M, Delouvee A, Koteliansky V, Babinet C, Krieg T. Impaired mechanical stability, migration and contractile capacity in vimentin-deficient fibroblasts. J Cell Sci. 1998;111 (Pt 13):1897-907. PubMed PMID: 9625752.
48. Jiu Y, Lehtimaki J, Tojkander S, Cheng F, Jaalinoja H, Liu X, Varjosalo M, Eriksson JE, Lappalainen P. Bidirectional Interplay between Vimentin Intermediate Filaments and Contractile Actin Stress Fibers. Cell Rep. 2015;11(10):1511-8. Epub 2015/06/02. doi: 10.1016/j.celrep.2015.05.008. PubMed PMID: 26027931.
49. Costigliola N, Ding L, Burckhardt CJ, Han SJ, Gutierrez E, Mota A, Groisman A, Mitchison TJ, Danuser G. Vimentin fibers orient traction stress. Proc Natl Acad Sci U S A. 2017;114(20):5195-200. Epub 2017/05/04. doi: 10.1073/pnas.1614610114. PubMed PMID: 28465431; PMCID: PMC5441818.

50. Jiu Y, Peranen J, Schaible N, Cheng F, Eriksson JE, Krishnan R, Lappalainen P. Vimentin intermediate filaments control actin stress fiber assembly through GEF-H1 and RhoA. J Cell Sci. 2017;130(5):892-902. Epub 2017/01/18. doi: 10.1242/jcs.196881. PubMed PMID: 28096473; PMCID: PMC5358333.
51. dos Santos G, Rogel MR, Baker MA, Troken JR, Urich D, Morales-Nebreda L, Sennello JA, Kutuzov MA, Sitikov A, Davis JM, Lam AP, Cheresh P, Kamp D, Shumaker DK, Budinger GR, Ridge KM. Vimentin regulates activation of the NLRP3 inflammasome. Nat Commun. 2015;6:6574. doi: 10.1038/ncomms7574. PubMed PMID: 25762200; PMCID: PMC4358756.
52. Kim KK, Kugler MC, Wolters PJ, Robillard L, Galvez MG, Brumwell AN, Sheppard D, Chapman HA. Alveolar epithelial cell mesenchymal transition develops in vivo during pulmonary fibrosis and is regulated by the extracellular matrix. Proc Natl Acad Sci U S A. 2006;103(35):13180-5. Epub 2006/08/23. doi: 10.1073/pnas.0605669103. PubMed PMID: 16924102; PMCID: PMC1551904.
53. Marmai C, Sutherland RE, Kim KK, Dolganov GM, Fang X, Kim SS, Jiang S, Golden JA, Hoopes CW, Matthay MA, Chapman HA, Wolters PJ. Alveolar epithelial cells express mesenchymal proteins in patients with idiopathic pulmonary fibrosis. Am J Physiol Lung Cell Mol Physiol. 2011;301(1):L71-8. Epub 2011/04/19. doi: 10.1152/ajplung.00212.2010. PubMed PMID: 21498628; PMCID: PMC3129898.
54. Rogel MR, Soni PN, Troken JR, Sitikov A, Trejo HE, Ridge KM. Vimentin is sufficient and required for wound repair and remodeling in alveolar epithelial cells. FASEB J. 2011;25(11):3873-83. doi: 10.1096/fj.10-170795. PubMed PMID: 21803859; PMCID: PMC3205840.
55. Wang Z, Divanyan A, Jourd'heuil FL, Goldman RD, Ridge KM, Jourd'heuil D, Lopez-Soler RI. Vimentin expression is required for the development of EMT-related renal fibrosis following unilateral ureteral obstruction in mice. Am J Physiol Renal Physiol. 2018;315(4):F769-F80. Epub 2018/04/11. doi: 10.1152/ajprenal.00340.2017. PubMed PMID: 29631355; PMCID: PMC6335003.
56. Challa AA, Stefanovic B. A novel role of vimentin filaments: binding and stabilization of collagen mRNAs. Mol Cell Biol. 2011;31(18):3773-89. doi: 10.1128/MCB.05263-11. PubMed PMID: 21746880; PMCID: PMC3165730.
57. Nieminen M, Henttinen T, Merinen M, Marttila-Ichihara F, Eriksson JE, Jalkanen S. Vimentin function in lymphocyte adhesion and transcellular migration. Nat Cell Biol. 2006;8(2):156-62. Epub 2006/01/24. doi: 10.1038/ncb1355. PubMed PMID: 16429129.
58. Brown MJ, Hallam JA, Colucci-Guyon E, Shaw S. Rigidity of circulating lymphocytes is primarily conferred by vimentin intermediate filaments. J Immunol. 2001;166(11):6640-6. Epub 2001/05/22. doi: 10.4049/jimmunol.166.11.6640. PubMed PMID: 11359818.
59. Barberis L, Pasquali C, Bertschy-Meier D, Cuccurullo A, Costa C, Ambrogio C, Vilbois F, Chiarle R, Wymann M, Altruda F, Rommel C, Hirsch E. Leukocyte transmigration is modulated by chemokine-mediated PI3Kgamma-dependent phosphorylation of vimentin. Eur J Immunol. 2009;39(4):1136-46. Epub 2009/03/18. doi: 10.1002/eji.200838884. PubMed PMID: 19291697.
60. Calle Y, Carragher NO, Thrasher AJ, Jones GE. Inhibition of calpain stabilises podosomes and impairs dendritic cell motility. J Cell Sci. 2006;119(Pt 11):2375-85. Epub 2006/05/26. doi: 10.1242/jcs.02939. PubMed PMID: 16723743.
61. Correia I, Chu D, Chou YH, Goldman RD, Matsudaira P. Integrating the actin and vimentin cytoskeletons. adhesion-dependent formation of fimbrin-vimentin complexes in macrophages. J

Cell Biol. 1999;146(4):831-42. Epub 1999/08/25. doi: 10.1083/jcb.146.4.831. PubMed PMID: 10459017; PMCID: PMC2156141.
62. Kolb M, Margetts PJ, Anthony DC, Pitossi F, Gauldie J. Transient expression of IL-1beta induces acute lung injury and chronic repair leading to pulmonary fibrosis. J Clin Invest. 2001;107(12):1529-36. Epub 2001/06/20. doi: 10.1172/JCI12568. PubMed PMID: 11413160; PMCID: PMC200196.
63. Lang T, Lee JPW, Elgass K, Pinar AA, Tate MD, Aitken EH, Fan H, Creed SJ, Deen NS, Traore DAK, Mueller I, Stanisic D, Baiwog FS, Skene C, Wilce MCJ, Mansell A, Morand EF, Harris J. Macrophage migration inhibitory factor is required for NLRP3 inflammasome activation. Nat Commun. 2018;9(1):2223. Epub 2018/06/10. doi: 10.1038/s41467-018-04581-2. PubMed PMID: 29884801; PMCID: PMC5993818.
64. Mohammad I, Nousiainen K, Bhosale SD, Starskaia I, Moulder R, Rokka A, Cheng F, Mohanasundaram P, Eriksson JE, Goodlett DR, Lahdesmaki H, Chen Z. Quantitative proteomic characterization and comparison of T helper 17 and induced regulatory T cells. PLoS Biol. 2018;16(5):e2004194. Epub 2018/06/01. doi: 10.1371/journal.pbio.2004194. PubMed PMID: 29851958; PMCID: PMC5979006.
65. McDonald-Hyman C, Muller JT, Loschi M, Thangavelu G, Saha A, Kumari S, Reichenbach DK, Smith MJ, Zhang G, Koehn BH, Lin J, Mitchell JS, Fife BT, Panoskaltsis-Mortari A, Feser CJ, Kirchmeier AK, Osborn MJ, Hippen KL, Kelekar A, Serody JS, Turka LA, Munn DH, Chi H, Neubert TA, Dustin ML, Blazar BR. The vimentin intermediate filament network restrains regulatory T cell suppression of graft-versus-host disease. J Clin Invest. 2018;128(10):4604-21. doi: 10.1172/JCI95713. PubMed PMID: 30106752; PMCID: PMC6159973.
66. Mor-Vaknin N, Legendre M, Yu Y, Serezani CH, Garg SK, Jatzek A, Swanson MD, Gonzalez-Hernandez MJ, Teitz-Tennenbaum S, Punturieri A, Engleberg NC, Banerjee R, Peters-Golden M, Kao JY, Markovitz DM. Murine colitis is mediated by vimentin. Sci Rep. 2013;3:1045. Epub 2013/01/11. doi: 10.1038/srep01045. PubMed PMID: 23304436; PMCID: PMC3540396.
67. Antfolk D, Sjoqvist M, Cheng F, Isoniemi K, Duran CL, Rivero-Muller A, Antila C, Niemi R, Landor S, Bouten CVC, Bayless KJ, Eriksson JE, Sahlgren CM. Selective regulation of Notch ligands during angiogenesis is mediated by vimentin. Proc Natl Acad Sci U S A. 2017;114(23):E4574-E81. Epub 2017/05/24. doi: 10.1073/pnas.1703057114. PubMed PMID: 28533359; PMCID: PMC5468602.
68. Boraas LC, Ahsan T. Lack of vimentin impairs endothelial differentiation of embryonic stem cells. Sci Rep. 2016;6:30814. Epub 2016/08/03. doi: 10.1038/srep30814. PubMed PMID: 27480130; PMCID: PMC4969593.
69. van Engeland NCA, Suarez Rodriguez F, Rivero-Muller A, Ristori T, Duran CL, Stassen O, Antfolk D, Driessen RCH, Ruohonen S, Ruohonen ST, Nuutinen S, Savontaus E, Loerakker S, Bayless KJ, Sjoqvist M, Bouten CVC, Eriksson JE, Sahlgren CM. Vimentin regulates Notch signaling strength and arterial remodeling in response to hemodynamic stress. Sci Rep. 2019;9(1):12415. Epub 2019/08/29. doi: 10.1038/s41598-019-48218-w. PubMed PMID: 31455807; PMCID: PMC6712036.
70. Gregor M, Osmanagic-Myers S, Burgstaller G, Wolfram M, Fischer I, Walko G, Resch GP, Jorgl A, Herrmann H, Wiche G. Mechanosensing through focal adhesion-anchored intermediate filaments. FASEB J. 2014;28(2):715-29. Epub 2013/12/19. doi: 10.1096/fj.13-231829. PubMed PMID: 24347609.

71. Shen Y, Wu H, Lu PJ, Wang D, Shayegan M, Li H, Shi W, Wang Z, Cai LH, Xia J, Zhang M, Ding R, Herrmann H, Goldman R, MacKintosh FC, Moncho-Jorda A, Weitz DA. Effects of Vimentin Intermediate Filaments on the Structure and Dynamics of In Vitro Multicomponent Interpenetrating Cytoskeletal Networks. Phys Rev Lett. 2021;127(10):108101. Epub 2021/09/18. doi: 10.1103/PhysRevLett.127.108101. PubMed PMID: 34533352.
72. Helmke BP, Goldman RD, Davies PF. Rapid displacement of vimentin intermediate filaments in living endothelial cells exposed to flow. Circ Res. 2000;86(7):745-52. Epub 2000/04/14. doi: 10.1161/01.res.86.7.745. PubMed PMID: 10764407.
73. Janmey PA, Euteneuer U, Traub P, Schliwa M. Viscoelastic properties of vimentin compared with other filamentous biopolymer networks. J Cell Biol. 1991;113(1):155-60. PubMed PMID: 2007620; PMCID: PMC2288924.
74. Koster S, Weitz DA, Goldman RD, Aebi U, Herrmann H. Intermediate filament mechanics in vitro and in the cell: from coiled coils to filaments, fibers and networks. Curr Opin Cell Biol. 2015;32:82-91. Epub 2015/01/27. doi: 10.1016/j.ceb.2015.01.001. PubMed PMID: 25621895; PMCID: PMC4355244.
75. Guzman C, Jeney S, Kreplak L, Kasas S, Kulik AJ, Aebi U, Forro L. Exploring the mechanical properties of single vimentin intermediate filaments by atomic force microscopy. J Mol Biol. 2006;360(3):623-30. Epub 2006/06/13. doi: 10.1016/j.jmb.2006.05.030. PubMed PMID: 16765985.
76. Rathje LS, Nordgren N, Pettersson T, Ronnlund D, Widengren J, Aspenstrom P, Gad AK. Oncogenes induce a vimentin filament collapse mediated by HDAC6 that is linked to cell stiffness. Proc Natl Acad Sci U S A. 2014;111(4):1515-20. Epub 2014/01/30. doi: 10.1073/pnas.1300238111. PubMed PMID: 24474778; PMCID: PMC3910606.
77. Mendez MG, Kojima S, Goldman RD. Vimentin induces changes in cell shape, motility, and adhesion during the epithelial to mesenchymal transition. FASEB J. 2010;24(6):1838-51. Epub 2010/01/26. doi: 10.1096/fj.09-151639. PubMed PMID: 20097873; PMCID: PMC2874471.
78. Zhu QS, Rosenblatt K, Huang KL, Lahat G, Brobey R, Bolshakov S, Nguyen T, Ding Z, Belousov R, Bill K, Luo X, Lazar A, Dicker A, Mills GB, Hung MC, Lev D. Vimentin is a novel AKT1 target mediating motility and invasion. Oncogene. 2011;30(4):457-70. Epub 2010/09/22. doi: 10.1038/onc.2010.421. PubMed PMID: 20856200; PMCID: PMC3010301.
79. Vahabikashi A, Park CY, Perkumas K, Zhang Z, Deurloo EK, Wu H, Weitz DA, Stamer WD, Goldman RD, Fredberg JJ, Johnson M. Probe Sensitivity to Cortical versus Intracellular Cytoskeletal Network Stiffness. Biophys J. 2019;116(3):518-29. Epub 2019/01/28. doi: 10.1016/j.bpj.2018.12.021. PubMed PMID: 30685055; PMCID: PMC6369565.
80. Siegel RL, Miller KD, Jemal A. Cancer statistics, 2019. CA Cancer J Clin. 2019;69(1):7-34. Epub 2019/01/09. doi: 10.3322/caac.21551. PubMed PMID: 30620402.
81. Dauphin M, Barbe C, Lemaire S, Nawrocki-Raby B, Lagonotte E, Delepine G, Birembaut P, Gilles C, Polette M. Vimentin expression predicts the occurrence of metastases in non small cell lung carcinomas. Lung Cancer. 2013;81(1):117-22. Epub 2013/04/09. doi: 10.1016/j.lungcan.2013.03.011. PubMed PMID: 23562674.
82. Burch TC, Watson MT, Nyalwidhe JO. Variable metastatic potentials correlate with differential plectin and vimentin expression in syngeneic androgen independent prostate cancer cells. PLoS One. 2013;8(5):e65005. doi: 10.1371/journal.pone.0065005. PubMed PMID: 23717685; PMCID: PMC3661497.
83. Domagala W, Lasota J, Dukowicz A, Markiewski M, Striker G, Weber K, Osborn M. Vimentin expression appears to be associated with poor prognosis in node-negative ductal NOS

breast carcinomas. Am J Pathol. 1990;137(6):1299-304. PubMed PMID: 1701960; PMCID: PMC1877729.
84. Kidd ME, Shumaker DK, Ridge KM. The role of vimentin intermediate filaments in the progression of lung cancer. Am J Respir Cell Mol Biol. 2014;50(1):1-6. Epub 2013/08/29. doi: 10.1165/rcmb.2013-0314TR. PubMed PMID: 23980547; PMCID: PMC3930939.
85. Dongre A, Weinberg RA. New insights into the mechanisms of epithelial-mesenchymal transition and implications for cancer. Nat Rev Mol Cell Biol. 2019;20(2):69-84. Epub 2018/11/22. doi: 10.1038/s41580-018-0080-4. PubMed PMID: 30459476.
86. Virtakoivu R, Mai A, Mattila E, De Franceschi N, Imanishi SY, Corthals G, Kaukonen R, Saari M, Cheng F, Torvaldson E, Kosma VM, Mannermaa A, Muharram G, Gilles C, Eriksson J, Soini Y, Lorens JB, Ivaska J. Vimentin-ERK Signaling Uncouples Slug Gene Regulatory Function. Cancer Res. 2015;75(11):2349-62. Epub 2015/04/10. doi: 10.1158/0008-5472.CAN-14-2842. PubMed PMID: 25855378.
87. Francart ME, Vanwynsberghe AM, Lambert J, Bourcy M, Genna A, Ancel J, Perez-Boza J, Noel A, Birembaut P, Struman I, Polette M, Gilles C. Vimentin prevents a miR-dependent negative regulation of tissue factor mRNA during epithelial-mesenchymal transitions and facilitates early metastasis. Oncogene. 2020;39(18):3680-92. Epub 2020/03/11. doi: 10.1038/s41388-020-1244-1. PubMed PMID: 32152404; PMCID: PMC7190572.
88. Meng J, Chen S, Han JX, Qian B, Wang XR, Zhong WL, Qin Y, Zhang H, Gao WF, Lei YY, Yang W, Yang L, Zhang C, Liu HJ, Liu YR, Zhou HG, Sun T, Yang C. Twist1 Regulates Vimentin through Cul2 Circular RNA to Promote EMT in Hepatocellular Carcinoma. Cancer Res. 2018;78(15):4150-62. Epub 2018/05/31. doi: 10.1158/0008-5472.CAN-17-3009. PubMed PMID: 29844124.
89. Schoumacher M, Goldman RD, Louvard D, Vignjevic DM. Actin, microtubules, and vimentin intermediate filaments cooperate for elongation of invadopodia. J Cell Biol. 2010;189(3):541-56. Epub 2010/04/28. doi: 10.1083/jcb.200909113. PubMed PMID: 20421424; PMCID: PMC2867303.
90. Hendrix MJ, Seftor EA, Seftor RE, Trevor KT. Experimental co-expression of vimentin and keratin intermediate filaments in human breast cancer cells results in phenotypic interconversion and increased invasive behavior. Am J Pathol. 1997;150(2):483-95. Epub 1997/02/01. PubMed PMID: 9033265; PMCID: PMC1858294.
91. Gilles C, Polette M, Zahm JM, Tournier JM, Volders L, Foidart JM, Birembaut P. Vimentin contributes to human mammary epithelial cell migration. J Cell Sci. 1999;112 (Pt 24):4615-25. Epub 1999/11/27. PubMed PMID: 10574710.
92. Messica Y, Laser-Azogui A, Volberg T, Elisha Y, Lysakovskaia K, Eils R, Gladilin E, Geiger B, Beck R. The role of Vimentin in Regulating Cell Invasive Migration in Dense Cultures of Breast Carcinoma Cells. Nano Lett. 2017;17(11):6941-8. doi: 10.1021/acs.nanolett.7b03358. PubMed PMID: 29022351.
93. Wang W, Yi M, Zhang R, Li J, Chen S, Cai J, Zeng Z, Li X, Xiong W, Wang L, Li G, Xiang B. Vimentin is a crucial target for anti-metastasis therapy of nasopharyngeal carcinoma. Mol Cell Biochem. 2018;438(1-2):47-57. Epub 2017/07/27. doi: 10.1007/s11010-017-3112-z. PubMed PMID: 28744809.
94. Chan SH, Tsai JP, Shen CJ, Liao YH, Chen BK. Oleate-induced PTX3 promotes head and neck squamous cell carcinoma metastasis through the up-regulation of vimentin. Oncotarget. 2017;8(25):41364-78. Epub 2017/05/11. doi: 10.18632/oncotarget.17326. PubMed PMID: 28489600; PMCID: PMC5522334.

95. Liu S, Liu L, Ye W, Ye D, Wang T, Guo W, Liao Y, Xu D, Song H, Zhang L, Zhu H, Deng J, Zhang Z. High Vimentin Expression Associated with Lymph Node Metastasis and Predicated a Poor Prognosis in Oral Squamous Cell Carcinoma. Sci Rep. 2016;6:38834. Epub 2016/12/15. doi: 10.1038/srep38834. PubMed PMID: 27966589; PMCID: PMC5155220.
96. Zelenko Z, Gallagher EJ, Tobin-Hess A, Belardi V, Rostoker R, Blank J, Dina Y, LeRoith D. Silencing vimentin expression decreases pulmonary metastases in a pre-diabetic mouse model of mammary tumor progression. Oncogene. 2017;36(10):1394-403. Epub 2016/08/30. doi: 10.1038/onc.2016.305. PubMed PMID: 27568979; PMCID: PMC5332535.
97. Yang CY, Chang PW, Hsu WH, Chang HC, Chen CL, Lai CC, Chiu WT, Chen HC. Src and SHP2 coordinately regulate the dynamics and organization of vimentin filaments during cell migration. Oncogene. 2019;38(21):4075-94. Epub 2019/01/31. doi: 10.1038/s41388-019-0705-x. PubMed PMID: 30696956; PMCID: PMC6755999.
98. Tang D, Chen X, Kang R, Kroemer G. Ferroptosis: molecular mechanisms and health implications. Cell Res. 2021;31(2):107-25. Epub 2020/12/04. doi: 10.1038/s41422-020-00441-1. PubMed PMID: 33268902; PMCID: PMC8026611.
99. Hu K, Li K, Lv J, Feng J, Chen J, Wu H, Cheng F, Jiang W, Wang J, Pei H, Chiao PJ, Cai Z, Chen Y, Liu M, Pang X. Suppression of the SLC7A11/glutathione axis causes synthetic lethality in KRAS-mutant lung adenocarcinoma. J Clin Invest. 2020;130(4):1752-66. Epub 2019/12/25. doi: 10.1172/JCI124049. PubMed PMID: 31874110; PMCID: PMC7108883.
100. Ni J, Chen K, Zhang J, Zhang X. Inhibition of GPX4 or mTOR overcomes resistance to Lapatinib via promoting ferroptosis in NSCLC cells. Biochem Biophys Res Commun. 2021;567:154-60. Epub 2021/06/23. doi: 10.1016/j.bbrc.2021.06.051. PubMed PMID: 34157442.
101. DuPage M, Dooley AL, Jacks T. Conditional mouse lung cancer models using adenoviral or lentiviral delivery of Cre recombinase. Nat Protoc. 2009;4(7):1064-72. Epub 2009/06/30. doi: 10.1038/nprot.2009.95. PubMed PMID: 19561589; PMCID: PMC2757265.
102. Shajani-Yi Z, de Abreu FB, Peterson JD, Tsongalis GJ. Frequency of Somatic TP53 Mutations in Combination with Known Pathogenic Mutations in Colon Adenocarcinoma, Non-Small Cell Lung Carcinoma, and Gliomas as Identified by Next-Generation Sequencing. Neoplasia. 2018;20(3):256-62. Epub 2018/02/18. doi: 10.1016/j.neo.2017.12.005. PubMed PMID: 29454261; PMCID: PMC5849803.
103. Scoccianti C, Vesin A, Martel G, Olivier M, Brambilla E, Timsit JF, Tavecchio L, Brambilla C, Field JK, Hainaut P, European Early Lung Cancer C. Prognostic value of TP53, KRAS and EGFR mutations in nonsmall cell lung cancer: the EUELC cohort. Eur Respir J. 2012;40(1):177-84. Epub 2012/01/24. doi: 10.1183/09031936.00097311. PubMed PMID: 22267755.
104. Cox AD, Fesik SW, Kimmelman AC, Luo J, Der CJ. Drugging the undruggable RAS: Mission possible? Nat Rev Drug Discov. 2014;13(11):828-51. Epub 2014/10/18. doi: 10.1038/nrd4389. PubMed PMID: 25323927; PMCID: PMC4355017.
105. Cancer Genome Atlas Research N. Comprehensive molecular profiling of lung adenocarcinoma. Nature. 2014;511(7511):543-50. Epub 2014/08/01. doi: 10.1038/nature13385. PubMed PMID: 25079552; PMCID: PMC4231481.
106. Jackson EL, Olive KP, Tuveson DA, Bronson R, Crowley D, Brown M, Jacks T. The differential effects of mutant p53 alleles on advanced murine lung cancer. Cancer Res. 2005;65(22):10280-8. Epub 2005/11/17. doi: 10.1158/0008-5472.CAN-05-2193. PubMed PMID: 16288016.

107. Soriano P. Generalized lacZ expression with the ROSA26 Cre reporter strain. Nat Genet. 1999;21(1):70-1. Epub 1999/01/23. doi: 10.1038/5007. PubMed PMID: 9916792.
108. Whithaus K, Fukuoka J, Prihoda TJ, Jagirdar J. Evaluation of napsin A, cytokeratin 5/6, p63, and thyroid transcription factor 1 in adenocarcinoma versus squamous cell carcinoma of the lung. Arch Pathol Lab Med. 2012;136(2):155-62. Epub 2012/02/01. doi: 10.5858/arpa.2011-0232-OA. PubMed PMID: 22288962.
109. Nagalingam A, Kuppusamy P, Singh SV, Sharma D, Saxena NK. Mechanistic elucidation of the antitumor properties of withaferin a in breast cancer. Cancer Res. 2014;74(9):2617-29. Epub 2014/04/16. doi: 10.1158/0008-5472.CAN-13-2081. PubMed PMID: 24732433; PMCID: PMC4009451.
110. Suman S, Das TP, Moselhy J, Pal D, Kolluru V, Alatassi H, Ankem MK, Damodaran C. Oral administration of withaferin A inhibits carcinogenesis of prostate in TRAMP model. Oncotarget. 2016;7(33):53751-61. Epub 2016/07/23. doi: 10.18632/oncotarget.10733. PubMed PMID: 27447565; PMCID: PMC5288218.
111. Kakar SS, Parte S, Carter K, Joshua IG, Worth C, Rameshwar P, Ratajczak MZ. Withaferin A (WFA) inhibits tumor growth and metastasis by targeting ovarian cancer stem cells. Oncotarget. 2017;8(43):74494-505. Epub 2017/11/02. doi: 10.18632/oncotarget.20170. PubMed PMID: 29088802; PMCID: PMC5650357.
112. Bargagna-Mohan P, Hamza A, Kim YE, Khuan Abby Ho Y, Mor-Vaknin N, Wendschlag N, Liu J, Evans RM, Markovitz DM, Zhan CG, Kim KB, Mohan R. The tumor inhibitor and antiangiogenic agent withaferin A targets the intermediate filament protein vimentin. Chem Biol. 2007;14(6):623-34. Epub 2007/06/23. doi: 10.1016/j.chembiol.2007.04.010. PubMed PMID: 17584610; PMCID: PMC3228641.
113. Bollong MJ, Pietila M, Pearson AD, Sarkar TR, Ahmad I, Soundararajan R, Lyssiotis CA, Mani SA, Schultz PG, Lairson LL. A vimentin binding small molecule leads to mitotic disruption in mesenchymal cancers. Proc Natl Acad Sci U S A. 2017;114(46):E9903-E12. Epub 2017/11/01. doi: 10.1073/pnas.1716009114. PubMed PMID: 29087350; PMCID: PMC5699095.
114. Thaiparambil JT, Bender L, Ganesh T, Kline E, Patel P, Liu Y, Tighiouart M, Vertino PM, Harvey RD, Garcia A, Marcus AI. Withaferin A inhibits breast cancer invasion and metastasis at sub-cytotoxic doses by inducing vimentin disassembly and serine 56 phosphorylation. Int J Cancer. 2011;129(11):2744-55. Epub 2011/05/04. doi: 10.1002/ijc.25938. PubMed PMID: 21538350.
115. Griffith OW. Mechanism of action, metabolism, and toxicity of buthionine sulfoximine and its higher homologs, potent inhibitors of glutathione synthesis. J Biol Chem. 1982;257(22):13704-12. Epub 1982/11/25. PubMed PMID: 6128339.
116. Doll S, Proneth B, Tyurina YY, Panzilius E, Kobayashi S, Ingold I, Irmler M, Beckers J, Aichler M, Walch A, Prokisch H, Trumbach D, Mao G, Qu F, Bayir H, Fullekrug J, Scheel CH, Wurst W, Schick JA, Kagan VE, Angeli JP, Conrad M. ACSL4 dictates ferroptosis sensitivity by shaping cellular lipid composition. Nat Chem Biol. 2017;13(1):91-8. Epub 2016/11/15. doi: 10.1038/nchembio.2239. PubMed PMID: 27842070; PMCID: PMC5610546.
117. Dixon SJ, Winter GE, Musavi LS, Lee ED, Snijder B, Rebsamen M, Superti-Furga G, Stockwell BR. Human Haploid Cell Genetics Reveals Roles for Lipid Metabolism Genes in Nonapoptotic Cell Death. ACS Chem Biol. 2015;10(7):1604-9. Epub 2015/05/13. doi: 10.1021/acschembio.5b00245. PubMed PMID: 25965523; PMCID: PMC4509420.
118. Yang WS, SriRamaratnam R, Welsch ME, Shimada K, Skouta R, Viswanathan VS, Cheah JH, Clemons PA, Shamji AF, Clish CB, Brown LM, Girotti AW, Cornish VW, Schreiber SL,

Stockwell BR. Regulation of ferroptotic cancer cell death by GPX4. Cell. 2014;156(1-2):317-31. Epub 2014/01/21. doi: 10.1016/j.cell.2013.12.010. PubMed PMID: 24439385; PMCID: PMC4076414.
119. Hassannia B, Wiernicki B, Ingold I, Qu F, Van Herck S, Tyurina YY, Bayir H, Abhari BA, Angeli JPF, Choi SM, Meul E, Heyninck K, Declerck K, Chirumamilla CS, Lahtela-Kakkonen M, Van Camp G, Krysko DV, Ekert PG, Fulda S, De Geest BG, Conrad M, Kagan VE, Vanden Berghe W, Vandenabeele P, Vanden Berghe T. Nano-targeted induction of dual ferroptotic mechanisms eradicates high-risk neuroblastoma. J Clin Invest. 2018;128(8):3341-55. Epub 2018/06/26. doi: 10.1172/JCI99032. PubMed PMID: 29939160; PMCID: PMC6063467.
120. Friedmann Angeli JP, Conrad M. Selenium and GPX4, a vital symbiosis. Free Radic Biol Med. 2018;127:153-9. Epub 2018/03/10. doi: 10.1016/j.freeradbiomed.2018.03.001. PubMed PMID: 29522794.
121. Gao M, Monian P, Quadri N, Ramasamy R, Jiang X. Glutaminolysis and Transferrin Regulate Ferroptosis. Mol Cell. 2015;59(2):298-308. Epub 2015/07/15. doi: 10.1016/j.molcel.2015.06.011. PubMed PMID: 26166707; PMCID: PMC4506736.
122. Yu Y, Jiang L, Wang H, Shen Z, Cheng Q, Zhang P, Wang J, Wu Q, Fang X, Duan L, Wang S, Wang K, An P, Shao T, Chung RT, Zheng S, Min J, Wang F. Hepatic transferrin plays a role in systemic iron homeostasis and liver ferroptosis. Blood. 2020;136(6):726-39. Epub 2020/05/07. doi: 10.1182/blood.2019002907. PubMed PMID: 32374849; PMCID: PMC7414596.
123. Yuan H, Li X, Zhang X, Kang R, Tang D. CISD1 inhibits ferroptosis by protection against mitochondrial lipid peroxidation. Biochem Biophys Res Commun. 2016;478(2):838-44. Epub 2016/08/12. doi: 10.1016/j.bbrc.2016.08.034. PubMed PMID: 27510639.
124. Wang Y, Liu Y, Liu J, Kang R, Tang D. NEDD4L-mediated LTF protein degradation limits ferroptosis. Biochem Biophys Res Commun. 2020;531(4):581-7. Epub 2020/08/20. doi: 10.1016/j.bbrc.2020.07.032. PubMed PMID: 32811647.
125. Romero R, Sayin VI, Davidson SM, Bauer MR, Singh SX, LeBoeuf SE, Karakousi TR, Ellis DC, Bhutkar A, Sanchez-Rivera FJ, Subbaraj L, Martinez B, Bronson RT, Prigge JR, Schmidt EE, Thomas CJ, Goparaju C, Davies A, Dolgalev I, Heguy A, Allaj V, Poirier JT, Moreira AL, Rudin CM, Pass HI, Vander Heiden MG, Jacks T, Papagiannakopoulos T. Keap1 loss promotes Kras-driven lung cancer and results in dependence on glutaminolysis. Nat Med. 2017;23(11):1362-8. Epub 2017/10/03. doi: 10.1038/nm.4407. PubMed PMID: 28967920; PMCID: PMC5677540.
126. Gibbons DL, Lin W, Creighton CJ, Rizvi ZH, Gregory PA, Goodall GJ, Thilaganathan N, Du L, Zhang Y, Pertsemlidis A, Kurie JM. Contextual extracellular cues promote tumor cell EMT and metastasis by regulating miR-200 family expression. Genes Dev. 2009;23(18):2140-51. Epub 2009/09/18. doi: 10.1101/gad.1820209. PubMed PMID: 19759262; PMCID: PMC2751985.
127. Thomas PA, Kirschmann DA, Cerhan JR, Folberg R, Seftor EA, Sellers TA, Hendrix MJ. Association between keratin and vimentin expression, malignant phenotype, and survival in postmenopausal breast cancer patients. Clin Cancer Res. 1999;5(10):2698-703. PubMed PMID: 10537332.
128. Peuhu E, Virtakoivu R, Mai A, Warri A, Ivaska J. Epithelial vimentin plays a functional role in mammary gland development. Development. 2017;144(22):4103-13. Epub 2017/09/28. doi: 10.1242/dev.154229. PubMed PMID: 28947532.
129. Bai Y, Meng L, Han L, Jia Y, Zhao Y, Gao H, Kang R, Wang X, Tang D, Dai E. Lipid storage and lipophagy regulates ferroptosis. Biochem Biophys Res Commun. 2019;508(4):997-1003. Epub 2018/12/14. doi: 10.1016/j.bbrc.2018.12.039. PubMed PMID: 30545638.

130. Kraft VAN, Bezjian CT, Pfeiffer S, Ringelstetter L, Muller C, Zandkarimi F, Merl-Pham J, Bao X, Anastasov N, Kossl J, Brandner S, Daniels JD, Schmitt-Kopplin P, Hauck SM, Stockwell BR, Hadian K, Schick JA. GTP Cyclohydrolase 1/Tetrahydrobiopterin Counteract Ferroptosis through Lipid Remodeling. ACS Cent Sci. 2020;6(1):41-53. Epub 2020/01/29. doi: 10.1021/acscentsci.9b01063. PubMed PMID: 31989025; PMCID: PMC6978838 equity in and consults with Inzen Therapeutics and is an inventor on patents and patent applications related to IKE and ferroptosis. J.A.S. holds patents related to ferroptosis. The other authors declare no competing interests.
131. Huang SH, Chi F, Peng L, Bo T, Zhang B, Liu LQ, Wu X, Mor-Vaknin N, Markovitz DM, Cao H, Zhou YH. Vimentin, a Novel NF-kappaB Regulator, Is Required for Meningitic Escherichia coli K1-Induced Pathogen Invasion and PMN Transmigration across the Blood-Brain Barrier. PLoS One. 2016;11(9):e0162641. Epub 2016/09/23. doi: 10.1371/journal.pone.0162641. PubMed PMID: 27657497; PMCID: PMC5033352.
132. Jiang SX, Slinn J, Aylsworth A, Hou ST. Vimentin participates in microglia activation and neurotoxicity in cerebral ischemia. J Neurochem. 2012;122(4):764-74. Epub 2012/06/12. doi: 10.1111/j.1471-4159.2012.07823.x. PubMed PMID: 22681613.
133. Surolia R, Li FJ, Wang Z, Li H, Dsouza K, Thomas V, Mirov S, Perez-Sala D, Athar M, Thannickal VJ, Antony VB. Vimentin intermediate filament assembly regulates fibroblast invasion in fibrogenic lung injury. JCI Insight. 2019;4(7). Epub 2019/04/05. doi: 10.1172/jci.insight.123253. PubMed PMID: 30944258; PMCID: PMC6483650.
134. Karki R, Kanneganti TD. Diverging inflammasome signals in tumorigenesis and potential targeting. Nat Rev Cancer. 2019;19(4):197-214. Epub 2019/03/08. doi: 10.1038/s41568-019-0123-y. PubMed PMID: 30842595; PMCID: PMC6953422.
135. Richardson AM, Havel LS, Koyen AE, Konen JM, Shupe J, Wiles WGt, Martin WD, Grossniklaus HE, Sica G, Gilbert-Ross M, Marcus AI. Vimentin Is Required for Lung Adenocarcinoma Metastasis via Heterotypic Tumor Cell-Cancer-Associated Fibroblast Interactions during Collective Invasion. Clin Cancer Res. 2018;24(2):420-32. doi: 10.1158/1078-0432.CCR-17-1776. PubMed PMID: 29208669; PMCID: PMC5771825.
136. Lanier MH, Kim T, Cooper JA. CARMIL2 is a novel molecular connection between vimentin and actin essential for cell migration and invadopodia formation. Mol Biol Cell. 2015;26(25):4577-88. Epub 2015/10/16. doi: 10.1091/mbc.E15-08-0552. PubMed PMID: 26466680; PMCID: PMC4678016.
137. Gan Z, Ding L, Burckhardt CJ, Lowery J, Zaritsky A, Sitterley K, Mota A, Costigliola N, Starker CG, Voytas DF, Tytell J, Goldman RD, Danuser G. Vimentin Intermediate Filaments Template Microtubule Networks to Enhance Persistence in Cell Polarity and Directed Migration. Cell Syst. 2016;3(3):252-63 e8. Epub 2016/09/27. doi: 10.1016/j.cels.2016.08.007. PubMed PMID: 27667364; PMCID: PMC5055390.
138. Al-Saad S, Al-Shibli K, Donnem T, Persson M, Bremnes RM, Busund LT. The prognostic impact of NF-kappaB p105, vimentin, E-cadherin and Par6 expression in epithelial and stromal compartment in non-small-cell lung cancer. Br J Cancer. 2008;99(9):1476-83. Epub 2008/10/16. doi: 10.1038/sj.bjc.6604713. PubMed PMID: 18854838; PMCID: PMC2579693.
139. Eden E, Lipson D, Yogev S, Yakhini Z. Discovering motifs in ranked lists of DNA sequences. PLoS Comput Biol. 2007;3(3):e39. Epub 2007/03/27. doi: 10.1371/journal.pcbi.0030039. PubMed PMID: 17381235; PMCID: PMC1829477.

140. Eden E, Navon R, Steinfeld I, Lipson D, Yakhini Z. GOrilla: a tool for discovery and visualization of enriched GO terms in ranked gene lists. BMC Bioinformatics. 2009;10:48. doi: 10.1186/1471-2105-10-48. PubMed PMID: 19192299; PMCID: PMC2644678.
141. Zhang L, Lee NJ, Nguyen AD, Enriquez RF, Riepler SJ, Stehrer B, Yulyaningsih E, Lin S, Shi YC, Baldock PA, Herzog H, Sainsbury A. Additive actions of the cannabinoid and neuropeptide Y systems on adiposity and lipid oxidation. Diabetes Obes Metab. 2010;12(7):591-603. Epub 2010/07/02. doi: 10.1111/j.1463-1326.2009.01193.x. PubMed PMID: 20590734.
142. Gilbert-Ross M, Konen J, Koo J, Shupe J, Robinson BS, Wiles WGt, Huang C, Martin WD, Behera M, Smith GH, Hill CE, Rossi MR, Sica GL, Rupji M, Chen Z, Kowalski J, Kasinski AL, Ramalingam SS, Fu H, Khuri FR, Zhou W, Marcus AI. Targeting adhesion signaling in KRAS, LKB1 mutant lung adenocarcinoma. JCI Insight. 2017;2(5):e90487. Epub 2017/03/16. doi: 10.1172/jci.insight.90487. PubMed PMID: 28289710; PMCID: PMC5333956 exists.
143. Chong J, Soufan O, Li C, Caraus I, Li S, Bourque G, Wishart DS, Xia J. MetaboAnalyst 4.0: towards more transparent and integrative metabolomics analysis. Nucleic Acids Res. 2018;46(W1):W486-W94. Epub 2018/05/16. doi: 10.1093/nar/gky310. PubMed PMID: 29762782; PMCID: PMC6030889.
144. Cruz MA, Chen J, Whitelock JL, Morales LD, Lopez JA. The platelet glycoprotein Ib-von Willebrand factor interaction activates the collagen receptor alpha2beta1 to bind collagen: activation-dependent conformational change of the alpha2-I domain. Blood. 2005;105(5):1986-91. Epub 2004/10/30. doi: 10.1182/blood-2004-04-1365. PubMed PMID: 15514009.
145. Plow EF, Haas TA, Zhang L, Loftus J, Smith JW. Ligand binding to integrins. J Biol Chem. 2000;275(29):21785-8. Epub 2000/05/10. doi: 10.1074/jbc.R000003200. PubMed PMID: 10801897.
146. Kim OV, Litvinov RI, Alber MS, Weisel JW. Quantitative structural mechanobiology of platelet-driven blood clot contraction. Nat Commun. 2017;8(1):1274. Epub 2017/11/04. doi: 10.1038/s41467-017-00885-x. PubMed PMID: 29097692; PMCID: PMC5668372.
147. Qiu Y, Myers DR, Lam WA. The biophysics and mechanics of blood from a materials perspective. Nat Rev Mater. 2019;4(5):294-311. Epub 2020/05/22. doi: 10.1038/s41578-019-0099-y. PubMed PMID: 32435512; PMCID: PMC7238390.
148. Brown AE, Litvinov RI, Discher DE, Purohit PK, Weisel JW. Multiscale mechanics of fibrin polymer: gel stretching with protein unfolding and loss of water. Science. 2009;325(5941):741-4. Epub 2009/08/08. doi: 10.1126/science.1172484. PubMed PMID: 19661428; PMCID: PMC2846107.
149. Piechocka IK, Bacabac RG, Potters M, Mackintosh FC, Koenderink GH. Structural hierarchy governs fibrin gel mechanics. Biophys J. 2010;98(10):2281-9. Epub 2010/05/21. doi: 10.1016/j.bpj.2010.01.040. PubMed PMID: 20483337; PMCID: PMC2872216.
150. Wolberg AS. Thrombin generation and fibrin clot structure. Blood Rev. 2007;21(3):131-42. Epub 2007/01/09. doi: 10.1016/j.blre.2006.11.001. PubMed PMID: 17208341.
151. Jirouskova M, Jaiswal JK, Coller BS. Ligand density dramatically affects integrin alpha IIb beta 3-mediated platelet signaling and spreading. Blood. 2007;109(12):5260-9. Epub 2007/03/03. doi: 10.1182/blood-2006-10-054015. PubMed PMID: 17332246; PMCID: PMC1890822.
152. Kee MF, Myers DR, Sakurai Y, Lam WA, Qiu Y. Platelet mechanosensing of collagen matrices. PLoS One. 2015;10(4):e0126624. Epub 2015/04/29. doi: 10.1371/journal.pone.0126624. PubMed PMID: 25915413; PMCID: PMC4411076.

153. Qiu Y, Brown AC, Myers DR, Sakurai Y, Mannino RG, Tran R, Ahn B, Hardy ET, Kee MF, Kumar S, Bao G, Barker TH, Lam WA. Platelet mechanosensing of substrate stiffness during clot formation mediates adhesion, spreading, and activation. Proc Natl Acad Sci U S A. 2014;111(40):14430-5. Epub 2014/09/24. doi: 10.1073/pnas.1322917111. PubMed PMID: 25246564; PMCID: PMC4210024.
154. Myers DR, Qiu Y, Fay ME, Tennenbaum M, Chester D, Cuadrado J, Sakurai Y, Baek J, Tran R, Ciciliano JC, Ahn B, Mannino RG, Bunting ST, Bennett C, Briones M, Fernandez-Nieves A, Smith ML, Brown AC, Sulchek T, Lam WA. Single-platelet nanomechanics measured by high-throughput cytometry. Nat Mater. 2017;16(2):230-5. Epub 2016/11/01. doi: 10.1038/nmat4772. PubMed PMID: 27723740; PMCID: PMC5266633.
155. Tablin F, Taube D. Platelet intermediate filaments: detection of a vimentinlike protein in human and bovine platelets. Cell Motil Cytoskeleton. 1987;8(1):61-7. Epub 1987/01/01. doi: 10.1002/cm.970080109. PubMed PMID: 3308127.
156. Muszbek L, Adany R, Glukhova MA, Frid MG, Kabakov AE, Koteliansky VE. The identification of vimentin in human blood platelets. Eur J Cell Biol. 1987;43(3):501-4. Epub 1987/06/01. PubMed PMID: 3305025.
157. Da Q, Behymer M, Correa JI, Vijayan KV, Cruz MA. Platelet adhesion involves a novel interaction between vimentin and von Willebrand factor under high shear stress. Blood. 2014;123(17):2715-21. Epub 2014/03/20. doi: 10.1182/blood-2013-10-530428. PubMed PMID: 24642750; PMCID: PMC3999756.
158. Podor TJ, Singh D, Chindemi P, Foulon DM, McKelvie R, Weitz JI, Austin R, Boudreau G, Davies R. Vimentin exposed on activated platelets and platelet microparticles localizes vitronectin and plasminogen activator inhibitor complexes on their surface. J Biol Chem. 2002;277(9):7529-39. Epub 2001/12/18. doi: 10.1074/jbc.M109675200. PubMed PMID: 11744725.
159. Sandmann R, Koster S. Topographic Cues Reveal Two Distinct Spreading Mechanisms in Blood Platelets. Sci Rep. 2016;6:22357. Epub 2016/03/05. doi: 10.1038/srep22357. PubMed PMID: 26934830; PMCID: PMC4776100.
160. Mangalpally KK, Siqueiros-Garcia A, Vaduganathan M, Dong JF, Kleiman NS, Guthikonda S. Platelet activation patterns in platelet size sub-populations: differential responses to aspirin in vitro. J Thromb Thrombolysis. 2010;30(3):251-62. Epub 2010/05/27. doi: 10.1007/s11239-010-0489-x. PubMed PMID: 20502945.
161. Opper C, Schuessler G, Kuschel M, Clement HW, Gear AR, Hinsch E, Hinsch K, Wesemann W. Analysis of GTP-binding proteins, phosphoproteins, and cytosolic calcium in functional heterogeneous human blood platelet subpopulations. Biochem Pharmacol. 1997;54(9):1027-35. Epub 1997/11/28. doi: 10.1016/s0006-2952(97)00317-1. PubMed PMID: 9374424.
162. Karpatkin S. Heterogeneity of human platelets. I. Metabolic and kinetic evidence suggestive of young and old platelets. J Clin Invest. 1969;48(6):1073-82. Epub 1969/06/01. doi: 10.1172/JCI106063. PubMed PMID: 5771188; PMCID: PMC322321.
163. Handtke S, Thiele T. Large and small platelets-(When) do they differ? J Thromb Haemost. 2020;18(6):1256-67. Epub 2020/02/29. doi: 10.1111/jth.14788. PubMed PMID: 32108994.
164. Mor-Vaknin N, Punturieri A, Sitwala K, Markovitz DM. Vimentin is secreted by activated macrophages. Nat Cell Biol. 2003;5(1):59-63. Epub 2002/12/17. doi: 10.1038/ncb898. PubMed PMID: 12483219.

165. Xu B, deWaal RM, Mor-Vaknin N, Hibbard C, Markovitz DM, Kahn ML. The endothelial cell-specific antibody PAL-E identifies a secreted form of vimentin in the blood vasculature. Mol Cell Biol. 2004;24(20):9198-206. Epub 2004/10/01. doi: 10.1128/MCB.24.20.9198-9206.2004. PubMed PMID: 15456890; PMCID: PMC517872.
166. Xiao J, Chen L, Melander O, Orho-Melander M, Nilsson J, Borne Y, Engstrom G. Circulating Vimentin Is Associated With Future Incidence of Stroke in a Population-Based Cohort Study. Stroke. 2021;52(3):937-44. Epub 2021/02/05. doi: 10.1161/STROKEAHA.120.032111. PubMed PMID: 33535783.
167. Fan E, Brodie D, Slutsky AS. Acute Respiratory Distress Syndrome: Advances in Diagnosis and Treatment. JAMA. 2018;319(7):698-710. Epub 2018/02/22. doi: 10.1001/jama.2017.21907. PubMed PMID: 29466596.
168. Misharin AV, Morales-Nebreda L, Reyfman PA, Cuda CM, Walter JM, McQuattie-Pimentel AC, Chen CI, Anekalla KR, Joshi N, Williams KJN, Abdala-Valencia H, Yacoub TJ, Chi M, Chiu S, Gonzalez-Gonzalez FJ, Gates K, Lam AP, Nicholson TT, Homan PJ, Soberanes S, Dominguez S, Morgan VK, Saber R, Shaffer A, Hinchcliff M, Marshall SA, Bharat A, Berdnikovs S, Bhorade SM, Bartom ET, Morimoto RI, Balch WE, Sznajder JI, Chandel NS, Mutlu GM, Jain M, Gottardi CJ, Singer BD, Ridge KM, Bagheri N, Shilatifard A, Budinger GRS, Perlman H. Monocyte-derived alveolar macrophages drive lung fibrosis and persist in the lung over the life span. J Exp Med. 2017;214(8):2387-404. Epub 2017/07/12. doi: 10.1084/jem.20162152. PubMed PMID: 28694385; PMCID: PMC5551573.
169. Bargagna-Mohan P, Lei L, Thompson A, Shaw C, Kasahara K, Inagaki M, Mohan R. Vimentin Phosphorylation Underlies Myofibroblast Sensitivity to Withaferin A In Vitro and during Corneal Fibrosis. PLoS One. 2015;10(7):e0133399. Epub 2015/07/18. doi: 10.1371/journal.pone.0133399. PubMed PMID: 26186445; PMCID: PMC4506086.
170. Grin B, Mahammad S, Wedig T, Cleland MM, Tsai L, Herrmann H, Goldman RD. Withaferin a alters intermediate filament organization, cell shape and behavior. PLoS One. 2012;7(6):e39065. Epub 2012/06/22. doi: 10.1371/journal.pone.0039065. PubMed PMID: 22720028; PMCID: PMC3376126.
171. Tirelli N, Lutolf MP, Napoli A, Hubbell JA. Poly(ethylene glycol) block copolymers. J Biotechnol. 2002;90(1):3-15. Epub 2002/06/19. doi: 10.1016/s1389-0352(01)00057-5. PubMed PMID: 12069046.
172. Harris JM, Chess RB. Effect of pegylation on pharmaceuticals. Nat Rev Drug Discov. 2003;2(3):214-21. Epub 2003/03/04. doi: 10.1038/nrd1033. PubMed PMID: 12612647.
173. Napoli A, Valentini M, Tirelli N, Muller M, Hubbell JA. Oxidation-responsive polymeric vesicles. Nat Mater. 2004;3(3):183-9. Epub 2004/03/03. doi: 10.1038/nmat1081. PubMed PMID: 14991021.
174. Allen SD, Liu YG, Kim T, Bobbala S, Yi S, Zhang X, Choi J, Scott EA. Celastrol-loaded PEG-b-PPS nanocarriers as an anti-inflammatory treatment for atherosclerosis. Biomater Sci. 2019;7(2):657-68. Epub 2019/01/03. doi: 10.1039/c8bm01224e. PubMed PMID: 30601470; PMCID: PMC6368678.
175. Yi S, Allen SD, Liu YG, Ouyang BZ, Li X, Augsornworawat P, Thorp EB, Scott EA. Tailoring Nanostructure Morphology for Enhanced Targeting of Dendritic Cells in Atherosclerosis. ACS Nano. 2016;10(12):11290-303. Epub 2016/12/10. doi: 10.1021/acsnano.6b06451. PubMed PMID: 27935698; PMCID: PMC5418862.
176. Shang S, Kats D, Cao L, Morgun E, Velluto D, He Y, Xu Q, Wang CR, Scott EA. Induction of Mycobacterium Tuberculosis Lipid-Specific T Cell Responses by Pulmonary Delivery of

Mycolic Acid-Loaded Polymeric Micellar Nanocarriers. Front Immunol. 2018;9:2709. Epub 2018/12/13. doi: 10.3389/fimmu.2018.02709. PubMed PMID: 30538700; PMCID: PMC6277542.
177. Allen SL, YG; Bobbala S; Cai L; Hecker, PI; Temel R; Scott EA. Polymersomes scalably fabricated via flash nanoprecipitation are non-toxic in non-human primates and associate with leukocytes in the spleen and kidney following intravenous administration. Nano Research. 2018;11:5689-703.
178. Kenneth NS, Younger JM, Hughes ED, Marcotte D, Barker PA, Saunders TL, Duckett CS. An inactivating caspase 11 passenger mutation originating from the 129 murine strain in mice targeted for c-IAP1. Biochem J. 2012;443(2):355-9. Epub 2012/02/16. doi: 10.1042/BJ20120249. PubMed PMID: 22332634; PMCID: PMC3327503.
179. Scott EA, Stano A, Gillard M, Maio-Liu AC, Swartz MA, Hubbell JA. Dendritic cell activation and T cell priming with adjuvant- and antigen-loaded oxidation-sensitive polymersomes. Biomaterials. 2012;33(26):6211-9. Epub 2012/06/05. doi: 10.1016/j.biomaterials.2012.04.060. PubMed PMID: 22658634.
180. Napolitano LM, Angus DC, Uyeki TM. Critically ill patients with influenza A(H1N1)pdm09 virus infection in 2014. JAMA. 2014;311(13):1289-90. Epub 2014/02/26. doi: 10.1001/jama.2014.2116. PubMed PMID: 24566924; PMCID: PMC6689404.
181. Writing Committee of the WHOCoCAoPI, Bautista E, Chotpitayasunondh T, Gao Z, Harper SA, Shaw M, Uyeki TM, Zaki SR, Hayden FG, Hui DS, Kettner JD, Kumar A, Lim M, Shindo N, Penn C, Nicholson KG. Clinical aspects of pandemic 2009 influenza A (H1N1) virus infection. N Engl J Med. 2010;362(18):1708-19. Epub 2010/05/07. doi: 10.1056/NEJMra1000449. PubMed PMID: 20445182.
182. Papazian L, Forel JM, Gacouin A, Penot-Ragon C, Perrin G, Loundou A, Jaber S, Arnal JM, Perez D, Seghboyan JM, Constantin JM, Courant P, Lefrant JY, Guerin C, Prat G, Morange S, Roch A, Investigators AS. Neuromuscular blockers in early acute respiratory distress syndrome. N Engl J Med. 2010;363(12):1107-16. Epub 2010/09/17. doi: 10.1056/NEJMoa1005372. PubMed PMID: 20843245.
183. Guerin C, Reignier J, Richard JC, Beuret P, Gacouin A, Boulain T, Mercier E, Badet M, Mercat A, Baudin O, Clavel M, Chatellier D, Jaber S, Rosselli S, Mancebo J, Sirodot M, Hilbert G, Bengler C, Richecoeur J, Gainnier M, Bayle F, Bourdin G, Leray V, Girard R, Baboi L, Ayzac L, Group PS. Prone positioning in severe acute respiratory distress syndrome. N Engl J Med. 2013;368(23):2159-68. Epub 2013/05/22. doi: 10.1056/NEJMoa1214103. PubMed PMID: 23688302.
184. Yi S, Zhang X, Sangji H, Liu Y, Allen SD, Xiao B, Bobbala S, Braverman CL, Cai L, Hecker PI, DeBerge M, Thorp EB, Temel RE, Stupp SI, Scott EA. Surface engineered polymersomes for enhanced modulation of dendritic cells during cardiovascular immunotherapy. Adv Funct Mater. 2019;29(42). Epub 2019/10/17. doi: 10.1002/adfm.201904399. PubMed PMID: 34335131; PMCID: PMC8320590.
185. Medrano-Bosch M, Moreno-Lanceta A, Melgar-Lesmes P. Nanoparticles to Target and Treat Macrophages: The Ockham's Concept? Pharmaceutics. 2021;13(9). Epub 2021/09/29. doi: 10.3390/pharmaceutics13091340. PubMed PMID: 34575416; PMCID: PMC8469871.
186. Barish GD, Downes M, Alaynick WA, Yu RT, Ocampo CB, Bookout AL, Mangelsdorf DJ, Evans RM. A Nuclear Receptor Atlas: macrophage activation. Mol Endocrinol. 2005;19(10):2466-77. Epub 2005/07/30. doi: 10.1210/me.2004-0529. PubMed PMID: 16051664.
187. Allen S, Osorio O, Liu YG, Scott E. Facile assembly and loading of theranostic polymersomes via multi-impingement flash nanoprecipitation. J Control Release. 2017;262:91-

103. Epub 2017/07/25. doi: 10.1016/j.jconrel.2017.07.026. PubMed PMID: 28736263; PMCID: PMC5603398.
188. Allen SD, Bobbala S, Karabin NB, Modak M, Scott EA. Benchmarking Bicontinuous Nanospheres against Polymersomes for in Vivo Biodistribution and Dual Intracellular Delivery of Lipophilic and Water-Soluble Payloads. ACS Appl Mater Interfaces. 2018;10(40):33857-66. Epub 2018/09/15. doi: 10.1021/acsami.8b09906. PubMed PMID: 30213189.
189. Han J, Zhu Z, Qian H, Wohl AR, Beaman CJ, Hoye TR, Macosko CW. A simple confined impingement jets mixer for flash nanoprecipitation. J Pharm Sci. 2012;101(10):4018-23. Epub 2012/07/11. doi: 10.1002/jps.23259. PubMed PMID: 22777753; PMCID: PMC6382459.
190. Liu F, Mih JD, Shea BS, Kho AT, Sharif AS, Tager AM, Tschumperlin DJ. Feedback amplification of fibrosis through matrix stiffening and COX-2 suppression. J Cell Biol. 2010;190(4):693-706. doi: 10.1083/jcb.201004082. PubMed PMID: 20733059; PMCID: PMC2928007.
191. Wang N, Stamenovic D. Contribution of intermediate filaments to cell stiffness, stiffening, and growth. Am J Physiol Cell Physiol. 2000;279(1):C188-94. doi: 10.1152/ajpcell.2000.279.1.C188. PubMed PMID: 10898730.
192. Li IMH, Horwell AL, Chu G, de Crombrugghe B, Bou-Gharios G. Characterization of Mesenchymal-Fibroblast Cells Using the Col1a2 Promoter/Enhancer. Methods Mol Biol. 2017;1627:139-61. doi: 10.1007/978-1-4939-7113-8_10. PubMed PMID: 28836200.
193. Booth AJ, Hadley R, Cornett AM, Dreffs AA, Matthes SA, Tsui JL, Weiss K, Horowitz JC, Fiore VF, Barker TH, Moore BB, Martinez FJ, Niklason LE, White ES. Acellular normal and fibrotic human lung matrices as a culture system for in vitro investigation. Am J Respir Crit Care Med. 2012;186(9):866-76. doi: 10.1164/rccm.201204-0754OC. PubMed PMID: 22936357; PMCID: PMC3530219.
194. Chen H, Qu J, Huang X, Kurundkar A, Zhu L, Yang N, Venado A, Ding Q, Liu G, Antony VB, Thannickal VJ, Zhou Y. Mechanosensing by the alpha6-integrin confers an invasive fibroblast phenotype and mediates lung fibrosis. Nat Commun. 2016;7:12564. doi: 10.1038/ncomms12564. PubMed PMID: 27535718; PMCID: PMC4992155.
195. Marinkovic A, Liu F, Tschumperlin DJ. Matrices of physiologic stiffness potently inactivate idiopathic pulmonary fibrosis fibroblasts. Am J Respir Cell Mol Biol. 2013;48(4):422-30. doi: 10.1165/rcmb.2012-0335OC. PubMed PMID: 23258227; PMCID: PMC3653602.
196. Murray ME, Mendez MG, Janmey PA. Substrate stiffness regulates solubility of cellular vimentin. Mol Biol Cell. 2014;25(1):87-94. doi: 10.1091/mbc.E13-06-0326. PubMed PMID: 24173714; PMCID: PMC3873896.
197. Tse JR, Engler AJ. Preparation of hydrogel substrates with tunable mechanical properties. Curr Protoc Cell Biol. 2010;Chapter 10:Unit 10 6. doi: 10.1002/0471143030.cb1016s47. PubMed PMID: 20521229.